

X-RAY NEBULAR MODELS

TIMOTHY R. KALLMAN AND RICHARD MCCRAY

Joint Institute for Laboratory Astrophysics, University of Colorado and National Bureau of Standards

Received 1981 July 23; accepted 1982 April 27

ABSTRACT

Theoretical models are presented for the temperature and ionization structure of spherically symmetric, constant density, gaseous nebulae surrounding compact X-ray sources and for the optical, UV, and X-ray spectra emerging from the nebulae. The structure is determined by assuming a local balance between heating and cooling in the gas, and the radiation field is found by solving a simplified equation of transfer. The calculations include an accurate and comprehensive treatment of the atomic processes affecting the state of the gas and the radiation field. The destruction of line radiation during resonance scattering causes models to be significantly hotter and more highly ionized than previous models of the same type. Model results are presented for a wide variety of gas densities and X-ray source spectra, scaling laws which allow these results to be generalized to a wide variety of astrophysical solutions are discussed, and column densities of multiply charged species are tabulated.

Subject headings: nebulae: general — radiation mechanisms — radiative transfer —
ultraviolet: spectra — X-rays: spectra

I. INTRODUCTION

The known cosmic X-ray sources can be divided roughly into two classes: diffuse sources, including hot interstellar gas, supernova remnants, and intergalactic gas in clusters; and compact sources, including galactic binaries, bursters, and the nuclei of active galaxies and quasars. In the diffuse sources, the X-ray emission and the ionization of the elements result primarily from electron collisions in a hot (10^6 to 10^8 K) optically thin gas of low atomic density ($\sim 10^{-4}$ cm $^{-3}$ in clusters of galaxies to $\sim 10^{+2}$ cm $^{-3}$ in supernova remnants). In contrast, the compact sources (except stellar coronae) are thought to consist of a central source of continuum X-rays surrounded by a distribution of gas. The emergent X-ray spectrum may obtain spectral features as a result of propagation through the gas, whose ionization structure and emissivity are controlled primarily by photoionization, recombination, and fluorescence rather than by electron collisions. Thus, the problem of understanding the spectra of the compact X-ray sources is the X-ray analog of the planetary nebula problem.

The solution to this problem is important for understanding a wide variety of phenomena associated with X-ray sources. In the binary sources, the compact source is embedded in the stellar wind of its companion, and the propagation of the X-rays through the wind may cause observable soft X-ray absorption and emission features (Buff and McCray 1974a; Hatchett and McCray 1977). X-ray photoionization of trace elements causes periodic variations in the P Cygni profiles of ultraviolet resonance lines formed in the stellar wind

(Hatchett and McCray 1977). This effect has been observed in the spectra of the binary X-ray sources 4U0900–40, Cyg X–1, and LMC X–4 (Dupree *et al.* 1980; Hammerschlag-Hensberge 1980; Treves *et al.* 1980). Cassinelli and Olson (1979) have invoked X-ray photonization models to explain absorption line spectra in early-type stars. X-ray photoionization by a compact galactic source may create shells of highly ionized traced elements in surrounding interstellar gas observable by ultraviolet absorption spectroscopy (McCray, Wright, and Hatchett 1977). Dense interstellar gas near an X-ray source may fluoresce with a distinct optical emission line spectrum (Halpern and Grindlay 1980).

The X-rays also may affect profoundly the gas dynamics near a compact object, both through radiation pressure (Tarter and McKee 1973; Hatchett, Buff, and McCray 1976, hereafter HBM) and through heating (Buff and McCray 1974b; Ostriker *et al.* 1976; Cowie, Ostriker, and Stark 1978; Shull 1979). Gas illuminated by X-rays is subject to thermal instability that may give rise to the coexistence of two or more density phases in pressure equilibrium and may drive stellar winds (Basko *et al.* 1977; London, McCray, and Auer 1981). These effects are particularly important for understanding gas dynamics in the nuclei of active galaxies and quasars (McCray 1979), which are now known to be powerful X-ray sources (Tananbaum *et al.* 1979).

The first detailed calculations of the ionization and temperature structure of gas illuminated by an X-ray source were presented by Tarter, Tucker, and Salpeter (1969, hereafter TTS) for optically thin nebulae and by

Tarter and Salpeter (1969) for optically thick nebulae. These calculations have been improved by several authors, including HBM, who included the important effects of Auger ionization and Compton heating, and by McCray, Wright, and Hatchett (1977) and Halpern and Grindlay (1980), who included the effects of charge transfer collisions. Many such calculations, reviewed by Davidson and Netzer (1979), have been made to explain the emission line spectra of quasars. In these objects, the gas density is sufficiently high that the effects of resonance line trapping and collisional de-excitation may alter significantly the emergent spectra (see Krolik and McKee 1978; Kwan and Krolik 1979; Ferland and Netzer 1979). The effects of resonance line trapping are also likely to be important in the dense gas around compact galactic X-ray sources.

Because of the general importance of these X-ray photoionization models, we have completely revised the code of HBM to include a comprehensive description of the major atomic and radiative processes determining the structure of X-ray photoionized nebulae. Significant improvements in the calculations presented here are:

1. A more comprehensive description of the ions of cosmically abundant elements, including iron, which dominates the heating and cooling for important ranges of parameter space;
2. A thorough updating of all atomic processes;
3. Calculation of detailed optical, ultraviolet and X-ray emission line and continuum spectra, including some 530 resonance, subordinate, intercombination, and forbidden lines;
4. Consideration of the effects of resonance line trapping, including the Bowen resonance fluorescence mechanism.

These model nebulae are restricted to cases where spherical geometry and uniform gas density apply and so will not be applicable to situations such as QSO emission line clouds, where plane-parallel geometry is a better assumption.

In this paper we describe in detail several models of X-ray photoionized nebulae, with the defining parameters spanning a broad range from those characteristic of galactic binaries to those characteristics of quasars. In § II we define the model and its assumptions and parameters. In § III we discuss the atomic processes determining the ionization and temperature of the gas, and in § IV we discuss the transfer of continuum and line radiation and the formation of the emergent spectrum. In § V we describe our method for solving the problem. Finally, In § VI we present and discuss the models.

II. THE MODEL

Our models for X-ray illuminated clouds consist of a spherical gas cloud with a point source of continuum radiation at the center. The input parameters are the

source spectrum, the gas composition, and the gas density. The source spectrum is described by the spectral luminosity, $L_{0\epsilon} = Lf_\epsilon$, where L is the total luminosity. The normalized spectral function, f_ϵ , may be of one of three types: thermal bremsstrahlung, $f_\epsilon \propto \exp(-\epsilon/kT)$; blackbody, $f_\epsilon \propto \epsilon^3/[\exp(\epsilon/kT)-1]$; or power law, $f_\epsilon \propto \epsilon^{-\alpha}$. The gas consists of the elements H, He, C, N, O, Ne, Si, S, and Fe, with relative abundances given by Withbroe (1971). These are allowed to range in ionization from neutral to fully stripped, with the exclusion of the ions with threshold energies below 13.6 eV.

Clouds are assumed to have given density. This may be the case if the hydrodynamic time scale is long compared to the time scale for the X-ray luminosity to change, or if the gas flow is supersonic. If these conditions are not met, constant pressure gas may be a better approximation.

The construction of a model consists of the simultaneous determination of the state of the gas and the radiation field as a function of distance from the source. The state of the gas at each radius follows from the assumption of a stationary local balance between heating and cooling and between ionization and recombination. This local balance assumption is valid if thermal and ionization time scales are shorter than flow time scales in the gas, a condition which is satisfied in a wide range of situations of interest.

When the gas is optically thin, the radiation field at each radius is determined simply by geometrical dilution of the given source spectrum f_ϵ . Then, as shown by TTS, the state of the gas depends only on the parameter $\xi = L/nR^2$. This scaling law allows the results of one model calculation to be applied to a wide variety of situations. The parameter ξ is proportional to the parameter $U_H = F_H/n_e$ used in quasar models (Davidson and Netzer 1979), where F_H is the incident flux at the hydrogen Lyman limit. Note that our models apply to filled spheres, while most models for quasar emission lines assume narrow density-bounded filaments at roughly constant U_H .

Our models range from optically thin to optically thick in the photoionization continua of abundant elements. In the latter case, we approximate the transfer of continuum radiation by assuming that diffuse radiation emitted at each radius is directed radially outward from the center of the cloud. This assumption, together with the detailed procedure for solving the transfer problem, is discussed further in § V. HBM showed that in this case the state of the gas could be parametrized in terms of ξ and one additional parameter which is a function of L and $n(R)$, the number density. In the case $n = \text{constant}$, this second parameter is simply $(Ln)^{1/2}$ (McCray, Wright, and Hatchett 1977).

This simple picture breaks down when the cloud optical depth is large. In the general case, the state of the gas at any point in the cloud is coupled to the state of the gas in a large part of the rest of the cloud. Over a

wide range of plausible situations large optical depths occur in the cores of resonance lines of abundant ions, which may be important in cooling the gas. As discussed in § IV, the nature of the frequency redistribution in line scattering allows a simple but fairly accurate description of the transfer of this radiation. However, the resonance line photon destruction during scattering causes the distribution of the lower ionization stages to depend on the location of the cloud boundary, and so leads to departures from the simple scaling laws of HBM.

When the electron scattering optical depth, τ_e , of the cloud becomes significant, the outward-only approximation used here breaks down, and a more sophisticated method of describing the radiative transfer must be used (e.g., Ross 1979). Therefore, the range of validity of the models presented here is restricted to $\tau_e \leq 0.3$, or electron column densities $\leq 10^{24} \text{ cm}^2$.

III. THE STATE OF THE GAS

a) Ionization and Recombination

The state of the gas is defined by its temperature and by the ionic level populations. All ions will be predominantly in the ground state, and except for hydrogen and helium the populations of excited levels may be neglected. The relative abundances of the ions of a given element are found by solving the ionization equilibrium equations under the assumption of local balance, subject to the constraint of particle number conservation for each element. These equations may be written schematically as

$$(\text{Ionization}) = (\text{Recombination}). \quad (1)$$

Explicit forms of these equations have been given by Osterbrock (1974) and Halpern and Grindlay (1980). The ionization processes included in our models are photoionization (including the effects of the Auger process and secondary ionization by Auger electrons and by fast photoelectrons), charge transfer ionization, and collisional ionization. Recombination processes include radiative and dielectronic recombination and charge transfer.

i) Photoionization

This process dominates the ionization throughout the majority of our models. Photoionization rates are obtained by convolving the radiation field with the photoionization cross section. Cross sections are required for the large number of ions and wide range of photon energies occurring in our models. The task of estimating them is simplified by their scaling behavior along isonuclear sequences (Huebner, Argo, and Ohlsen 1978; Missavage, Manson, and Daum 1977; Reilman and Manson 1978). For a given subshell of an ion, the cross section has an energy dependence essentially independent of the ionization state of the ion and a value

approximately proportional to the number of electrons in the subshell. Given the cross section as a function of photon energy for a subshell of a neutral atom, the corresponding cross section for an ion of that element can then be obtained by: (1) discarding the part of the cross section between the threshold energies of the neutral atom and the ion; (2) correcting the remaining cross section for the number of electrons in the subshell of the ion; and (3) multiplying the cross section by a scale factor, of order 1, which takes into account the effects of correlations between electrons of the subshell in question and other electrons in the shell. If ionization occurs from a filled shell, the scale factor is 1.

Photoionization cross sections for neutral atoms over a wide range of photon energies have been calculated by Barfield, Koontz, and Huebner (1972). These values, obtained by the Hartree-Slater method, are expected to be accurate to within a few percent for K or L shell ionization, or M shell ionization at high energies, and within a factor of 2 for M shell ionization near threshold. This method will not account for the effects of resonances in photoionization cross sections near threshold. Such effects are likely to be large only for nearly neutral ions. Manson and co-workers (Missavage, Manson, and Daum 1977; Reilman and Manson 1978; Manson 1979) have calculated cross sections for a narrow range of energies above threshold for all subshells of all ions of interest to us. These results agree well with those of Barfield *et al.* in the energy range where they overlap and can be used to derive the scaling factors mentioned above. We use the threshold energies calculated by Clementi (1965), together with neutral cross sections, scaling factors, and the scaling procedure outlined above, to derive cross sections for all subshells of all ions of interest to us in the photon energy range between 13.6 eV and 20 keV. The one exception is the cross section for hydrogenic ions, where the exact, nonrelativistic formula is used (Bethe and Salpeter 1957). This formula will be accurate to within .5% for all ions considered here.

A further ionization process results from recoil of bound electrons following Compton scattering. We account for this process approximately by letting all cross sections asymptotically approach the Thomson value at high energies. This results in a slight overestimate of the Compton ionization cross section, as shown by Halpern and Grindlay (1980), but the error is negligible for all cases of interest to us.

The ionization in X-ray illuminated clouds is enhanced by Auger cascades following the removal of inner shell electrons. This process can result in the ejection of up to eight extra electrons (in the case of iron) in addition to the original photoelectron. We include this effect in the ionization equilibrium equations following the method outlined by Weisheit (1974). In cases where the Auger yield depends on whether a K shell vacancy is filled by a $K L_{II,III}$ or a $K L_I L_{II,III}$ transition, we calculate

the relative probabilities for these processes using rates given by McGuire (1969, 1970). The reduction in the iron K shell Auger yield due to radiative transitions is also included. The fluorescence yield for this process is taken to be 0.34 (Bambynek *et al.* 1972), independent of ionization stage. This assumption has been shown to be roughly correct in the case of neon (Bhalla and Hein 1973).

ii) Collisional Ionization

Ionization by electron collisions is important if the gas temperature approaches the ionization threshold energy of the most abundant ions in the gas. This can occur just outside an ionization front or in the region where the $n = 2$ levels of hydrogen are populated (see below). Since the temperature in our models is considerably lower than is found in coronal models for a corresponding degree of ionization, the contribution to the collisional ionization rate comes predominantly from electrons with energies barely above the ionization threshold. We use the rates derived by Cox (1970) from the cross sections of Lotz (1967), which are accurate to within $\sim 40\%$ of experimental values for the energy region near threshold (Burgess *et al.* 1977; Crandall, Phaneuf, and Gregory 1979).

A significant enhancement of the effective collisional ionization rate results from electron collisional excitation of autoionizing levels. This process is particularly important for ions of the boron isoelectronic sequence (Summers 1972) and has recently been shown to occur for lithium-like ions (Crandall *et al.* 1979). We include a correction to the collisional ionization rate which accounts for this effect, using rates calculated by Sarazin (1978).

A further contribution to the total ionization rate comes from collisional ionization by fast electrons produced either by X-ray photoionization or by Auger processes. In an ionized gas, these electrons slow primarily by elastic collisions with thermal electrons and deposit their energy as heat, but in neutral ($n_e/n_H \leq 10^{-2}$) gas, collisional excitation and ionization of hydrogen and helium are significant. We include the rates of hydrogen and helium ionization and heating produced per incident electron using the function of electron energy and the neutral fraction of the gas calculated by Shull (1979). The rate per helium atom is assumed to be roughly one-half that per hydrogen atom, corresponding to the ratio of the peak helium to hydrogen collisional ionization cross sections (see Lotz 1967).

iii) Recombination

Radiative and dielectronic recombination rates for elements other than iron are taken from the work of Aldrovandi and Pequignot (1973) and rates for iron from Sarazin (1978). For hydrogenic ions, we use the total rates given by Gould and Thakur (1970) and

calculate the rates for individual n levels from the Milne relation (Osterbrock 1974). We also include the suppression of dielectronic recombination by electron collisions, using the fits of Raymond (1978) to the calculations of Summers (1972).

iv) Charge Transfer

Rates for charge transfer reactions are taken from Butler, Heil, and Dalgarno (1980), Butler and Dalgarno (1980), and Dalgarno, Heil, and Butler (1981). For highly charged ions, where accurate calculations do not exist, we scaled the rates along isonuclear sequences, assuming that the cross section is proportional to the square of the total residual charge on the ion. We also include the resonant charge transfer reaction of O II with H (Field and Steigman 1971).

b) Excitation

For most of the ions in our model, the permitted radiative decays of bound excited levels are much faster than the excitation rates, so that their populations are negligible compared to that of the ground state. For hydrogen and helium, however, the radiation from the decays of excited levels may be trapped sufficiently to build up an appreciable population of excited atoms or ions. Since neutral helium is never the dominant coolant in our models, we neglect the effects of excited level populations for this ion, but we explicitly calculate the $n = 2$ level populations for all hydrogenic ions. Populations are found according to the local balance assumption by solving the statistical equilibrium equations for an ion consisting of the bound $n = 1$ and $n = 2$ levels and the continuum. We also calculate the fraction of the $n = 2$ population that is in either of the two sublevels, $2s$ and $2p$. For each level, the statistical equilibrium equations may be written schematically as

$$(\text{Rate in}) = (\text{Rate out}). \quad (2)$$

We include all collisional and radiative rates between the various levels, accounting for the effects of resonance absorption in the $n = 1$ to $n = 2$ transition by setting the radiative decay rate $A'_{21} = A_{21}P_{\text{esc}}$, where A_{21} is the vacuum decay rate and P_{esc} is the line escape probability (§ IV).

Collisional and radiative rates connecting the ground level of hydrogenic ions with the continuum have been discussed above. Photoionization cross sections for $n = 2$ are taken from Bethe and Salpeter (1957). Collisional ionization from $n = 2$ is assumed to follow the classical scaling law (Krolik and McKee 1978),

$$C_n(T) = n^3 C_1(n^2 T), \quad (3)$$

where $C_n(T)$ is the rate for ionization from a level with quantum number n . Rates for two-photon decays of the

2s level are from Tucker and Koren (1971). Rates for collisional transfers between 2s and 2p sublevels are from Brocklehurst (1971). Collisional rates between $n = 1$ and $n = 2$ are from Burke, Ormonde, and Whitaker (1967) and Mahan, Gallagher, and Smith (1976) for neutral hydrogen, and from Mewe (1972) for other hydrogenic ions.

c) Heating and Cooling

The temperature is found by solving the equation of thermal equilibrium, which may be written schematically as

$$(\text{Heating}) = (\text{Cooling}). \quad (4)$$

The heating term includes photoionization heating (including the Auger effect), Compton heating, charge transfer, and collisional de-excitation. The cooling term includes radiative and dielectronic recombination, bremsstrahlung, collisional ionization, collisional excitation of bound levels, and (endothermic) charge transfer.

In the most highly ionized regions of our models, the dominant heating process is electron recoil following Compton scattering. The net heating rate may be written (Ross 1979)

$$n_e \Gamma_e = \frac{\sigma_T}{m_e c^2} n_e \left[\int \left(\epsilon - \frac{21}{5} \frac{\epsilon^2}{m_e c^2} \right) J_\epsilon d\epsilon - 4kT \int J_\epsilon d\epsilon \right]. \quad (5)$$

Here σ_T is the Thomson cross section, n_e is the electron number density, T is the electron temperature, and J_ϵ is the local mean intensity in the radiation field. The first term in the brackets represents the heating of electrons by the X-rays, and includes the Klein-Nishina correction to the Compton scattering to lowest order in $\epsilon/m_e c^2$. The second term represents cooling of hot electrons by scattering with low energy photons.

The heating due to photoelectrons and Auger electrons depends on whether these electrons are slowed by elastic collisions with thermal electrons or by inelastic collisions with hydrogen and helium and has been calculated as a function of electron energy and the neutral fraction of the gas by Shull (1979). The spectrum of photoelectron energies for each ion is found by convolving the radiation field, weighted by photoelectron energy, with the photoionization cross section (see, e.g., Osterbrock 1974). In calculating the Auger electron spectrum for each ion, we assume crudely that the energy liberated by Auger processes is shared equally among the ejected electrons. The total energy in Auger electrons is simply the difference in total electronic binding energy of the initial and final ions.

The cooling rate due to radiative recombination is calculated under the assumption that the mean energy

of a recombining electron is $3kT/4$. The dielectronic recombination cooling rate for each ion is calculated under the assumption that each recombination leads to the emission of a satellite to the lowest lying resonance line of the recombining ion. The charge transfer heating or cooling (per reaction) is simply the difference in total binding energies of the initial and final systems. Each collisional ionization removes an amount of energy equal to the ionization threshold energy. The bremsstrahlung cooling rate is (Osterbrock 1974)

$$n_e \Gamma_e = 1.42 \times 10^{-27} T^{1/2} z^2 n_e n_z \text{ ergs cm}^{-3} \text{ s}^{-1}, \quad (6)$$

where T is the electron temperature, n_e is the electron number density, z is the charge on the cooling ion, and n_z is the ion density.

One of the most important cooling processes is collisional excitation of bound levels. However, resonance lines emitted by the decay of these levels are subject to destruction during resonant trapping, which reduces the effective collisional excitation cooling rate. Our technique for including this cooling and suppression is described in § IV.

IV. RADIATION FIELD

The second main ingredient in our models is the radiation field. This can be separated broadly into two components—continuum and lines. The clouds that we consider have moderate optical depths in the continuum, which can be emitted or absorbed at any point in the cloud. Line radiation, on the other hand, will resonantly scatter only in a small spatial region near the point of emission. Therefore, we may describe its transfer with an escape probability formalism.

a) Continuum

Diffuse continuum radiation is emitted by three processes: thermal bremsstrahlung, radiative recombination, and two-photon decays of metastable levels. The emissivity due to recombination into a given level of an ion is assumed to be distributed uniformly in the spectral region between the ionization threshold of the level, I_{ij} , and the energy, $I_{ij} + 3kT/2$, and is normalized to the total recombination cooling for that level (see § IIIc). The thermal bremsstrahlung emissivity is given by Osterbrock (1974):

$$j_\epsilon = \frac{1}{4\pi} n_z n_e \frac{32 Z^2 e^4 h}{3 m^2 c^3} \left(\frac{\pi h \nu_0}{3kT} \right)^{1/2} e^{-h\nu/kT} g_{\text{ff}}(T, Z, r), \quad (7)$$

where T is the electron temperature, n_e is the electron abundance, Z is the charge on the most abundant ion, n_z is the abundance of that ion, and g_{ff} is a Born

approximation Gaunt factor (Bekefi 1966). For two-photon decays, we adopt the distribution (Tucker and Koren 1971):

$$H\left(\frac{\epsilon}{\epsilon_0}\right) = 12\left(\frac{\epsilon}{\epsilon_0}\right)^2 \left(1 - \frac{\epsilon}{\epsilon_0}\right), \quad (8)$$

where ϵ_0 is the excitation energy. Emissivities due to decays of metastable levels are included for all hydrogenic and helium-like ions. The decay rates of hydrogenic ions are calculated using the procedure described in the previous section. The method for calculating the decay rates of helium-like metastable levels is described below.

The continuum radiation field is modified primarily by photoabsorption, for which the opacity, $\kappa(\epsilon)$, is equal to the product of the ion abundance with the total photoionization cross section, summed over ions. The continuum will be affected slightly by the energy shift suffered by photons during Compton scattering, and we account for this effect approximately by removing a fraction of the radiation field given by

$$\frac{\Delta L_\epsilon}{L_\epsilon} = \frac{\Delta \epsilon}{\epsilon} \Delta \tau_T, \quad (9)$$

where $\Delta \epsilon / \epsilon$ is the fractional energy loss per Compton scattering and $\Delta \tau_T$ is the fractional Thomson optical depth. As shown by Ross, Weaver, and McCray (1978), the expression

$$\frac{\Delta \epsilon}{\epsilon} = \frac{\epsilon}{mc^2} \left(1 - \frac{4kT}{\epsilon} - \frac{21}{5} \frac{\epsilon}{mc^2}\right) \quad (10)$$

is valid in the limit that $\epsilon \ll mc^2$.

b) Line Emission

Altogether, we include in our models the 530 lines listed in Table 1. Line radiation is emitted by most of the processes that determine the thermal and ionization balance of the gas, including radiative and dielectronic recombination, charge transfer, collisional excitation, and fluorescence following inner shell ionization. Our treatment of line emission and escape is designed to provide a fairly comprehensive description of the energy balance in the gas and of the radiation field emergent from such a cloud.

For each ion, we consider line emission typically from three excited levels, chosen to illustrate the effects of important and qualitatively different transitions. Recombination rates to excited levels of each ion are taken to be hydrogenic, with the recombination rate to the highest excited level considered including the rates to all higher levels. In cases where a level may decay by more than one route, branching ratios for X-ray lines with wavelengths below 200 Å are taken from Kato (1976),

for EUV lines between 200 and 1000 Å from Stern, Wang, and Bowyer (1978), and for lines not covered by the other references from Wiese, Smith, and Glennon (1966) and from Wiese, Smith, and Miles (1969).

Emissivities due to dielectronic recombination, charge transfer, and inner shell fluorescence are proportional to the reaction rates for these processes. Dielectronic recombination leaves the core of the resulting ion in an excited state which decays with the emission of a line photon. We assume that the line emitted by this process is a satellite of the lowest energy line which originates from the ground level of the recombining ion. Line emission following charge transfer is assumed to occur in the cases described by Dalgarno and Butler (1978), Butler, Heil, and Dalgarno (1980), and Dalgarno, Heil, and Butler (1981). Inner shell fluorescence line emission is assumed to occur following K shell ionization of iron ions, with probability 0.34 (see § IIIa) and following inner shell ionization of any ion when the resulting vacancy cannot be filled by an Auger transition (e.g., lithium-like ions). Emission of the UV fine structure doublets of lithium-like ions (e.g., C IV $\lambda\lambda 1550$) is assumed to follow the K shell photoionization and Auger emission of the corresponding boron-like ion (e.g., C II) with probability 0.75 (Shapiro and Bahcall 1981), but similar Auger fluorescence processes from ions other than boron-like are neglected.

Rates for collisional excitation are calculated using the collision strengths summarized by Kato (1976) and Shull (1981) for X-ray lines with wavelengths less than 200 Å. For lines between 200 and 1000 Å we calculate collision strengths using the method of Van Regemorter (1962) and oscillator strengths from Stern, Wang, and Bowyer (1978). Average Gaunt factors are taken from Mewe (1972), and from Gau and Henry (1977) for lithium-like ions, and are evaluated at $E/kT = 1/1.5$. Oscillator strengths of optical and UV lines are taken from Wiese, Smith, and Glennon (1966) and Wiese, Smith, and Miles (1969). Wavelengths of inner shell fluorescence lines are taken from House (1969), and oscillator strengths from Mewe (1977). Oscillator strengths for the lower ionization stages of iron are from Abbott (1978), Biemont (1976), Morton and Smith (1973), and Czyzak and Krueger (1966). Forbidden line data are from Osterbrock (1974), Wiese, Smith, and Glennon (1966), Wiese, Smith, and Miles (1969), Raymond (1976), and Garstang, Robb, and Rountree (1978). Intercombination line data are from Osterbrock (1974) and Raymond (1976).

A particularly interesting set of lines are the $n = 2$ to $n = 1$ transitions of helium-like ions. As shown by Gabriel and Jordan (1969) and Blumenthal, Drake, and Tucker (1972), the ratio of the forbidden to intercombination line intensities from these ions can be a useful density diagnostic for high temperature plasmas. Following Blumenthal *et al.*, we have calculated the intensi-

TABLE I
EMISSION LINES

| ion | $\lambda(\text{\AA})$ | type | mechanism | ion | $\lambda(\text{\AA})$ | type | mechanism | ion | $\lambda(\text{\AA})$ | type | mechanism |
|-------|-----------------------|------|-----------|-------|-----------------------|------|-----------|--------|-----------------------|------|-----------|
| H I | 1026. | R | R,C | N II | 533.7 | R | R,C | O II | 430.1 | R | R,C |
| | 1216. | R | R,C | | 4489. | B | R,C | | 390.3 | B | R,C |
| | 6563. | R | R,C | | 4623. | B | R,C | | 4642. | B | R,C |
| | | | | | 671.5 | R | R,C | | 539.4 | R | R,C |
| He I | 537. | R | R,C | | 1085. | R | C,F | | 539.4 | S | D |
| | 584.3 | R | R,C | | 1085. | S | D,X | | 833.8 | S | C,F |
| | 584.3 | S | D | | 31.60 | S | C,F | | 23.62 | S | C,F |
| | | | | | 2141. | I | R,C | | 3728. | F | C |
| He II | 56.4 | R | R,C | | 6583. | F | C,X | | | | |
| | 303.8 | R | R,C | | | | | O III | 303.8 | R | R,C,B |
| | 1640. | R | R,C | N III | 991.0 | R | C,F | | 3444. | B | R,C,B |
| | 4686. | B | R | | 991.0 | S | D,X | | 3760. | B | R,C,B |
| | | | | | 374.4 | R | R,C,B | | 374.4 | R | R,C,B |
| C II | 1335. | R | C | | 4641. | B | R,C,B | | 374.4 | S | D,X |
| | 1335. | S | D | | 691.4 | B | R,C,B | | 835.0 | R | C,F |
| | 687.2 | R | R,C | | 4099. | B | R,C,B | | 835.0 | S | D,X |
| | 7234. | B | R,C | | 452.1 | R | R,C,B | | 23.14 | S | C,F |
| | 2837. | B | R,C | | 452.1 | S | X | | 1663. | I | R,C |
| | 6580. | B | R,C | | 30.66 | S | C,F | | 5007. | F | C |
| | 858.4 | R | R,C | | 1750. | F | C | | | | |
| | 43.20 | S | C | | | | | O IV | 789.4 | R | C,F |
| | 2326. | F | C | N IV | 765.1 | R | R,C | | 789.4 | S | D |
| | | | | | 765.1 | S | D | | 238.5 | R | R,C |
| C III | 977. | R | R,C,F | | 247.2 | R | R,C | | 3409. | B | R,C |
| | 977. | S | D,X | | 468.7 | B | R,C | | 379.8 | B | R,C |
| | 386.2 | R | R,C | | 1719. | B | R,C | | 3066. | B | R,C |
| | 884. | B | R,C | | 335.0 | B | R,C | | 279.8 | R | R,C |
| | 2296. | B | R,C | | 387.4 | B | R,C | | 22.86 | S | C,F |
| | 5740. | B | R,C | | 30.17 | S | C,F | | 1407. | F | C |
| | 690.0 | B | R,C | | 1488. | I | R,C | | | | |
| | 42.50 | S | C,F | N V | 1240. | R | R,C,A | O V | 629.7 | R | R,C |
| | 1909. | I | R,C,X | | 1240. | S | D | | 629.7 | S | D |
| C IV | 1549. | R | R,C,A | | 209.3 | R | R,C | | 172.2 | R | R,C |
| | 1549. | S | D | | 247.7 | B | R,C | | 286.6 | B | R,C |
| | 312.4 | R | R,C | | 4609. | B | R,C | | 1371. | B | R,C |
| | 384.1 | B | R,C | | 266.3 | B | R,C | | 220.3 | B | R,C |
| | 5805. | B | R,C | N VI | 24.90 | R | R,C | | 248.5 | B | R,C |
| | 419.7 | B | R,C | | 28.80 | R | R,C | | 22.52 | S | C,F |
| | | | | | 28.80 | S | D | | 1218. | I | R,C |
| C V | 34.97 | R | R,C | | 29.53 | F | C,F | O VI | 1034. | R | R,C,A |
| | 40.27 | R | R,C | | 29.08 | I | R,C | | 1034. | S | D |
| | 40.27 | S | D | N VII | 20.94 | R | R,C | | 150.1 | R | R,C |
| | 41.47 | F | C,F | | 24.82 | R | R,C | | 173.0 | B | R,C |
| | 40.73 | I | R,C | | 133.9 | R | R,C | | 3819. | B | R,C |
| C VI | 28.50 | R | R,C | | | | | | 184.1 | B | R,C |
| | 33.78 | R | R,C | O I | 1027. | R | R,C | O VII | 18.63 | R | R,C |
| | 182.3 | R | R,C | | 11287. | B | R,C | | 21.60 | R | R,C |
| N I | 964.4 | R | R,C | | 8447. | B | R,C | | 21.60 | S | D |
| | 9829. | B | R,C | | 1304. | R | R,C | | 22.10 | F | C,F |
| | 8692. | B | R,C | | 1304. | S | D | | 18.63 | I | R,C |
| | 1200. | R | R,C | | 1356. | I | R,C | O VIII | 16.03 | R | R,C |
| | 1200. | S | D | | | | | | 19.00 | R | R,C |
| | 1135. | R | C | | | | | | 102.5 | B | R,C |

TABLE 1—Continued

| ion | $\lambda(\text{\AA})$ | type | mechanism | ion | $\lambda(\text{\AA})$ | type | mechanism | ion | $\lambda(\text{\AA})$ | type | mechanism |
|--------|-----------------------|------|-----------|---------|-----------------------|------|-----------|---------|-----------------------|------|-----------|
| Ne I | 743.7 | R | R,C | Ne VIII | 773.7 | R | R,C,A | Si V | 97.14 | R | R,C |
| | 7489. | B | R,C | | 773.7 | S | D | | 117.9 | R | R,C |
| | 7032. | B | R,C | | 88.13 | R | R,C | | 117.9 | S | F,D |
| | 743.8 | R | R,C | | 93.31 | B | R,C | | 7.117 | S | C,F |
| | 743.8 | S | D | | 2860. | B | R,C | | 240.7 | S | C,F |
| | | | | | 103.0 | B | R,C | | 119.0 | I | R,C |
| Ne II | 461.3 | R | R,C | Ne IX | 11.56 | R | R,C | Si VI | 83.00 | R | R,C |
| | 461.3 | S | C,F,D | | 13.46 | R | R,C | | 99.40 | R | R,C |
| | 14.61 | S | C,F | | 13.46 | S | D | | 247.0 | R | C |
| | 454.4 | F | C | | 13.70 | F | R,C,F | | 247.0 | S | F,D |
| | | | | | 13.70 | I | R,C | | 7.112 | S | C,F |
| Ne III | 251.3 | R | R,C | Ne X | 10.26 | R | R,C | | 100.6 | F | C |
| | 2413. | B | R,C | | 12.16 | R | R,C | | 19608. | F | C |
| | 2678. | B | R,C | | 65.63 | R | R,C | Si VII | 68.00 | R | R,C |
| | 313.4 | R | R,C | | | | | | 85.60 | R | R,C |
| | 313.4 | S | X | Si II | 1814. | R | R,C | | 275.5 | R | C |
| | 489.5 | R | C | | 1814. | S | D | | 275.5 | S | F,D |
| | 489.5 | S | F,C | | 2858. | B | R,C | | 7.063 | S | C,F |
| | 14.52 | S | C,F | | 6355. | B | R,C | | 99.83 | I | R,C |
| | 318.3 | I | R,C | | 1531. | R | R,C | | 2128. | F | C |
| | 3870. | F | C | | 991.7 | R | R,C | Si VIII | 61.00 | R | R,C |
| Ne IV | 172.6 | R | R,C | | 5051. | B | R,C | | 69.60 | R | R,C |
| | 1735. | B | R,C | | 4130. | B | R,C | | 317.7 | R | C |
| | 2362. | B | R,C | | 1263. | R | R,C | | 317.7 | S | F,D |
| | 208.6 | R | R,C | | 2072. | B | R,C | | 7.007 | S | C,F |
| | 542.8 | R | C | | 2325. | F | C | | 1489. | F | C |
| | 542.8 | S | F,D | Si III | 1207. | R | R,C | Si IX | 55.30 | R | R,C |
| | 14.40 | S | C,F | | 1207. | S | F,D,X | | 61.60 | R | R,C |
| | 2425. | F | C | | 566.6 | R | R,C | | 347.4 | R | R,C |
| Ne V | 143.3 | R | R,C | | 5740. | B | R,C | | 347.4 | S | F,D |
| | 1270. | B | R,C | | 823.4 | B | R,C | | 6.947 | S | C,F |
| | 2269. | B | R,C | | 2559. | B | R,C | | 666.6 | I | R,C |
| | 173.9 | R | R,C | | 1313. | B | R,C | | 1888. | F | C |
| | 571.0 | R | C | | 1112. | B | R,C | Si X | 353.1 | R | C |
| | 571.0 | S | F,D | | 3590. | B | R,C | | 353.1 | S | D,F |
| | 14.26 | S | C,F | | 7.124 | S | C,F | | 50.64 | R | R,C |
| | 1127. | I | R,C | | 76.93 | S | C,F | | 54.90 | R | R,C |
| | 3726. | F | C | | 1895. | I | R,C | | 6.850 | S | C,F |
| Ne VII | 561.4 | R | C | Si IV | 1397. | R | R,C | | 14306. | F | C |
| | 561.4 | S | F,D | | 1397. | S | D | Si XI | 307.6 | R | R,C |
| | 122.6 | R | R,C | | 457.9 | R | R,C | | 303.6 | S | F,D |
| | 2224. | B | R,C | | 4098. | B | R,C | | 43.76 | R | R,C |
| | 168.8 | B | R,C | | 560.5 | B | R,C | | 55.81 | B | R,C |
| | 2047. | B | R,C | | 1067. | B | R,C | | 609.8 | B | R,C |
| | 138.6 | R | R,C | | 817.1 | B | R,C | | 49.22 | B | R,C |
| | 14.10 | S | C,F | | 1126. | B | R,C | | 52.23 | B | R,C |
| | 1020. | I | R,C | | 3160. | B | R,C | | 6.780 | S | C,F |
| | 76336. | F | C | | 1724. | B | R,C | | | | |
| Ne VII | 465.2 | R | R,C | | 239.4 | S | C,F | | | | |
| | 465.2 | S | F,D | | 118.1 | S | C,F | | | | |
| | 97.55 | R | R,C | | 7.121 | S | C,F | | | | |
| | 117.0 | B | R,C | | | | | | | | |
| | 127.7 | B | R,C | | | | | | | | |
| | 13.92 | S | C,F | | | | | | | | |

TABLE 1—Continued

| ion | $\lambda(\text{\AA})$ | type | mechanism | ion | $\lambda(\text{\AA})$ | type | mechanism | ion | $\lambda(\text{\AA})$ | type | mechanism |
|---------|-----------------------|------|-----------|--------|-----------------------|------|-----------|--------|-----------------------|------|-----------|
| Si XII | 506.4 | R | R,C,A | S VI | 937.1 | R | R,C | S XIII | 256.7 | R | R,C |
| | 506.4 | S | F,D | | 937.1 | S | D | | 256.7 | S | F,D |
| | 40.92 | R | R,C | | 249.1 | R | R,C | | 32.41 | R | R,C |
| | 44.12 | B | R,C | | 2598. | B | R,C | | 35.70 | S | R,C |
| | 18.75 | B | R,C | | 409.2 | B | R,C | | 37.60 | S | R,C |
| | 45.60 | B | R,C | | 464.6 | B | R,C | | 5.130 | S | C,F |
| Si XIII | 5.680 | R | R,C | | 309.2 | B | R,C | S XIV | 30.43 | R | R,C |
| | 6.650 | R | R,C | | 710.6 | B | R,C | | 30.43 | S | D |
| | 6.650 | S | D | | 1987. | B | R,C | | 32.50 | B | R,C |
| | 6.738 | F | R,C,F | | 649.2 | B | R,C | | 33.50 | B | R,C |
| | 6.680 | I | R,C | | 195.6 | S | C,F | S XV | 4.300 | R | R,C |
| Si XIV | 5.220 | R | R,C | | 72.83 | S | C,F | | 5.040 | R | R,C |
| | 6.180 | R | R,C | | 5.364 | S | C,F | | 5.040 | S | D |
| | 33.39 | R | R,C | S VII | 60.80 | R | R,C | | 6.731 | F | R,C,F |
| S II | 6733. | F | C | | 72.03 | R | R,C | | 5.070 | I | R,C |
| S III | 683.1 | R | R,C | | 72.03 | S | F,C | S XVI | 3.990 | R | R,C |
| | 3840. | B | R,C | | 5.360 | S | C,F | | 4.730 | R | R,C |
| | 2961. | B | R,C | | 197.1 | S | C,F | | 25.54 | R | R,C |
| | 3346. | B | R,C | S VIII | 53.00 | R | R,C | Fe II | 2600. | R | R,C |
| | 1198. | R | C | | 63.30 | R | R,C | | 1608. | R | R,C |
| | 1198. | S | F,D | | 199.9 | R | C | Fe III | 859.2 | R | R,C |
| | 53.22 | S | C,F | | 199.9 | S | F,D | | 859.2 | S | D |
| | 5.372 | S | C,F | | 5.356 | S | C,F | | 208.4 | S | C,F |
| | 77.76 | S | C,F | | 64.11 | F | C | | 383.6 | S | C,F |
| | 1667. | I | R,C | | 9872. | F | C | | 17.34 | S | C,F |
| | 8834. | F | C | S IX | 49.20 | R | R,C | | 16.26 | S | C,F |
| S IV | 1070. | R | C | | 56.10 | R | R,C | | 1.785 | S | C,F |
| | 1070. | S | F,D | | 224.8 | R | C | Fe IV | 526.0 | R | R,C |
| | 836.4 | B | R,C | | 224.8 | S | F,C | | 526.0 | S | D |
| | 3104. | B | R,C | | 5.320 | S | C,F | | 217.8 | S | C,F |
| | 553.1 | R | R,C | | 91.77 | I | R,C | | 321.5 | S | C,F |
| | 661.4 | R | R,C | | 1724. | F | C | | 17.04 | S | C,F |
| | 52.53 | S | C,F | S X | 42.50 | R | R,C | | 15.62 | S | C,F |
| | 5.370 | S | C,F | | 47.70 | R | R,C | | 1.763 | S | C,F |
| | 76.39 | S | C,F | | 257.1 | R | C | Fe V | 387.9 | R | R,C |
| | 1385. | F | C | | 257.1 | S | F,D | | 387.9 | S | D |
| S V | 786.5 | R | R,C | | 5.281 | S | C,F | | 226.5 | S | C,F |
| | 786.5 | S | F,D | | 1305. | F | C | | 317.1 | S | C,F |
| | 290.6 | R | R,C | S XI | 39.90 | R | R,C | | 17.05 | S | C,F |
| | 5.367 | S | C,F | | 41.00 | R | R,C | | 15.59 | S | C,F |
| | 51.66 | S | C,F | | 247.0 | R | C | | 1.762 | S | C,F |
| | 193. | I | R,C | | 247.0 | S | F,D | Fe VI | 294.1 | R | R,C |
| | | | | | 5.239 | S | C,F | | 294.1 | S | D |
| | | | | | 540.5 | I | R,C | | 225.8 | S | C,F |
| | | | | | 1482. | F | C | | 313.1 | S | C,F |
| | | | | S XII | 227.2 | R | C | | 16.97 | S | C,F |
| | | | | | 227.2 | S | F,D | | 15.52 | S | C,F |
| | | | | | 36.50 | R | R,C | | 1.762 | S | C,F |
| | | | | | 37.80 | R | R,C | | | | |
| | | | | | 5.180 | S | C,F | | | | |
| | | | | | 497.5 | F | C | | | | |
| | | | | | 7358. | F | C | | | | |

TABLE 1—Continued

| ion | $\lambda(\text{\AA})$ | type | mechanism | ion | $\lambda(\text{\AA})$ | type | mechanism | ion | $\lambda(\text{\AA})$ | type | mechanism |
|---------|-----------------------|------|-----------|---------|-----------------------|------|-----------|----------|-----------------------|------|-----------|
| Fe VII | 233.8 | R | R,C | Fe XII | 79.50 | R | R,C | Fe XVII | 15.00 | R | R,C |
| | 233.8 | S | D | | 66.10 | R | R,C | | 16.77 | R | R,C |
| | 150.8 | R | R,C | | 195.1 | R | R,C | | 16.77 | S | D |
| | 228.3 | S | C,F | | 357.2 | R | C | | 103.3 | S | C,F |
| | 307.7 | S | C,F | | 357.2 | S | F,D | | 1.941 | S | C,F |
| | 16.89 | S | C,F | | 18.32 | S | C,F | | 15.26 | I | R,C |
| | 15.44 | S | C,F | | 14.83 | S | C,F | Fe XVIII | 14.30 | R | R,C |
| | 1.761 | S | C,F | | 1.752 | S | C,F | | 15.80 | R | R,C |
| Fe VIII | 131.0 | R | R,C | | 2406. | I | R,C | | 104.0 | R | C |
| | 168.5 | R | R,C | Fe XIII | 76.0 | R | R,C | | 104.0 | S | F,D |
| | 168.5 | S | D | | 62.0 | R | R,C | | 1.927 | S | C,F |
| | 303.1 | S | C,F | | 202.0 | R | R,C | | 12.42 | I | R,C |
| | 16.78 | S | C,F | | 360.1 | R | C | | 974.7 | F | C |
| | 15.34 | S | C,F | | 360.1 | S | F,D | Fe XIX | 13.50 | R | R,C |
| | 1.760 | S | C,F | | 18.04 | S | F | | 14.50 | R | R,C |
| Fe IX | 103.6 | R | R,C | | 14.74 | S | F | | 108.0 | R | C |
| | 103.6 | S | F,D | | 1.749 | S | F | | 108.0 | S | F,D |
| | 83.00 | R | R,C | | 517.0 | I | R,C | | 1.917 | S | C,F |
| | 171.1 | R | R,C | | 5438. | F | C | | 17.86 | I | R,C |
| | 298.0 | S | C,F | Fe XIV | 384.4 | R | R,C | | 824.4 | F | C |
| | 16.62 | S | C,F | | 384.4 | R | F,D | Fe XX | 13.40 | R | R,C |
| | 15.21 | S | C,F | | 71.50 | R | R,C | | 13.70 | R | R,C |
| | 1.758 | S | C,F | | 59.30 | R | R,C | | 121.0 | R | C |
| | 105.2 | I | R,C | | 77.00 | B | R,C | | 121.0 | S | F,D |
| | 217.1 | I | R,C | | 215.1 | R | R,C | | 1.907 | S | C,F |
| Fe X | 97.00 | R | R,C | | 95.20 | B | R,C | | 811.9 | F | C |
| | 77.00 | R | R,C | | 14.55 | S | F | Fe XXI | 12.30 | R | R,C |
| | 170.9 | R | R,C | | 1.745 | S | F | | 13.00 | R | R,C |
| | 355.4 | S | F,D | | 17.72 | S | F | | 150.0 | R | C |
| | 18.88 | S | C,F | | 729.8 | F | C | | 150.0 | S | F,D |
| | 15.09 | S | C,F | | 5304. | F | C | | 1.890 | S | C,F |
| | 1.757 | S | C,F | Fe XV | 284.1 | R | R,C | | 278.6 | I | R,C |
| | 97.20 | I | R,C | | 284.1 | S | F,D | | 448.4 | F | C |
| | 6376. | F | C | | 52.80 | R | R,C | Fe XXII | 167.0 | R | C |
| Fe XI | 87.00 | R | R,C | | 65.60 | B | R,C | | 167.0 | S | F,D |
| | 72.70 | R | R,C | | 71.00 | B | R,C | | 11.91 | R | R,C |
| | 92.90 | B | R,C | | 14.36 | S | C,F | | 12.40 | R | R,C |
| | 178.6 | R | R,C | | 17.43 | S | C,F | | 1.890 | S | C,F |
| | 123.5 | B | R,C | | 1.741 | S | C,F | | 401.6 | F | C |
| | 354.5 | R | C | | 418.4 | I | R,C | | 846.0 | F | C |
| | 354.5 | S | F,D | Fe XVI | 360.8 | R | R,C | Fe XXIII | 168.2 | R | R,C |
| | 18.61 | S | C,F | | 360.8 | S | D | | 168.2 | S | F,D |
| | 14.95 | S | C,F | | 50.50 | R | R,C | | 11.19 | R | R,C |
| | 1.754 | S | C,F | | 54.70 | B | R,C | | 11.80 | B | R,C |
| | 1343. | I | R,C | | 66.30 | B | R,C | | 12.24 | B | R,C |
| | | | | | 63.50 | B | R,C | | 1.870 | S | C,F |
| | | | | | 76.60 | B | R,C | Fe XXIV | 10.80 | R | R,C |
| | | | | | 102.5 | S | F | | 10.80 | S | D |
| | | | | | 17.49 | S | F | | 11.20 | B | R,C |
| | | | | | 1.942 | S | F | | 11.38 | R | R,C |
| | | | | | | | | | | | |

TABLE 1—Continued

| ion | $\lambda(\text{\AA})$ | type | mechanism | ion | $\lambda(\text{\AA})$ | type | mechanism | ion | $\lambda(\text{\AA})$ | type | mechanism |
|---------|-----------------------|------|-----------|-----|-----------------------|------|-----------|-----|-----------------------|------|-----------|
| Fe XXV | 1.570 | R | R,C | | | | | | | | |
| | 1.850 | R | R,C | | | | | | | | |
| | 1.850 | S | D | | | | | | | | |
| | 1.868 | F | R,C,F | | | | | | | | |
| | 1.860 | I | R,C | | | | | | | | |
| Fe XXVI | 1.510 | R | R,C | | | | | | | | |
| | 1.790 | R | R,C | | | | | | | | |
| | 9.630 | R | R,C | | | | | | | | |

Key: Line type: R: resonance
 R: subordinate
 S: satellite
 I: intercombination
 F: forbidden

Formation mechanism: R: radiative recombination
 C: collisional excitation
 D: dielectronic recombination
 F: inner shell fluorescence
 X: charge transfer
 B: Bowen resonance fluorescence
 A: Auger

ties of these lines, according to

$$I(\text{forbidden}) = R(^3S)(1 - G_{fi}) + R(^3P)F_{if}, \quad (11)$$

$$I(\text{intercombination}) = R(^3P)(1 - G_{if}) + R(^3S)F_{fi}, \quad (12)$$

where $R(^3S)$ and $R(^3P)$ are the rates into the 3S and 3P levels, G_{fi} (G_{if}) is the fraction of ions excited to 3S (3P) which decay to ground by routes other than direct radiative decay, and F_{if} (F_{fi}) if the fractional probability that an ion in 3P (3S) will decay by the emission of a forbidden (intercombination) line photon. We do not distinguish between the fine structure levels of the 3P level. The singlet series of helium-like ions produce the allowed and two-photon radiation, which are treated in the same way as the forbidden and intercombination lines. Rates for collisional and radiative transitions of these ions are taken from Mewe and Schrijver (1978) and Pradhan, Norcross, and Hummer (1981). Because of the large number of levels involved and the possible importance of $n=2$ level populations, we have neglected the effects of all lines involving transitions between $n=2$ and higher excited levels of helium-like ions.

c) Line Transfer

Emission lines in our models can be divided into two broad categories. Resonance lines, corresponding to allowed transitions to ground ionic level, may be emitted

following collisional excitation or radiative recombination. Allowed transitions to the $n=2$ level of hydrogenic ions are also treated as resonance lines, since the populations of these excited ions are calculated explicitly. Nonresonance lines include subordinate lines, also emitted following collisional excitation or radiative recombination; satellite lines, emitted by dielectronic recombination, K shell fluorescence, or charge transfer; and forbidden and intercombination lines, emitted following collisional excitation or recombination.

The optical depths in the resonance lines of many ions may be very large in X-ray illuminated clouds. Photons emitted near the centers of these lines are likely to be absorbed by the transition which emitted them and reemitted at a new frequency. This line scattering will repeat many times until the photon either escapes the gas, is destroyed, or is degraded into longer wavelength photons which may then escape. Since these processes may either facilitate or impede the radiative cooling of the gas, an accurate treatment of line scattering is important for our models.

Our treatment of resonance line transfer is based on the assumption of complete redistribution. That is, we assume that there is no correlation of photon frequencies before and after each scattering event. This has been shown to be a good approximation for a wide variety of situations, particularly when the line profile is dominated by Doppler broadening. In this case, detailed numerical models (e.g., Hummer and Rybicki 1971) have shown that line scattering is restricted to a small spatial region near the point where the photons are emitted. Line photons first scatter to a frequency such that the gas cloud is optically thin and then escape in a single long

flight. The probability of escape per scattering depends on the optical depth, τ_0 , at the center of the line (London 1979). For $1 \leq \tau_0 \leq 10^6$, the resonant trapping is effectively local. For $\tau_0 \geq 10^6$, the lines become optically thick in the damping wings, and the line escapes as a result of diffusion in both space and frequency. Since the scattering in the Doppler core is always dominated by complete redistribution, and since most of the lines in our models are optically thin in the wings, we assume that all line scattering takes place in the emission region.

In our treatment of line transfer, we have assumed that spectral lines are broadened by thermal Doppler motions. When velocity gradients are large, spectral line trapping and its effects are reduced. If the velocity gradients were known, their effects could be calculated by replacing the thermal escape probabilities used here by Sobolev escape probabilities (Castor 1970). The results of such calculations would be intermediate between those of models calculated here with thermal escape probabilities and those without line trapping.

Line photons are removed by thermalization, splitting, escape, photoabsorption, and Compton scattering. For all ions other than hydrogenic and helium-like, we neglect collisional transfer between excited levels, so that the probability of thermalization per scattering is

$$P_{\text{th}} = [1 + A_{ug}/(n_e C_{ug})]^{-1}, \quad (13)$$

where n_e is the electron number density, C_{ug} is the collisional de-excitation rate coefficient, and A_{ug} is the radiative decay rate for the transition between excited and ground levels. Line splitting occurs when the upper level decays by a route other than directly back to ground. An example is the decay of the $n=3$ level of hydrogenic ions with the emission of $H\alpha$ and $Ly\alpha$ photons. The probability of this process per $Ly\beta$ scattering is simply

$$P_{\text{sp}} = 1 - A_{ug}/A_u, \quad (14)$$

where A_u is the net radiative decay rate to all levels from level u . For the escape probability, we take (Hollenbach and McKee 1978)

$$P_{\text{esc}} = \frac{1 - P_{\text{th}} - P_{\text{sp}}}{1 + \tau_0 [2\pi \ln(2.13 + \tau_0^2)]^{1/2}}, \quad (15)$$

where τ_0 is the optical depth at line center. This probability, although derived for uniform plane-parallel slabs, is sufficiently accurate for our purposes. Photons are removed from the line core by continuum opacity with a probability per scattering given by Hummer (1968):

$$P_{\text{cont}} = (1 - P_{\text{th}} - P_{\text{sp}})\beta F(\beta), \quad (16)$$

where $\beta = \kappa/\kappa_0$, the ratio of continuum opacity to line

center opacity, and

$$F(\beta) = 2(-\ln \beta \sqrt{\pi})^{1/2} + \frac{1}{\beta} \operatorname{erfc}[(-\ln \beta \sqrt{\pi})^{1/2}]. \quad (17)$$

Continuum opacity results from photoabsorption and Compton scattering, with probabilities

$$P_{\text{abs}} = (\kappa_{\text{abs}}/\kappa) P_{\text{cont}}, \quad (18)$$

and

$$P_{\text{C}} = (\kappa_{\text{C}}/\kappa) P_{\text{cont}}, \quad (19)$$

respectively. Here κ_{abs} is the photoabsorption opacity, κ_{C} is the Compton opacity, and $\kappa = \kappa_{\text{abs}} + \kappa_{\text{C}}$. Since the electron thermal velocity exceeds the ion velocity by $\sqrt{M}/\sqrt{m_e}$, where m_e is the electron mass and M is the ion mass, Compton scattering is tantamount to escape, and the scattered radiation will appear as a narrow once-Comptonized profile in the vicinity of the line core (Illarionov *et al.* 1979).

Special treatment is required for the lines involved in the Bowen resonance fluorescence mechanism, in which a frequency coincidence allows photons emitted in the He II $Ly\alpha$ line, near 304 Å, to be absorbed by a line of O III. The O III upper level may decay by an alternate route, producing two near-UV photons and a photon near 374 Å. A further coincidence allows the latter photon to be absorbed by N III, followed by conversion to optical line radiation near 4640 Å. When the optical depth in He II $Ly\alpha$ is large, the Bowen mechanism can be an important escape route for $Ly\alpha$ radiation. This is borne out by optical observations which indicate that $\lambda 4640$ is often one of the brightest features in the optical spectra of X-ray sources (McClintock, Canizares, and Tarter 1975). In our models we calculate the intensities of the O III and N III Bowen lines using the theory of Kallman and McCray (1980).

The rates for line emission and the probabilities for the various resonance line escape and destruction probabilities depend on the state of the gas at each point in the cloud. The cooling function for the gas depends on the line escape probabilities, and the effects of line trapping must be incorporated in the solution for the temperature and ionization of the gas. Once the state of the gas at a given point has been determined, a fraction of the radiation emitted in each resonance line corresponding to the fractional probability of escape plus Compton scattering is assumed to escape the vicinity of the emission point. We treat the photoabsorption of this radiation as it traverses the rest of the cloud in the same way as the continuum at that energy (see § V). A fraction of the radiation in each resonance line corresponding to the fractional splitting probability for that

line is reemitted in the corresponding subordinate and resonance lines.

V. COMPUTATIONAL PROCEDURE

The equations of statistical and thermal equilibrium constitute a set of 92 coupled nonlinear equations. The solution of this system, for a given local radiation flux, is developed as follows. We note that, for a given temperature and electron number density, the ionization equilibrium equations for each element constitute a linear system which may be solved by a simple analytic technique (Weisheit 1974). Then the ion abundances can be regarded as functionals of the temperature and electron number density, leaving the thermal equilibrium and charge conservation equations as a coupled nonlinear system in two variables. These two equations are solved by a Newton-Raphson or secant technique to give the temperature and electron number density. Using this procedure, we obtain a result which includes all the contributions to heating and cooling self-consistently. This procedure is more accurate and efficient than that used by HBM, in which only a subset of the ions was included in the thermal balance calculation.

Construction of a model of an X-ray illuminated cloud consists of the simultaneous solution of the local balance equations, determining the state of the gas, and the radiative transfer equation, determining the radiation field. The local balance equations include corrections to the cooling due to the trapping of resonance line radiation and corrections to the ionization and thermal balance due to ionization and excitation from $n = 2$ levels of hydrogenic ions. The radiative transfer equation is solved for both the continuum and for the lines that escape the region near the point of emission. The large number of ions in the calculation results in many ionization edges that may affect the radiation field. We solve the transfer equation on a frequency grid that includes slightly more than one grid point per edge, resulting in a total of 299 continuum grid points ranging in energy from 1.4 eV to 100 keV. We calculate the luminosities of 530 spectral lines and solve the continuum transfer equation individually for each of these. The emissivity of each line at each point is the product of the emissivity discussed in § IVb and the local escape fraction for that line, as discussed in § IVc. The continuum opacity for each line is the opacity calculated for the energy bin that contains the line. For photon wavelengths $\lambda > 912 \text{ \AA}$, we include the effects of absorption due to the Balmer continuum of hydrogen but neglect absorption by ions of trace elements that have thresholds below 13.6 eV.

A model is constructed by dividing the cloud into a set of concentric spherical shells. The radiation field incident on the innermost shell is the source spectrum. For each shell, starting with the innermost one, the ionization and temperature structure is calculated from

the local balance equations using the radiation field incident on the inner surface. The radiation field is then transferred through the shell. We solve a simplified version of the transfer equation, which is based on the approximation that the radiation produced at any point in the cloud will eventually move in the radially outward direction. This approximation is reasonable in a spherical nebula in which opacity at any wavelength increases with radius, provided that the scattering optical depths are not large. Under this assumption, the transfer equation may be written

$$\frac{dL_\epsilon}{dR} = -\kappa(\epsilon)L_\epsilon + 4\pi R^2 j_\epsilon, \quad (20)$$

where L_ϵ is the luminosity, $\kappa(\epsilon)$ is the opacity, and j_ϵ is the emissivity at the radius R . The transfer equation is solved using a simple one-step forward differencing formula (HBM),

$$L_\epsilon(R + \Delta R) = L_\epsilon(R) e^{-\kappa(\epsilon, R)\Delta R} + 4\pi R^2 j_\epsilon(R) \frac{(1 - e^{-\kappa(\epsilon, R)\Delta R})}{\kappa(\epsilon, R)}, \quad (21)$$

where R is the radius at the inner edge of the shell and ΔR is the shell thickness. This procedure is repeated for each successive shell with increasing radius.

The resonance line escape probabilities depend on the ionization structure of the model. Therefore, in cases where line trapping is important, we first calculate a model with estimated escape probabilities and then iterate with escape probabilities calculated from results of the previous model. We iterate by using the column densities computed from the previous iteration to calculate resonance line optical depths to the edge of the cloud. We construct the ion column densities as functions of the ion abundances, $N_i(n_i)$, from the results of the previous iteration. These functions are multiple valued since, for ions which are not abundant at either the inner or the outer boundaries of the cloud, a given value of n_i occurs at least two values of ξ and of total column density N_i . The multiple-valued nature of these functions is suppressed by requiring that N_i always decrease with decreasing ξ . Then, at each radius step the ion abundances are calculated, and the column densities n_i are obtained from the functions $N_i(n_i)$. This iterative procedure is found to converge very rapidly—on the third iteration the ion column densities change less than 2%.

VI. RESULTS

The X-ray nebular models are sensitive to many parameters, including central source luminosity, L ,

TABLE 2
LIST OF MODELS

| Model | Source Luminosity L (ergs s $^{-1}$) | Spectral Shape | Gas Density n (cm $^{-3}$) |
|---------|--|---|----------------------------------|
| 1 | 10^{37} | 10 keV bremsstrahlung | 1 (optically thin) |
| 2 | 10^{37} | 10 keV bremsstrahlung | 10^3 |
| 3 | 10^{37} | 10 keV bremsstrahlung | 10^{11} (no line trapping) |
| 4 | 10^{37} | 10 keV bremsstrahlung | 10^{11} |
| 5 | 10^{37} | 10 keV bremsstrahlung + 30,000 K blackbody | 10^{11} |
| 6 | 10^{37} | 2 keV bremsstrahlung | 10^{11} |
| 7 | 10^{37} | ν^{-1} power law | 10^{11} |
| 8 | 10^{37} | 4 keV blackbody | 10^{11} |

source spectrum, f_e , and gas density, n . Further, the models embody many competing physical processes and generate a great quantity of information: ion abundances, temperature, line luminosities, and continuous spectrum as functions of R , the distance from the source. In this section we present a range of model results which may be interpolated or extrapolated to a specific astrophysical system, in sufficient detail that the reader will be able to find appropriate principles for such interpolation.

In order to illustrate the general properties of our models and to make contact with previous work, this section is organized as follows: the basic model has a spectrum appropriate to a compact galactic X-ray source, and we start with the simplest case, corresponding to the limit of low gas densities. The model complexity increases with increasing gas densities, for which radiation transfer becomes important. The dependence of the model results on the input spectrum is also explored. Table 2 lists the parameters of the models that we shall present. In every case the source luminosity is chosen to be 10^{37} ergs s $^{-1}$, typical of a luminous galactic compact X-ray source. Models 1–4 all have a central source spectrum given by $f_e = 1/kT_{\text{rad}} \exp(-\epsilon/kT_{\text{rad}})$, where $kT_{\text{rad}} = 10$ keV. Model 5 has an additional contribution to the source spectrum to illustrate the effects of a strong source of ionizing ultraviolet radiation, such as an OB star. Model 6 illustrates the effects of a reduced X-ray source temperature, and model 7 shows results for a power-law spectrum, $f_e \approx \epsilon^{-1}$. Model 8 has a blackbody spectrum and illustrates the multiple solutions for the gas state that may occur when the source spectrum is deficient in soft X-rays. In § VIi we consider a few additional optically thin models.

a) Model 1: Optically Thin Gas

This model illustrates the gas structure that results from X-ray heating and ionization in the absence of absorption and scattering of the incident X-rays by the gas. The computational procedure is the same as that outlined in §§ III–V, but all radiation emissivities and

opacities are set to zero. The assumptions are the same as those of TTS and of Buff and McCray (1974a), although the atomic processes are included in much better detail. Model 1 best approximates the physical conditions in a gas cloud surrounding a source such that the product, Ln is small, for example, in interstellar gas surrounding a compact galactic source.

For an optically thin model with a given source spectral shape, f_e , the ionization and temperature structure of the gas are determined only by the parameter $\xi = L/nR^2$. This scaling law is broken by the collisional suppression of forbidden lines (Osterbrock 1974) for atomic densities, $n > 10^3$ cm $^{-3}$, and at much greater densities ($n > 10^9$ cm $^{-3}$) by the collisional suppression of dielectronic recombination. However, since the forbidden lines never have a dominant effect on the state of the gas, this scaling law remains approximately valid over a wide range of densities.

Figure 1a, b shows the ionization structure of the optically thin model 1. Here the relative abundances of all the ions of each element are plotted as a function of the parameter $\log(\xi) = \log(L/nR^2) = 37 - 2 \log[R(\text{cm})]$, so that large values of ξ correspond to small R and the source lies at the right-hand side of the figure, at $\xi = \infty$. At small R , corresponding to $\log \xi \geq 5$, the gas is fully photoionized. At larger radii, or smaller ξ , the radiation intensity decreases due to geometrical dilution, and recombination occurs. For a given gas temperature, the value of ξ where a given ion, i , recombines can be estimated by equating the rates for photoionization and recombination to give

$$(\xi_i)_r = \frac{4\pi\alpha_i}{\gamma_i}, \quad (22)$$

where α_i is the recombination coefficient and γ_i is the photoionization rate coefficient normalized to unit source luminosity, i.e.,

$$\gamma_i = \int_{\epsilon_i}^{\infty} f_e \sigma_i(\epsilon) \frac{d\epsilon}{\epsilon}, \quad (23)$$

where ε_i is the ionization threshold and $\sigma_i(\varepsilon)$ is the photoionization cross section. For example, equation (22) yields $\log(\xi_i)_r = 3.5$ for the recombination of hydrogenic iron, Fe xxvi, which is in accord with the results shown in Figure 1. Such simple estimates become less accurate at larger radii, or smaller ξ , due to the variety of atomic processes that affect the state of the gas. Dielectronic recombination causes the recombination rate to increase with temperature over a narrow range of temperatures, leading to the anomalous appearance of the ion abundance curves of Ne, Si, and S near $\log \xi = 2$. In this regime, the dielectronic recombination rates of the dominant ions exceed the radiative rates by factors ~ 5 .

At small $\log \xi$, where hydrogen and helium become neutral, the ionization of the trace elements is affected by charge transfer reactions with these atoms. The rates for these reactions can exceed the rates for radiative and dielectronic recombination by factors up to $\sim 10^4$ and strongly couple the abundances of many of the ions in the gas to the hydrogen and helium neutral fractions. Charge transfer dominates radiative recombination for most ions in the region $\log \xi \leq -1.0$, where significant abundances of H I and He I appear. The outstanding exceptions are Ne II and S III, which have anomalously low charge transfer rate coefficients and therefore survive far into the H I region.

The Auger effect is most noticeable in the ionization curves for silicon, where the abundance of Si III is very low because a single photon changes Si II to Si IV, and the recombination rate of Si III exceeds that of Si IV.

The temperature structure for model 1, together with the rates for the various processes that dominate the thermal balance in the gas, are shown in Figure 2. In the region where the gas is fully ionized, near $\log \xi \approx 5$, the thermal balance is dominated by heating and cooling due to Compton scattering. The rates for these processes far exceed any other heating or cooling process in this region of the gas; therefore, only the difference between the Compton heating and cooling (eq. [5]) is shown as the curve labeled Compton heating in Figure 2. The gas temperature T in this region can be estimated by equating the net Compton heating-cooling $\Gamma_c \approx 0$ in equation (5). For an exponential source spectrum with $kT_{\text{rad}} \leq 50$ keV, the result is $T \approx T_{\text{rad}}/4$. Therefore, for models 1–4, in which $kT_{\text{rad}} = 10$ keV, the asymptotic gas temperature near the source is $T \approx 2.2 \times 10^7$ K. Further from the source, for $\log \xi \leq 3.5$, the gas is not fully ionized, and photoionization of trace ions replaces Compton scattering as the dominant heating mechanism, since the photon energy loss per photoabsorption is much greater than the energy loss per Compton scattering. Iron ionization dominates the heating for $\log \xi \approx 3.2$, and photoionization of oxygen, helium, and hydrogen successively dominate the heating at smaller ξ . Previous calculations of this type, such as those by

HBM, did not include the effects of iron photoionization heating.

In addition to Compton scattering, the gas temperature is affected by bremsstrahlung cooling over a large portion of the cloud. This process accounts for the difference between Compton heating and cooling in the region near $\log \xi \approx 5$ and balances photoionization heating for $\log \xi \approx 3$. The value of ξ at which Compton cooling equals bremsstrahlung cooling may be estimated from equations (5) and (6): $\xi T^{1/2} \approx 4 \times 10^7$, or $\log \xi \approx 4$, in rough agreement with Figure 2. As $\log \xi$ decreases, the cooling is dominated by collisional excitation of the resonance lines of lithium-like iron, He II, lithium-like oxygen, carbon, and hydrogen successively. In the region where the gas is predominantly neutral, near $\log \xi = -3$, the cooling is also affected by collisional excitation of fine structure lines of trace elements, such as [N II] $\lambda 6583$, [O II] $\lambda 3728$, and [S II] $\lambda 6733$.

Figure 2 also shows the ratio of the radiation pressure in the gas to the radiation pressure that would obtain in the presence of Compton scattering alone. This radiation pressure multiplier is given by (HBM; Tarter and McKee 1973)

$$\beta = 1 + \frac{1}{1.2 \sigma_T n} \int_0^\infty \kappa(\varepsilon) f_\varepsilon d\varepsilon, \quad (24)$$

where σ_T is the Thomson scattering cross section and $\kappa(\varepsilon)$ is the photoelectric opacity. In the absence of absorption of the radiation, this multiplier approaches $\beta \approx 10^4$, and the gas will feel a net outward force if the source luminosity $L \geq \beta^{-1} L_E$, where L_E is the Eddington limit.

The results presented here for model 1 are in good agreement with previous calculations of the same type, such as those by Buff and McCray (1974a), TTS, and HBM. Important differences in the ionization structure exist for $\log \xi < 1$ as a result of charge transfer and the Auger effect. Significant increases in accuracy result from a better computational procedure and better treatment of atomic processes, especially the heating and cooling due to iron. All of our photoionization rates are calculated using a photon energy grid which has approximately 6 times as many points as that of HBM.

b) Model 2: Low Density Gas

The optically thin model is valid only if Ln , the product of the source luminosity and the gas density, is very small. For greater values of this parameter the cloud structure is affected by radiative transfer. In order to illustrate the onset of these effects, we now discuss model 2 which has a low, but significant, value of Ln . Model 2 has a gas density of $n = 10^3 \text{ cm}^{-3}$, the same input spectrum as model 1, and employs the full treatment of radiative transfer and resonance line trapping that was described in §§ III–V. This combination of

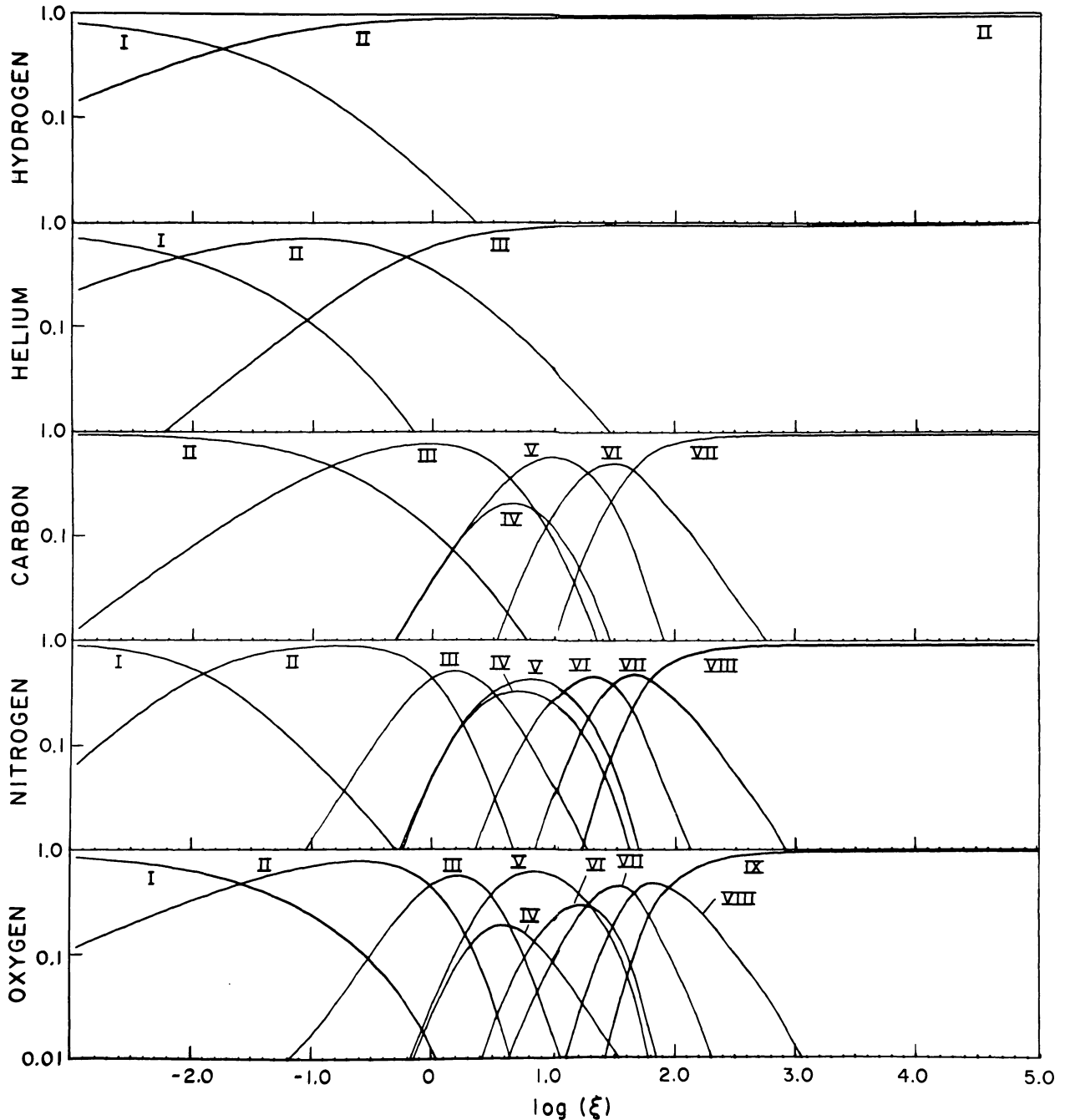


FIG. 1a

FIG. 1.—Ionization structure of model 1. Relative abundances of the ions of each element are shown as a function of $\log \xi$ for $-3 < \log \xi < 5$.

input parameters makes model 2 representative of a compact source embedded in a dense interstellar cloud (Halpern and Grindlay 1980).

The gas structure in model 2 over a large portion of the cloud is the same as in the optically thin case. This is apparent in Figures 3 and 4, which show, respectively, the ionization and temperature structure of model 2 as a function of $\log \xi = 34 - 2 \log [R(\text{cm})]$. The results coin-

cide with the results of model 1 for $\log \xi \geq 1.0$. For lower values of $\log \xi$, photoabsorption in the ionizing continua of He II, He I, and H I, respectively, results in the recombination of He II at $\log \xi \approx +0.1$ and the recombination of hydrogen at $\log \xi \approx -0.1$. In the H I zone there are few photons between 13.6 and 100 eV and consequently a low direct photoionization rate for most ions. Ionization of hydrogen in this region is dominated

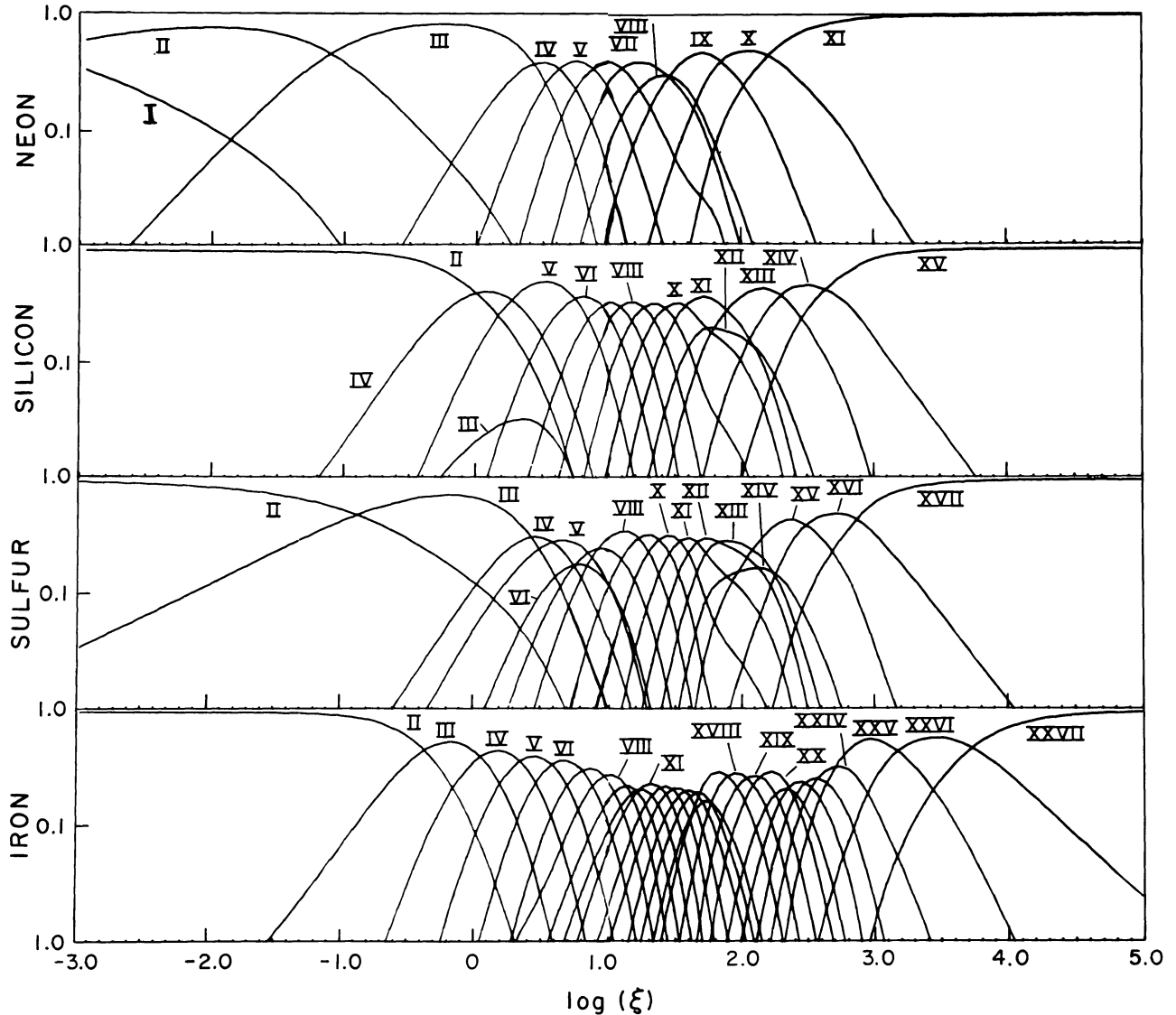


FIG. 1b

by collisions with fast photoelectrons and Auger electrons, which are produced by high energy photons. Photoabsorption also causes a reduction in the radiation pressure multiplier, β , for $\log \xi \leq 0$, as shown in Figure 4.

Figure 5 shows the radiation spectrum of model 2, in the neutral region at $\log \xi = -1$. The spectrum is displayed with an energy resolution $\epsilon/\Delta\epsilon = 100$; only the low energy range ($\epsilon < 100$ eV) is displayed, because the X-ray spectrum for this model is devoid of spectral features except photoelectric absorption for $\epsilon \leq 200$ eV. The dashed line indicates the source spectrum. The source continuum spectrum for $13.6 < h\nu \leq 200$ eV is removed by photoabsorption due to hydrogen and helium. The photon luminosities of the strongest emission lines are also listed, sorted according to wavelength. At the energy resolution assumed, the logarithm of the luminosity spectrum ($\text{ergs s}^{-1} \text{ ergs}^{-1}$) of emission lines

displayed in the graph equals the listed logarithm of the photon luminosity (s^{-1}) plus 2.0. Important emission lines include hydrogen $H\alpha$, $L\gamma$, and the forbidden lines [O III] $\lambda 5007$, [N II] $\lambda 6583$, and [S II] $\lambda 6733$. Halpern and Grindlay (1980) have calculated models with input parameters similar to our model 2, but their assumed source spectrum is cut off at energies below 1 keV, so that, at a given radius, their models are less ionized than ours. Comparison of the emission spectra of the two models shows that the line luminosities are generally greater in the models of Halpern and Grindlay, since the strongest lines are formed in the less ionized gas.

We shall now derive some analytic estimates which help to explain the behavior of this and succeeding models. The onset of optical depth effects as L_n increases can be understood as follows. In the optically thin limit, the value of ξ where a given ion recombines is given by equation (22). In the optically thick limit, ion i

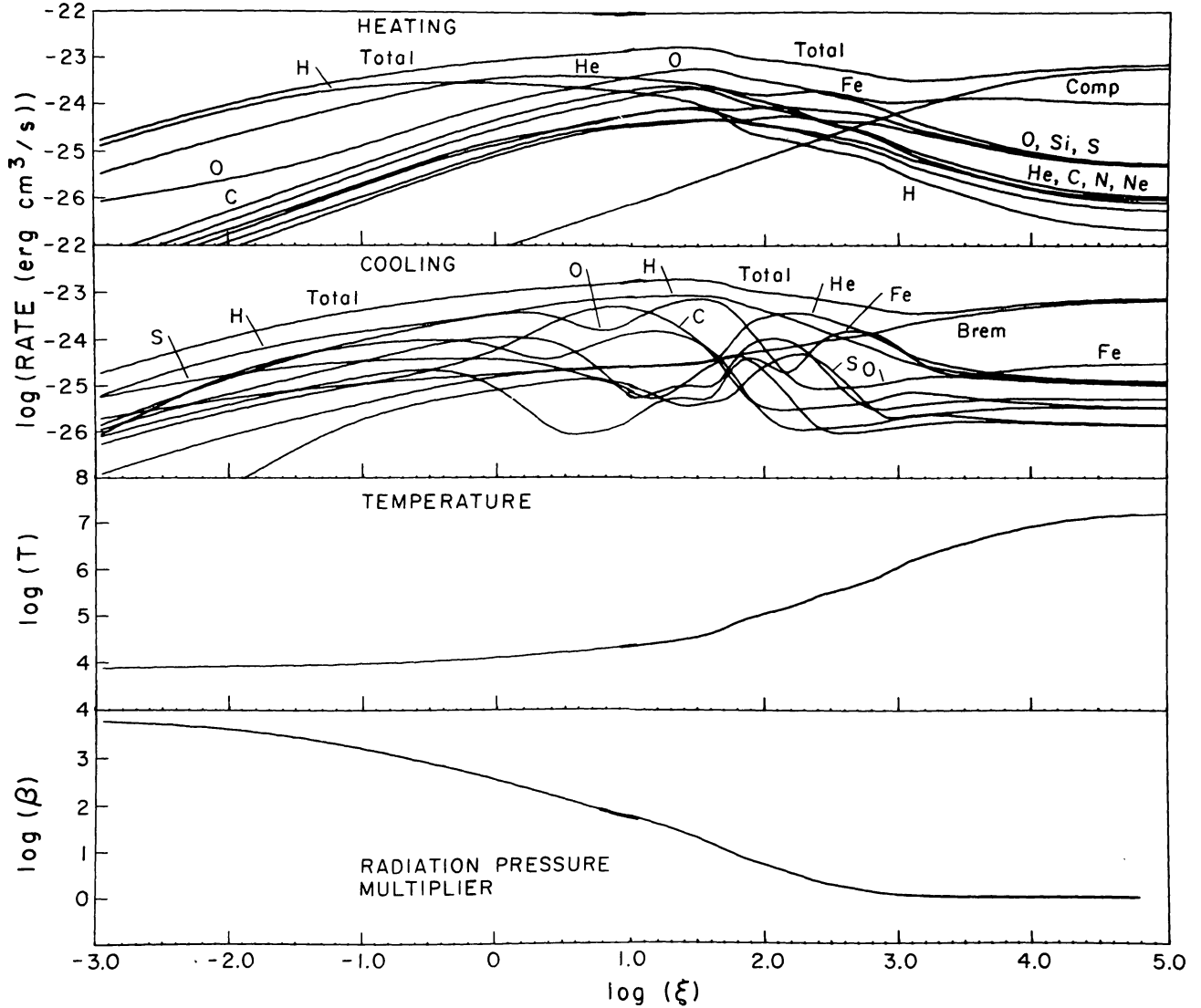


FIG. 2.—Thermal structure of model 1. Heating rates, cooling rates, temperature, and radiation pressure multiplier are shown as a function of $\log \xi$ for $-3 < \log \xi < 5$. Total heating and cooling rates, together with contributions due to Compton scattering, bremsstrahlung emission, and line and continuum radiation from each separate element, are shown.

recombines at roughly the Strömgren radius, where

$$(\xi_i)_S = \left[\left(\frac{4\pi\alpha_i}{3\eta_i} \right)^2 Ln \right]^{1/3}, \quad (25)$$

and $\eta_i = \int_{\xi_i}^{\infty} f_e d\xi$. In general, recombination will occur at the greater of $(\xi_i)_S$ and $(\xi_i)_r$ (eq. [22]). If Ln is small, $(\xi_i)_S$ is negligible, and recombination occurs at $(\xi_i)_r$, but if Ln is large, $(\xi_i)_S$ determines the cloud structure. The transition between the two regimes can be estimated by defining $(Ln)_{crit}$, such that $(\xi_i)_S = (\xi_i)_r$, or

$$(Ln)_{crit} = \frac{(3\eta_i)^2 4\pi\alpha_i}{\gamma_i^3}. \quad (26)$$

Note that $(Ln)_{crit}$ is an increasing function of the ionic charge.

The fractional range of ξ over which a given ion predominates is independent of Ln for both the optically thin and thick cases. In the optically thin case, we define

$$\Delta \log (\xi_i)_r = \log (\xi_i)_r - \log (\xi_{i-1})_r = \log \left[\frac{\alpha_i \gamma_{i-1}}{\gamma_i \alpha_{i-1}} \right], \quad (27)$$

and in the optically thick case,

$$\Delta \log (\xi_i)_S = \log (\xi_i)_S - \log (\xi_{i-1})_S = \frac{2}{3} \log \left(\frac{\eta_{i-1} \alpha_i}{\eta_i \alpha_{i-1}} \right). \quad (28)$$

Both $\Delta \log (\xi)_r$ and $\Delta \log (\xi)_s$ depend only on atomic constants and on the shape of the input spectrum.

The ion column densities depend on Ln in both the optically thin and optically thick cases. The column density is

$$N_i \approx n \Delta R \approx (Ln)^{1/2} \frac{\Delta \xi}{\xi^{3/2}} \approx (Ln)^{1/2} \xi^{-1/2} \Delta \log \xi, \quad (29)$$

so, in the optically thin case,

$$N_i \approx (Ln)^{1/2} \Delta \log (\xi)_r. \quad (30)$$

In the optically thick case,

$$N_i \approx (Ln)^{1/3} \Delta \log (\xi)_s. \quad (31)$$

Although these simple estimates neglect many important effects, such as temperature variations in the cloud and atomic processes other than photoionization and recombination, they explain the scaling behavior that is seen in model 2 and in later models.

c) Model 3: High Density Gas without Line Trapping

We now explore the effects of further increasing the value of Ln . As shown in the previous section, the ion column densities and the cloud optical depths will increase monotonically with Ln . Therefore, for a given value of ξ , we expect that increasing Ln will (1) increase the total optical depth in the cloud; (2) increase the sharpness of the ionization fronts in the optically thick region; and (3) increase the importance of secondary emission by increasing the column densities of the emitting ions. These effects are illustrated by model 3, which has a gas density $n = 10^{11} \text{ cm}^{-3}$, the same input spectrum as models 1 and 2, and includes the effects of continuum transfer but *not* the effects of resonance line trapping. Such a model might be applicable to a compact source in a stellar wind or an accretion flow, if the velocity gradients in the wind are large enough to render all resonance line optical depths negligible.

The ionization structure of model 3 is shown on an expanded scale in Figure 6a, b as a function of $\log \xi = 26 - 2 \log [R(\text{cm})]$. The gas is optically thin for $\log \xi > 2.0$, and the ionization structure in this region is almost identical to that of models 1 and 2. At smaller ξ , the gas becomes optically thick in the ionizing continua of C VI, O VIII, He II, and hydrogen. Ionization fronts of He II and hydrogen occur at $\log \xi = 1.8$ and 1.5, respectively. In the region between the fronts, the gas consists primarily of ions with photoionization thresholds greater than 54.4 eV: C IV, N IV, O III, Ne III, Si V, S V, and Fe IV. Secondary emission of He II Ly α by the gas is

important in controlling the ionization in this region. At the H I front a slight increase in the ionization of trace elements occurs, due to the decreased electron abundance (McClintock, Canizares, and Tarter 1975). In the zone beyond the hydrogen ionization front, $\log \xi \lesssim 1.5$, the gas is kept $\sim 15\%$ ionized by fast photoelectrons and Auger electrons.

The ionization equilibrium in the neutral zone of model 3 and that of the optically thin model 1 differ markedly. In the optically thin case, the radiation field in this region is determined by dilution of the incident radiation field, so that the intensity in all wavelength bands decreases with decreasing ionization parameter, ξ . In the optically thick case, the radiation field in the neutral zone is deficient in low energy ($13.6 \text{ eV} < \epsilon \lesssim 0.2 \text{ keV}$ or so) photons, so that the ionization is controlled by hard X-rays. Collisional ionization by secondary electrons and inner shell ionization followed by Auger decays are the dominant processes. The majority of trace element ionization events cause the ion charge to change by two or more, resulting in qualitatively different ion abundances in the neutral zones of models 1 and 3. For example, in the neutral zone of model 3, C III is less abundant than that in model 1 by a factor ~ 10 , owing to the shortage of low energy photons required to convert C II to C III. On the other hand, Ne III, produced by Auger decay following K shell ionization of Ne I, is very much more abundant in this neutral zone of model 3 than in the neutral zone of model 1.

The effects of radiative transfer are also apparent in the thermal balance of model 3, as shown in Figure 7. For $\log \xi > 2.0$, the heating and cooling are the same as in model 1. At the He II ionization front, near $\log \xi \approx 1.8$, the heating peaks sharply as the photons in the He II Lyman continuum are absorbed. In the He II zone ($1.5 < \log \xi < 1.8$), heating due to hydrogen photoionization is dominant. In the neutral zone, $\log \xi < 1.5$, the photons with $\epsilon \lesssim 1\text{--}2 \text{ keV}$ in the hydrogen Lyman continuum have been removed, and the heating is affected by X-ray photoionization of oxygen.

The cooling in model 3 is dominated by line emission: He II Ly α collisional excitation and recombination emission for $1.8 < \log \xi < 2.6$; O VI $\lambda 1034$ collisional excitation for $\log \xi \approx 1.75$; C IV $\lambda 1549$ collisional excitation for $1.5 < \log \xi < 1.7$; and hydrogen Ly α collisional excitation for $\log \xi < 1.5$. The C IV and hydrogen Ly α cooling functions are very sharply increasing functions of temperature, causing the gas to be nearly isothermal in the regions where these ions dominate the cooling.

The radiation pressure multiplier, β , shown in Figure 7, has two components in model 3—that due to photoabsorption of continuum radiation, and that due to photoabsorption of line radiation. The continuum component shows a peak at $\log \xi = 1.8$, with a decrease at smaller ξ due to absorption of the ionizing continuum photons. The conversion of the absorbed continuum photons into lines is apparent in the line contribution to

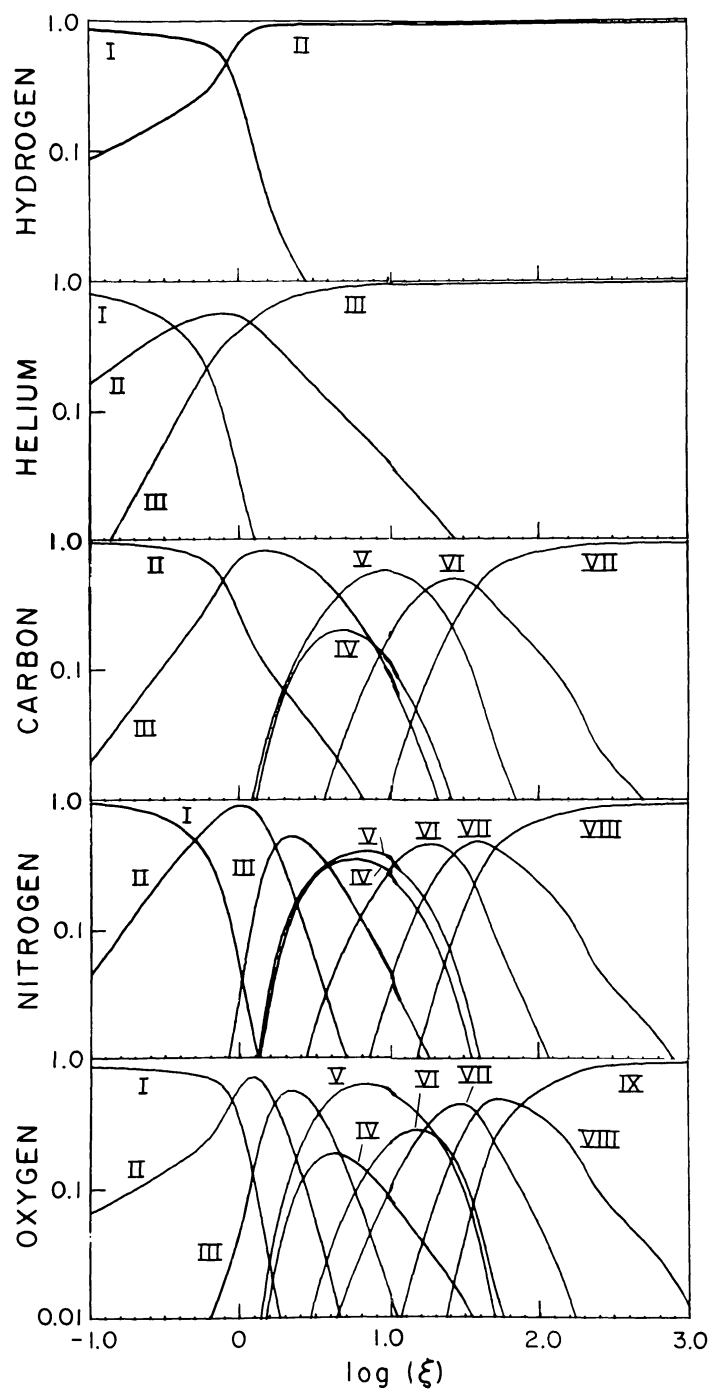


FIG. 3a

FIG. 3.—Ionization structure of model 2. Relative abundances of the ions of each element are shown as a function of $\log \xi$ for $-1 < \log \xi < 3$. Curves for $\log \xi > 3$ are almost identical to those of Fig. 1a, b.

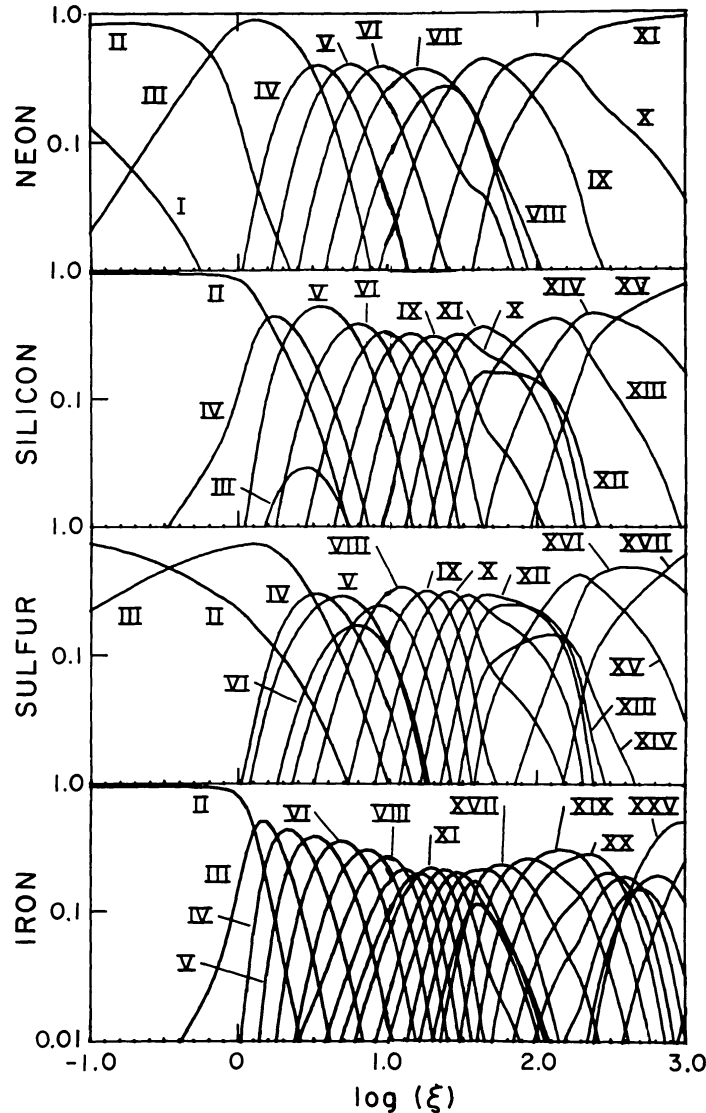


FIG. 3b

the pressure multiplier. This component actually dominates the pressure for $1.5 < \log \xi < 1.7$, the most important line being He II Ly α .

The results of model 3 can be understood in terms of a flow of photons to lower energy with decreasing ξ . Moving away from the source, the gas becomes optically thick in the continua of O VIII, C VI, and He II, respectively. Photons absorbed in these energy ranges are reemitted as lines and recombination continua at lower energies. Figure 8a, b shows the radiation spectrum at $\log \xi = 1.8$, where model 3 is optically thick in the He II Lyman continuum but not yet in the He I and H I continua. He II absorption is apparent between 54.4 and 150 eV, and photoabsorption of the K edge of oxygen near 800 eV is just becoming apparent in the X-ray spectrum of Figure 8b. The strongest X-ray emission lines are those of hydrogen and helium-like carbon and oxygen. The EUV emission spectrum of Figure 8a

is dominated by the resonance lines of abundant ions formed primarily by recombination: He II Ly α , O v $\lambda 630$, and Ne VIII $\lambda 774$. The ultraviolet and optical emission line spectrum is dominated by the recombination lines H α , He II $\lambda 4686$, He II $\lambda 1640$, Ly α , and collisionally excited O VI $\lambda 1034$.

At greater radii the cloud becomes optically thick in the Lyman continuum of hydrogen; most of the extreme ultraviolet radiation is absorbed and reemitted in the form of optical and ultraviolet lines and continua with wavelengths greater than 912 Å. This process is illustrated in Figure 9 which shows that the luminosity lost by He II $\lambda 304$ at $\log \xi < 1.8$ is replaced by that of optical and UV lines. Note that the strengths of UV lines from ions such as He II, C III, and C IV remain at their maximum values once the ions recombine, while Ly α and H α continue to increase in the H I region as more X-rays are absorbed.

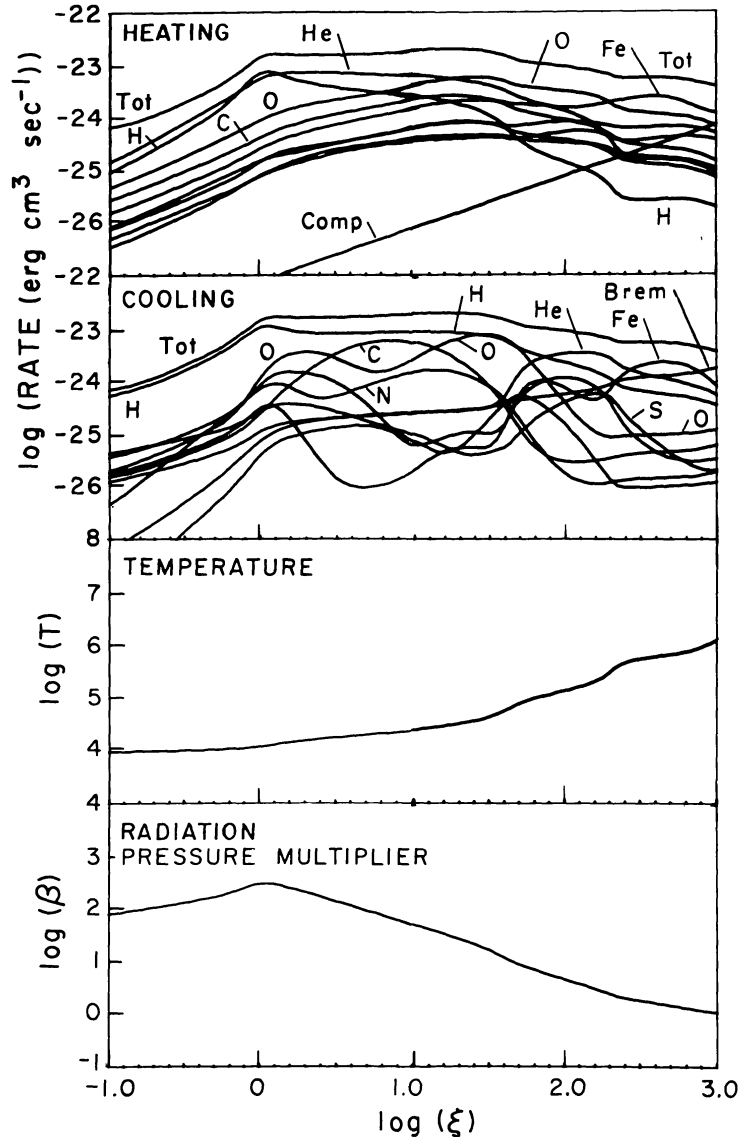


FIG. 4.—Thermal structure of model 2. Heating rates, cooling rates, temperature, and radiation pressure multiplier are shown as a function of $\log \xi$ for $-3 < \log \xi < 5$.

Figure 10*a, b* shows the radiation spectrum from the same model 3 in the neutral hydrogen zone, at $\log \xi = 1.0$. In this region, absorption has removed nearly all radiation from 13.6 eV to ~ 2 keV. In the high energy portion of the spectrum, continuum absorption causes longer wavelength lines to be less luminous than shorter wavelength lines. For example, the luminosity of Si XIV $L\beta$ exceeds that of Si XIV $L\alpha$ by a factor of 2 in Figure 10. The lines carry most of the total energy in the optical and UV radiation field. Of this, the main components are hydrogen Ly α , Ly β , C IV $\lambda 1549$. Other prominent lines are H α and C III $\lambda 977$. The dominant line emission mechanism is recombination, although collisional excitation dominates for a few lines, such as O VI $\lambda 1034$ and C IV $\lambda 1549$. Of special interest are the lines formed by other processes. These include the prominent iron K α fluorescence lines near 6.5 keV and low-lying resonance

lines, such as C II $\lambda 1335$ and O I $\lambda 1135$, which have large contributions from dielectronic recombination. Figure 10*a* also shows strong forbidden line emission from [Fe X] $\lambda 6376$, [S XII] $\lambda 7358$, and [Fe XIII] $\lambda 5438$, all of which have critical densities in the range $\sim 10^{10}$ – 10^{11} cm $^{-3}$. The results shown here differ from the results of model 2 in that the column densities of all emitting and absorbing ions are greater by a factor $\sim 10^4$, resulting in greater continuum optical depths and greater line luminosities.

The parameters of model 3 are the same as those of model 2 of HBM. The results of the two models agree very well overall, but important differences occur in the neutral region as a result of their neglect of charge transfer and secondary collisional ionization of hydrogen. We also differ on details of the emission spectrum, because of our more accurate treatment of line excita-

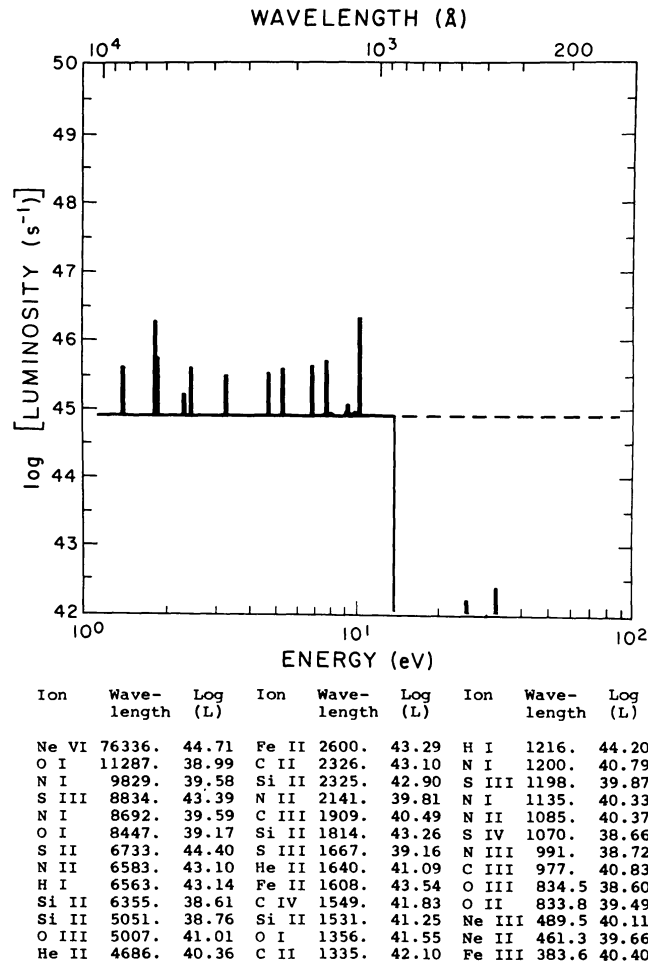


FIG. 5.—Radiation spectrum in model 2 at $\log \xi = -0.10$. Total spectral luminosity (ergs s^{-1}) is shown as a function of photon energy in eV in the low ($1 < \epsilon < 100$ eV) energy range. Photons are sorted into bins of width $\epsilon/\Delta\epsilon = 100$. Wavelengths (Å) and photon luminosities (s^{-1}) of the 100 strongest lines with number luminosities greater than 10^{38} s^{-1} are listed.

tion. For example, we find an emergent luminosity for C IV $\lambda 1549$ which exceeds theirs by a factor of ~ 10 .

d) Model 4: The Effects of Line Trapping

The effects of line trapping change our model results in several important ways. Line trapping impedes the escape of resonance line photons from the cloud, and so impedes the cooling of the gas in the cloud. Trapped resonance lines can also cause the buildup of excited level populations, and so can facilitate ionization from these levels. The radiation spectrum emergent from the cloud is affected by suppression of resonance line luminosities, by the Bowen fluorescence mechanism, and by the splitting of resonance lines. In this section we discuss these processes and present a few simple estimates for escape and destruction probabilities. We then

illustrate the detailed effects of line trapping by presenting the results of a model calculation.

One of the outstanding features of X-ray ionized nebulae is the large column density of ionized material that can occur. As shown in the previous section, the column density increases with the quantity Ln , roughly as the one-half or one-third power. The resonance line optical depths are proportional to the ionized column density, and so may also be very large. The optical depths may be estimated from equation (29), i.e.,

$$\tau \approx \frac{\pi e^2}{mc} f \frac{n_i R}{\Delta v_{D_i}} \approx 2 \times 10^8 X_i \left(\frac{A_i}{T_4} \right)^{1/2} \xi_i^{-1/2} \lambda_A f \left(\frac{Ln}{10^{48} \text{ ergs cm}^{-3} \text{ s}^{-1}} \right)^{1/2}, \quad (32)$$

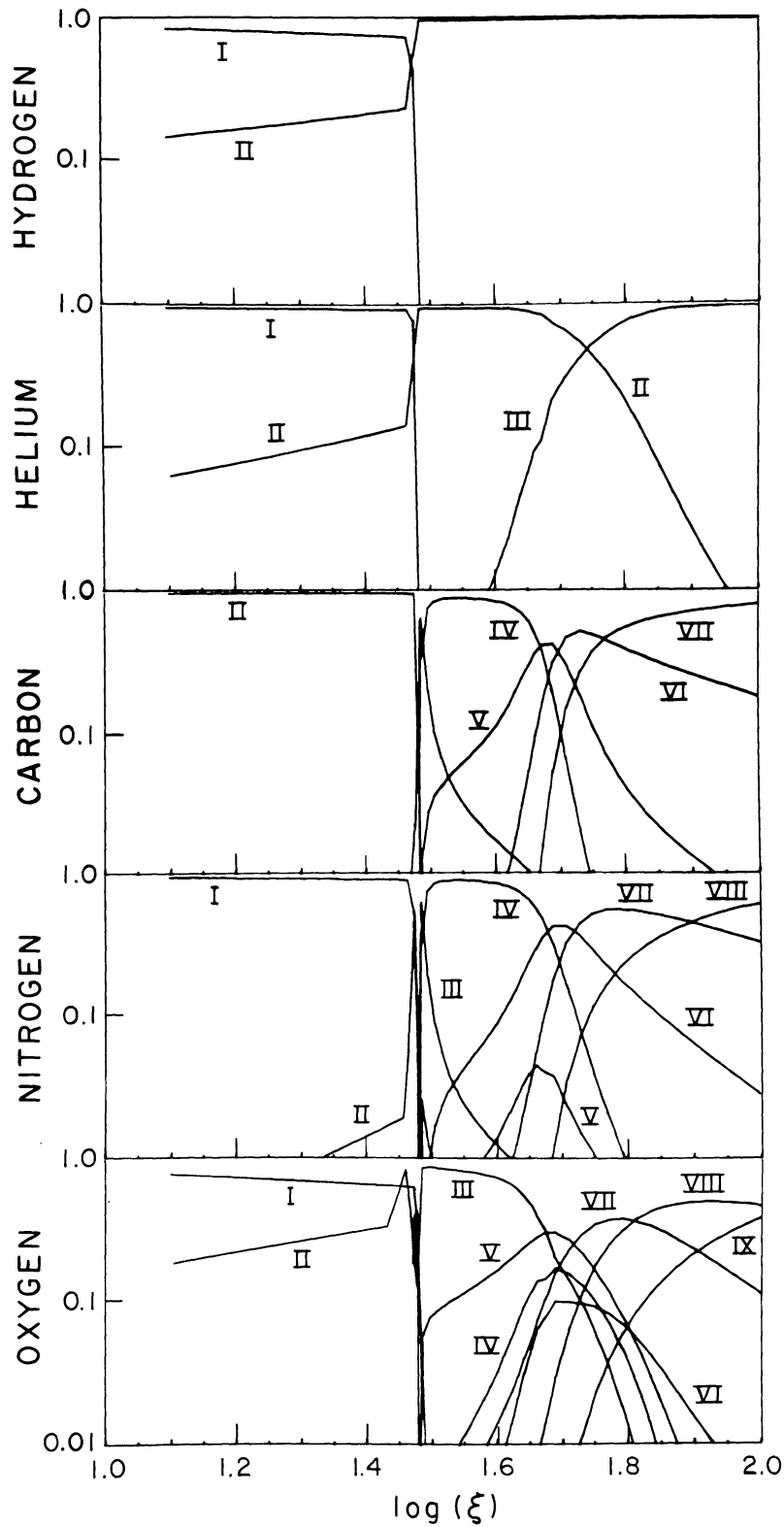


FIG. 6a

FIG. 6.—Ionization structure of model 3 near the hydrogen and helium ionization fronts. Relative abundances of the ions of each element are shown as a function of $\log \xi$ for $1 < \log \xi < 2$. Curves for $\log \xi > 2$ are almost identical to those of Fig. 2a, b.

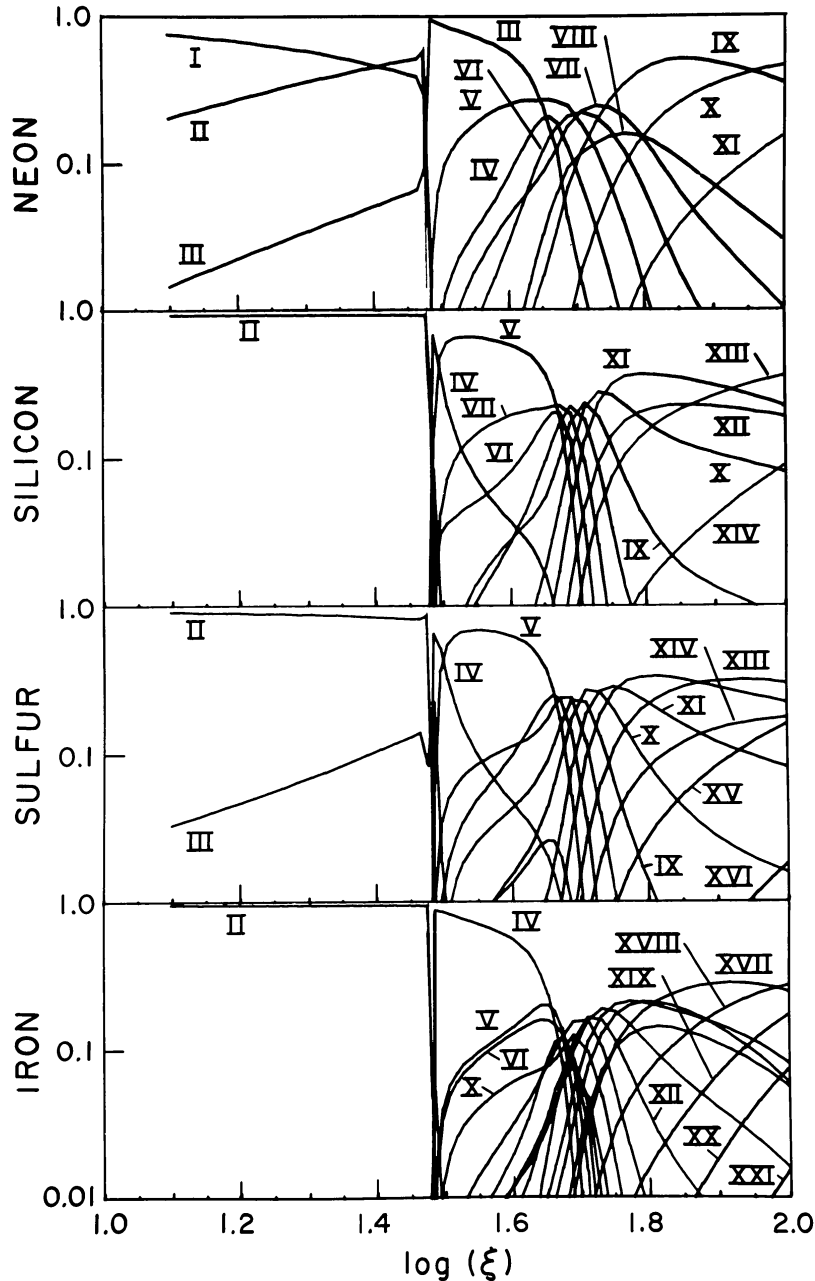


FIG. 6b

where f is the line oscillator strength, X_i is the element abundance, A_i is the atomic weight, T_4 is the gas temperature in units of 10^4 K, and λ_A is the line wavelength in angstroms. Values taken from the results of model 3 give for a few representative lines: $\tau(\text{He II Ly}\alpha) \approx 10^8$; $\tau(\text{O VI } \lambda 1034) \approx 7 \times 10^6$; $\tau(\text{O VIII Ly}\alpha) \approx 2 \times 10^3$; $\tau(\text{O VIII Ly}\beta) \approx 3 \times 10^2$; and $\tau(\text{Fe XXVI Ly}\alpha) \approx 2$.

Resonance line photons created at large optical depths must scatter many times before escaping the nebula, and at each scattering they may be destroyed by one of several processes. Line trapping has the effect of

making resonance lines act as forbidden lines that can be suppressed at high density. The probability of escape per scattering is proportional to $1/\tau$, so that destruction will be important when

$$\tau \approx 1/P_{\text{des}}. \quad (33)$$

Here P_{des} is the probability of destruction per scattering and is the sum of the probabilities for the various destruction processes: collisional de-excitation, continuum absorption, and splitting. Resonance line pho-

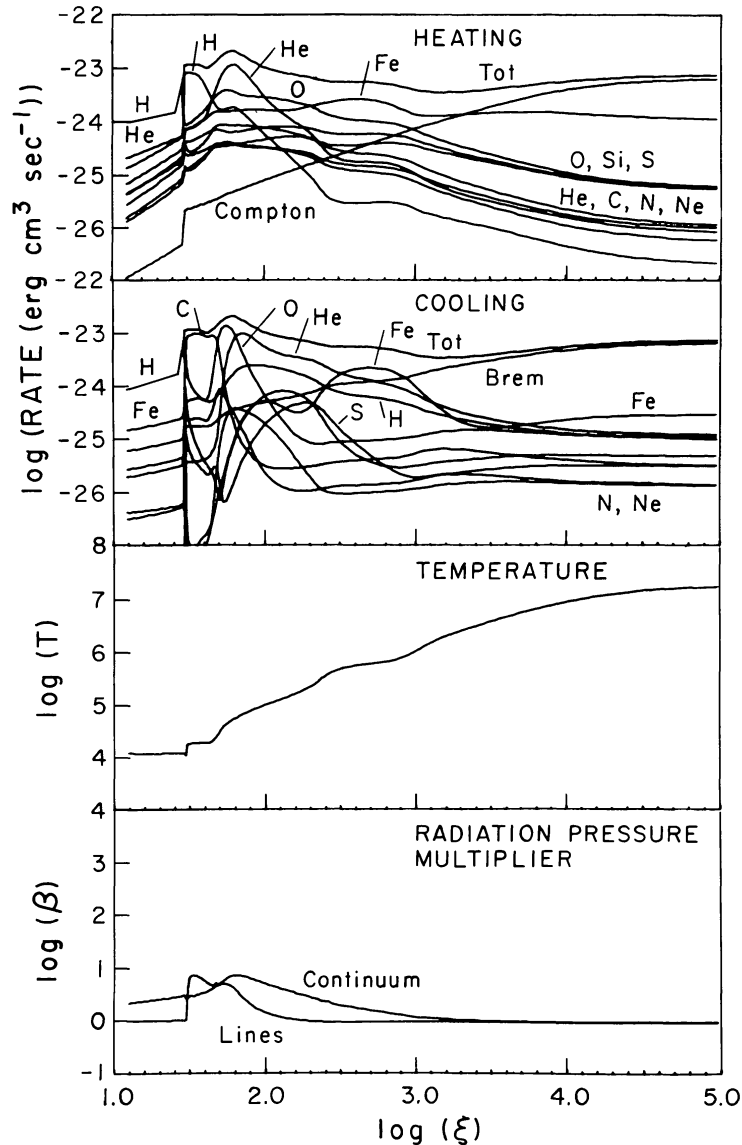


FIG. 7.—Thermal structure of model 3. Heating rates, cooling rates, temperature, and radiation pressure multiplier are shown as a function of $\log \xi$ for $1 < \log \xi < 5$.

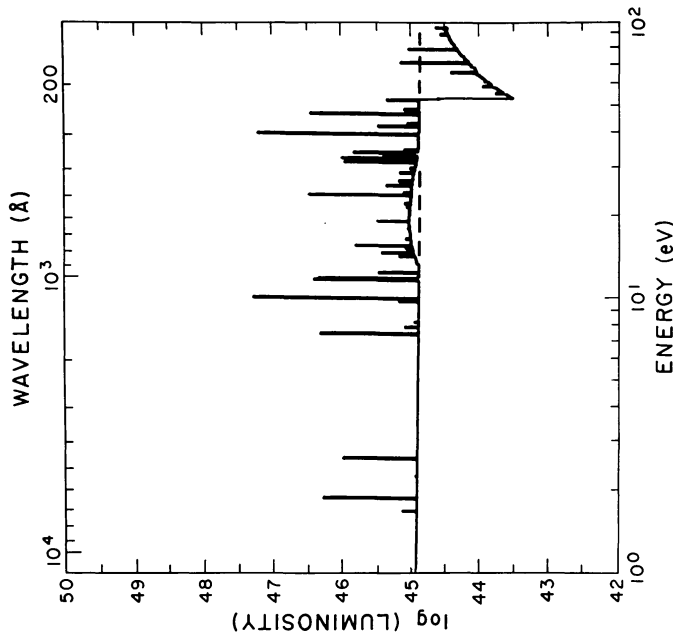
tons not destroyed or modified by these processes will escape the emission region via frequency redistribution or Compton scattering.

The importance of resonance line destruction can be demonstrated by presenting some simple estimates for destruction probabilities. The collisional excitation rate formula of Van Regemorter (1962) may be used to estimate the probability of collisional de-excitation to give

$$P_{th} \approx 4 \times 10^{-27} n_e \lambda_A^3 T_A^{1/2}. \quad (34)$$

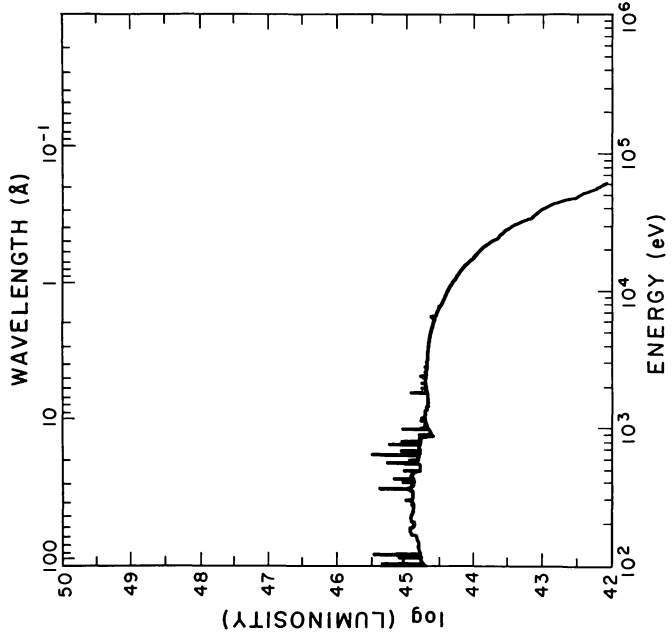
Of the lines mentioned previously, collisional de-excitation will be important in the suppression of O VI $\lambda 1034$

and He II Ly α . For forbidden and intercombination lines, the radiative decay rate is much smaller than for allowed lines, so that collisional de-excitation may be important even for very small optical depths. Continuum photoabsorption is important in regions of the cloud where the continuum opacity is large, which occurs primarily near the hydrogen and He II ionization fronts. However, the strong dependence of the continuum opacity on temperature and position in the cloud makes quantitative estimates of the probability of this process difficult. Both collisional de-excitation and continuum absorption deposit the energy of the destroyed photon as heat in the gas. Thus, these processes will inhibit the cooling of the gas and will result in



| Ion | Wave-length (Å) | Log (L) | Ion | Wave-length (Å) | Log (L) | Ion | Wave-length (Å) | Log (L) |
|----------|-----------------|---------|---------|-----------------|---------|----------|-----------------|---------|
| Si X | 14306. | 41.70 | O IV | 789.4 | 42.33 | Si VIII | 317.7 | 41.15 |
| S XII | 7358. | 42.67 | Ne VIII | 773.7 | 43.74 | C IV | 312.4 | 39.96 |
| H I | 6563. | 44.23 | N IV | 765.1 | 41.57 | He II | 303.9 | 45.22 |
| Fe XIII | 5438. | 41.63 | Fe XIV | 729.8 | 42.19 | Si XI | 303.6 | 43.98 |
| He II | 4686. | 43.91 | Si IX | 666.6 | 41.72 | Fe XV | 284.1 | 43.38 |
| Fe XII | 2406. | 41.00 | O V | 629.7 | 43.31 | Fe XII | 278.6 | 42.57 |
| Si IX | 1888. | 40.81 | He I | 584.3 | 41.38 | N V | 266.3 | 40.17 |
| S IX | 1724. | 40.13 | Ne V | 571.0 | 40.57 | S X | 257.1 | 42.08 |
| He II | 1640. | 44.30 | Ne VI | 561.4 | 42.04 | S XIII | 256.7 | 43.71 |
| Fe II | 1608. | 40.38 | Ne VI | 540.5 | 42.28 | He II | 256.4 | 44.40 |
| C IV | 1549. | 42.62 | He I | 537.0 | 41.03 | O V | 248.5 | 40.46 |
| S IV | 1488. | 40.77 | Fe XIII | 517.0 | 41.01 | N V | 247.7 | 39.89 |
| S XI | 1482. | 42.06 | Si XII | 506.4 | 44.48 | S XI | 247.0 | 42.70 |
| O IV | 1407. | 40.56 | S XII | 497.5 | 42.44 | O IV | 238.5 | 40.22 |
| S X | 1305. | 40.28 | Ne VII | 465.2 | 43.11 | S XII | 227.2 | 43.19 |
| N V | 1240. | 42.84 | Fe XII | 448.4 | 42.74 | Fe XIV | 215.1 | 41.18 |
| O V | 1218. | 42.71 | C IV | 419.7 | 40.37 | Fe XIII | 202.0 | 41.43 |
| He I | 1216. | 45.30 | Fe XV | 418.4 | 42.72 | Fe XII | 195.1 | 40.82 |
| Ne V | 1127. | 39.85 | Fe XII | 401.6 | 42.15 | O VI | 189.1 | 40.59 |
| O VI | 1034. | 44.40 | Fe XIV | 384.4 | 43.94 | C VI | 182.3 | 42.21 |
| H I | 1026. | 44.33 | C IV | 384.1 | 40.09 | Fe XI | 178.6 | 39.74 |
| Ne VI | 1020. | 41.66 | S XIV | 372.1 | 43.98 | O VI | 173.0 | 40.87 |
| N III | 991. | 40.32 | Fe XVI | 360.8 | 43.08 | O V | 172.2 | 40.05 |
| C III | 977. | 40.95 | Fe XIII | 360.1 | 42.76 | Fe XXIII | 168.2 | 42.82 |
| Fe XXIII | 974.7 | 43.33 | Fe XII | 357.2 | 42.02 | Fe XXII | 167.0 | 42.84 |
| Fe XXII | 846. | 42.77 | Fe X | 355.4 | 39.81 | O VI | 150.1 | 40.74 |
| O III | 834.5 | 40.90 | Fe XI | 354.5 | 41.08 | Fe XXI | 150.0 | 42.96 |

FIG. 8a



| Ion | Wave-length (Å) | Log (L) | Ion | Wave-length (Å) | Log (L) | Ion | Wave-length (Å) | Log (L) |
|----------|-----------------|---------|----------|-----------------|---------|----------|-----------------|---------|
| Fe XX | 121.00 | 43.18 | S XIV | 32.50 | 41.40 | Fe XXI | 12.30 | 41.05 |
| Fe XIX | 108.00 | 42.79 | S XIV | 30.43 | 42.51 | Ne X | 12.19 | 42.07 |
| Fe XVIII | 104.00 | 43.30 | N VI | 29.53 | 41.46 | Fe XXII | 11.91 | 40.86 |
| Ne VIII | 103.00 | 43.34 | N VI | 29.08 | 42.00 | Ne IX | 11.56 | 41.55 |
| O VIII | 102.50 | 42.85 | N VI | 28.79 | 40.90 | Fe XXIV | 11.20 | 40.87 |
| Ne VIII | 98.31 | 40.72 | C VI | 28.50 | 42.82 | Fe XXIV | 10.80 | 41.93 |
| Ne VIII | 88.13 | 40.50 | S XVI | 25.54 | 40.95 | Ne X | 10.26 | 41.81 |
| Fe XIV | 77.00 | 40.36 | N VI | 24.90 | 41.26 | Si XIII | 6.74 | 42.01 |
| Fe XVI | 66.30 | 41.13 | O VI | 22.10 | 42.58 | Si XIII | 6.68 | 42.48 |
| Ne X | 65.63 | 41.76 | O VII | 21.80 | 43.06 | Si XIII | 6.65 | 41.34 |
| Fe XVI | 63.50 | 40.30 | O VII | 21.60 | 41.95 | Si XIII | 6.18 | 41.92 |
| Si IX | 55.30 | 40.31 | N VII | 20.94 | 42.28 | Si XIV | 5.68 | 41.85 |
| Si X | 54.90 | 40.27 | O VIII | 19.00 | 43.35 | S XV | 5.22 | 41.55 |
| Fe XVI | 54.70 | 41.00 | O VII | 18.63 | 42.37 | S XV | 5.10 | 41.52 |
| Si X | 50.64 | 40.98 | Fe XIX | 17.86 | 42.70 | S XV | 5.07 | 42.02 |
| Fe XVI | 50.50 | 40.78 | Fe XVII | 16.77 | 40.43 | S XVI | 5.04 | 40.88 |
| Si XI | 49.22 | 40.44 | O VIII | 16.03 | 43.02 | S XVI | 4.73 | 41.31 |
| Si XII | 45.60 | 41.01 | Fe XVIII | 15.80 | 40.73 | S XVI | 4.30 | 41.38 |
| Si XIII | 44.12 | 41.34 | Fe XVII | 15.26 | 42.69 | Fe XVIII | 3.99 | 41.03 |
| C V | 41.47 | 41.46 | Fe XIX | 15.00 | 41.12 | Fe XIX | 1.93 | 40.93 |
| Si XII | 40.92 | 41.66 | Fe XIX | 14.50 | 40.68 | Fe XX | 1.92 | 41.27 |
| Si XII | 40.73 | 42.16 | Fe XVIII | 14.30 | 41.45 | Fe XX | 1.89 | 41.44 |
| C V | 40.27 | 41.07 | Ne VI | 14.10 | 40.94 | Fe XXI | 1.89 | 41.41 |
| C V | 40.27 | 41.07 | Ne VI | 14.10 | 40.94 | Fe XXI | 1.89 | 41.41 |
| S XI | 39.80 | 40.39 | Ne IX | 13.70 | 42.19 | Fe XXIII | 1.87 | 41.02 |
| S XII | 37.80 | 40.39 | Ne IX | 13.70 | 42.19 | Fe XXV | 1.87 | 41.02 |
| S XIII | 36.50 | 41.08 | Fe XX | 13.70 | 40.74 | Fe XXV | 1.86 | 41.49 |
| S XIII | 35.70 | 40.38 | Fe XX | 13.50 | 41.32 | Fe XXV | 1.85 | 40.37 |
| C V | 34.97 | 41.43 | Ne IX | 13.46 | 41.06 | Fe XXVI | 1.79 | 40.28 |
| C VI | 33.78 | 43.16 | Fe XX | 13.40 | 41.46 | Fe XXV | 1.57 | 40.82 |

FIG. 8b

FIG. 8.—Radiation spectrum of model 3 at $\log \xi = 1.8$, near the He II ionization front

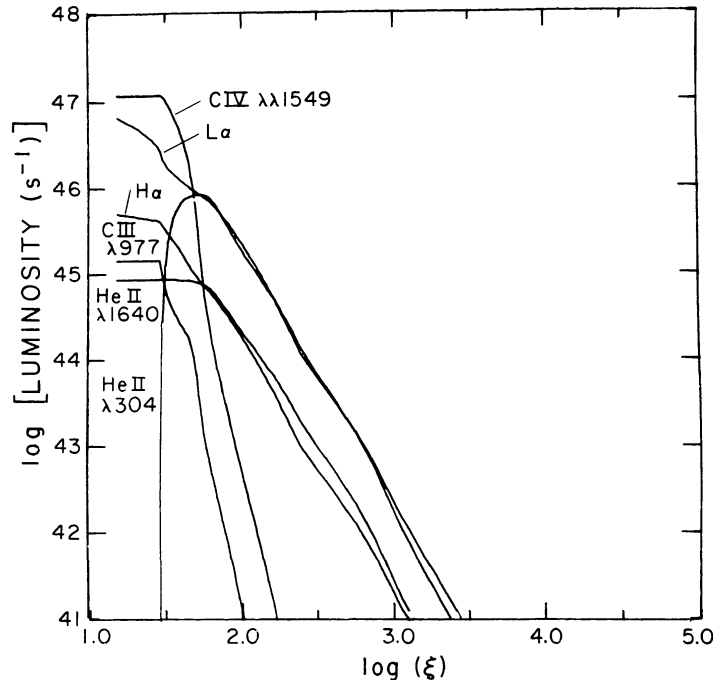


FIG. 9.—Luminosities of selected lines from model 3. Line luminosities are shown as a function of $\log \xi$ for $1 < \log \xi < 5$.

higher temperatures in regions where the cooling is dominated by line excitation.

The effect of resonance line splitting is to break photons into longer wavelength pieces rather than to destroy them. When an intermediate energy level exists, the splitting probability per scattering is typically 0.01–0.4, so that this process can dominate collisional de-excitation and continuum absorption. The primary effect of splitting is to increase the luminosities of subordinate lines relative to resonance lines, leading to spectra of the type referred to as case B (see, e.g., Davidson and Netzer 1979). Thus, the luminosities of splittable resonance lines can be used as an optical depth diagnostic, when both the resonance line and the subordinate it produces can be observed. For example, the ratio of $\text{Ly}\beta$ to $\text{H}\alpha$ luminosities of hydrogenic ions, which is ~ 1.3 in the optically thin limit, will decrease to zero when the $\text{Ly}\beta$ optical depth is large. Splitting could also facilitate the cooling of the cloud by moving line radiation to longer wavelengths where the continuum opacity may be smaller. However, in our models the cooling is never dominated by excitation of such lines, so the net effect of line trapping is to suppress line cooling.

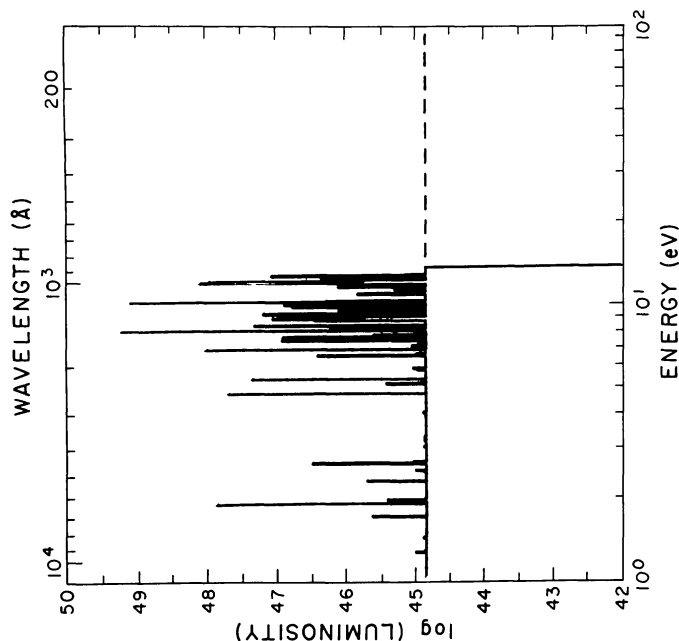
In addition to modifying the cooling of the gas, resonance line trapping affects the ionization structure of our models, via the buildup of the $n = 2$ populations of H I and He II. The excited level populations can be estimated by solving the statistical equilibrium equations for a two-level atom. If the effective decay rate for the upper level is $A_{21}F_{\text{esc}}$, where F_{esc} is the $\text{Ly}\alpha$ line

escape fraction, then the ratio of excited level population to ground level population is

$$n_2/n_1 \approx (n_2/n_1)^*/(1 + n_{\text{crit}}F_{\text{esc}}/n_e), \quad (35)$$

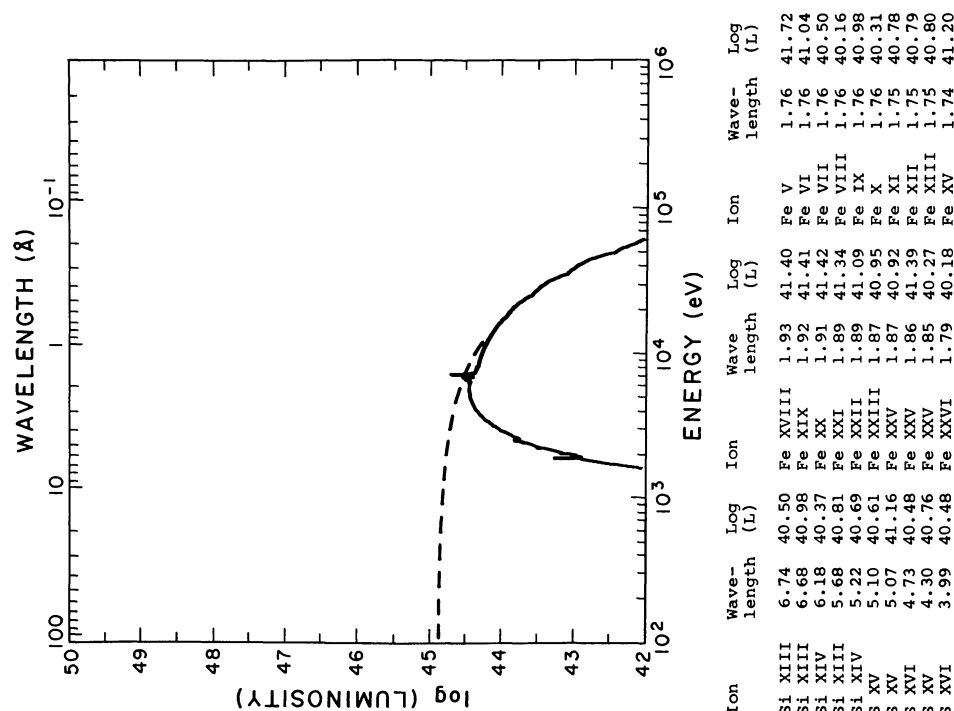
where $(n_2/n_1)^*$ is the population ratio in local thermodynamic equilibrium (LTE) and is given by the Boltzmann factor. For hydrogen, $n_{\text{crit}} \approx 8 \times 10^{16} \text{ cm}^{-3}$, so that $n_2/n_1 \approx (n_2/n_1)^*$ for $F_{\text{esc}} < 10^{-6}$. For He II, $n_{\text{crit}} \approx 6 \times 10^{18} \text{ cm}^{-3}$, so $n_2/n_1 \approx (n_2/n_1)^*$ for $F_{\text{esc}} \leq 10^{-8}$. A significant population of hydrogen atoms in $n = 2$ is, in effect, a new abundant trace ion with a low-lying excitation and ionization potential. The excited atoms can contribute significant cooling through collisional ionization and collisional excitation of $\text{H}\alpha$, which acts as a resonance line, and significant heating through photoionization. At larger optical depths, the populations of the $n = 3$ and higher levels become significant. We have neglected this effect, which must be included in more accurate calculations of this type (e.g., Krolik and McKee 1978).

The $\text{Ly}\alpha$ line of He II deserves special mention. We have already shown that the optical depth in this line may be large enough for the $n = 2$ level population to build up and for collisional de-excitation to occur. However, photons in the He II $\text{Ly}\alpha$ line may also be removed by the Bowen resonance fluorescence mechanism. As shown by Kallman and McCray (1980), when the fractional abundance of He II and O III are comparable, the efficiency of Bowen conversion from He II $\text{Ly}\alpha$ to the O III Bowen lines will approach 100% for He II $\text{Ly}\alpha$



| Ion | Wave-length | Log (L) | Ion | Wave-length | Log (L) |
|--------|-------------|---------|---------|-------------|---------|
| Si X | 14306. | 42.56 | Si IV | 3160. | 41.41 |
| O I | 11287. | 40.92 | O IV | 3066. | 41.93 |
| S VIII | 9872. | 42.18 | C II | 2837. | 41.26 |
| N I | 9829. | 40.79 | Fe II | 2600. | 45.29 |
| S III | 8834. | 41.47 | Fe XII | 2406. | 43.17 |
| N I | 8692. | 40.83 | Ne IV | 2362. | 41.14 |
| O I | 8447. | 41.16 | C II | 2325. | 43.12 |
| S XII | 7358. | 43.13 | Si II | 2325. | 44.96 |
| C II | 7234. | 40.92 | C III | 2296. | 41.19 |
| C II | 6580. | 41.26 | Ne V | 2269. | 40.94 |
| H I | 6563. | 45.71 | N II | 2141. | 42.09 |
| Fe X | 6376. | 43.05 | Si VII | 2128. | 42.58 |
| Si II | 6355. | 41.19 | Ne VI | 2047. | 40.68 |
| Fe XII | 5438. | 43.40 | S VI | 1987. | 40.76 |
| Fe XIV | 5304. | 43.70 | C III | 1909. | 44.37 |
| Si II | 5051. | 41.34 | Si III | 1895. | 43.83 |
| O III | 5007. | 41.89 | Si IX | 1888. | 42.30 |
| He II | 4886. | 44.52 | Si II | 1814. | 45.25 |
| O II | 4852. | 42.38 | N III | 1750. | 42.72 |
| N III | 4641. | 40.71 | S IX | 1724. | 42.23 |
| N III | 4623. | 40.88 | Si IV | 1724. | 41.04 |
| Si IV | 4099. | 41.68 | S III | 1667. | 42.38 |
| O II | 4098. | 40.62 | O III | 1663. | 44.92 |
| Ne III | 3903. | 41.25 | He II | 1640. | 44.94 |
| Si II | 3870. | 41.37 | Fe II | 1608. | 42.95 |
| Si II | 3858. | 40.80 | C IV | 1549. | 47.08 |
| O VI | 3819. | 40.58 | Si II | 1531. | 43.82 |
| O III | 3762. | 41.69 | Si VIII | 1489. | 40.94 |

FIG. 10a



| Ion | Wave-length | Log (L) | Ion | Wave-length | Log (L) |
|---------|-------------|---------|----------|-------------|---------|
| Si XIII | 6.74 | 40.50 | Fe XVIII | 1.93 | 41.40 |
| Si XIII | 6.68 | 40.98 | Fe XIX | 1.92 | 41.41 |
| Si XIV | 6.18 | 40.37 | Fe XX | 1.91 | 41.42 |
| Si XIII | 5.68 | 40.81 | Fe XXI | 1.89 | 41.34 |
| Si XIV | 5.22 | 40.69 | Fe XXII | 1.89 | 41.09 |
| S XV | 5.10 | 40.61 | Fe XXIII | 1.87 | 40.95 |
| S XV | 5.07 | 41.16 | Fe XXV | 1.86 | 40.92 |
| S XVI | 4.73 | 40.48 | Fe XXV | 1.85 | 40.27 |
| S XVI | 3.99 | 40.48 | Fe XXVI | 1.79 | 40.18 |

FIG. 10b

FIG. 10.—Radiation spectrum from model 3 at $\log \xi = 1.0$

optical depths greater than 10^4 and neutral hydrogen abundances less than 500 $n(\text{O III})$. Thus, the Bowen mechanism can effectively control the $\text{He II } n=2$ level population.

We now present the results of a model calculation which illustrates many of the effects discussed so far. Model 4 has the same model parameters as model 3, but includes line trapping as described in §§ IV and V. Thus, model 4 is applicable to a compact X-ray source in a gas cloud, perhaps from a stellar wind or an accretion flow, provided that velocity gradients are negligible compared with the thermal velocity dispersion in the gas.

The dominant effect of line trapping in model 4 is the suppression of line cooling. This is apparent in the thermal structure of model 4, shown in Figure 11. For $\log \xi > 3.0$, the thermal balance in the gas is identical to model 3. At smaller values of $\log \xi$, the cooling is reduced from that of model 3 typically by a factor of 2. The effects are most pronounced near $\log \xi = 1.55$, where collisional de-excitation suppresses the dominant coolant, $\text{C IV } \lambda 1549$, and continuum absorption reduces the cooling due to other resonance lines, such as $\text{N IV } \lambda 765$ and $\text{Ne III } \lambda 251$. The photoionization heating of the gas in this region is weakly dependent on the effects of line trapping, so that the suppression of cooling in model 4 causes the temperature to exceed that of model 3 by a factor of 2–3, for $1.5 < \log \xi < 3.0$. For $\log \xi < 1.5$, the hydrogen line cooling is suppressed by trapping of $\text{Ly}\alpha$ and $\text{H}\alpha$. The cooling in this region is dominated by collisional ionization of hydrogen, and the temperature approaches 1.6×10^4 K, rather than 1.2×10^4 K as in model 3.

The effects of resonance line trapping on the ionization structure of model 4 are apparent in Figure 12*a, b*, which shows the relative ion abundances as a function of $\log \xi$. Comparison of these results with model 3 (Fig. 6*a, b*) shows that model 4 is slightly more ionized throughout the cloud. This is due to the fact that the recombination rates are smaller at the higher temperatures found in model 4. More important is the effect of ionization from the excited levels of hydrogenic ions, which significantly changes the structure of the cloud in the vicinity of the He II and He I ionization fronts. Photoionization from the $n=2$ level of He II moves the ionization front from $\log \xi \approx 1.75$ in model 3 to $\log \xi \approx 1.65$ in model 4. Photoionization from the $n=2$ level of H I moves the He I ionization front from $\log \xi \approx 1.5$ in model 3 to $\log \xi \approx 1.3$ in model 4 and suppresses the recombination of hydrogen.

Line trapping dramatically affects the radiation spectrum emergent from model 4. Figure 13 shows the luminosities of some selected lines in model 4 as functions of $\log \xi$, and Figure 14*a, b* shows the radiation spectrum at $\log \xi = 1.0$. The effect of resonance line suppression is apparent in Figure 13, which shows that

the luminosities in hydrogen $\text{Ly}\alpha$ and $\text{He II Ly}\alpha$ are much smaller than in model 3 (Fig. 9) throughout the cloud. At the same time, the luminosities of the $\text{H}\alpha$ lines of hydrogen and He II are enhanced, due primarily to recombination following ionization from the $n=2$ levels of these ions. Resonance line trapping also greatly suppresses the luminosities of $\text{Ly}\beta$ lines of hydrogenic ions by splitting them into $\text{Ly}\alpha$ plus $\text{H}\alpha$ lines. For example, the $\text{Si XIV Ly}\beta$ line at 5.22 \AA is suppressed by a factor $\geq 10^2$ in model 4 compared to model 3. Comparison of the spectra from models 3 and 4 (Figs. 10, 14) shows that, although line trapping suppresses the luminosities of the brightest resonance lines, the spectrum from model 4 shows a much richer variety of lower luminosity lines. In addition, Figure 14*a* shows prominent Balmer continuum emission, due to recombination following collisional ionization from the $n=2$ level. At $\log \xi \approx 1$, model 4 has equal amounts of energy in the continuum and line spectra, with 20% of the energy carried by the $\text{H}\alpha$ line. In this region, the hydrogen line ratios approach values appropriate to a Planck spectrum at the local gas temperature.

Although most resonance line luminosities are suppressed in model 4, interesting exceptions occur for collisionally excited resonance lines which dominate the cooling in some region of the cloud, for example, $\text{C IV } \lambda 1549$ and $\text{O VI } \lambda 1034$. The suppression of escape of these lines forces the temperature and the line emissivity in the emitting region to increase sufficiently that the total line luminosity will remain roughly the same in models 3 and 4. The elevated temperature of model 4 is reflected in the greater ratio of $\text{O VI } \lambda 1034 / \text{C IV } \lambda 1549$. Hydrogen Balmer continuum absorption causes a decrease in the luminosities of all UV lines for $\log \xi < 1.3$.

The importance of the Bowen mechanism in model 4 is apparent in Figure 13. For $\log > 1.6$, Bowen conversion is inefficient, and the $\text{He II Ly}\alpha$ line luminosity builds up with decreasing ξ . In this region, the $n=2$ level population of He II approaches about half the LTE value, and photoionization from this level dominates the He II ionization, but for $\log \xi \leq 1.7$, O IV recombines to O III , the efficiency of the Bowen mechanism rapidly increases to 90%, and the luminosity in the O III Bowen lines (e.g., $\lambda 3762$) begins to build up. At this point, $\text{He II Ly}\alpha$ is no longer effectively trapped, so the $n=2$ level population is insignificant. At $\log \xi \approx 1.6$, N IV recombines to N III , and the O III to N III Bowen conversion becomes efficient, producing $\text{N III } \lambda 4641$. The luminosities in both the O III and the N III Bowen lines level off at $\log \xi \approx 1.5$, where helium becomes neutral.

When line trapping is important, the temperature and ionization structure of the outermost part of a model may depend on the location of the outer boundary, which determines the optical depth and escape probabilities of the resonance lines emitted by the ions found there. Therefore, the strengths of emission lines, such as

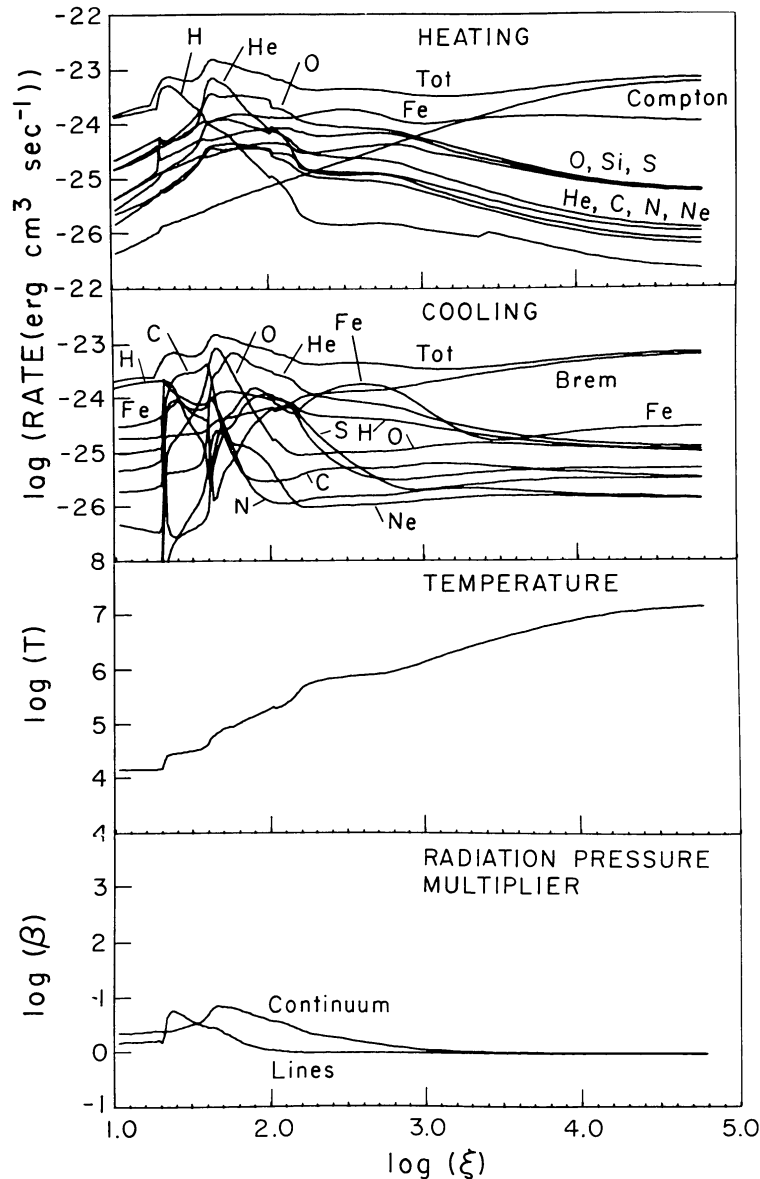


FIG. 11.—Thermal structure of model 4

$\text{Ly}\alpha$ and $\text{H}\alpha$, from the dominant ions at the outer boundary of the model (usually the lowest ionization stage) depend on this arbitrary location. However, the strengths of emission lines from higher ionization stages are almost independent of the location of the outer boundary.

e) Model 5: The Effects of a Stellar Radiation Field

We now consider the effects of varying the source spectrum in our models, beginning with model 5, which has a stellar radiation field added to the X-ray source spectrum. The stellar radiation field is a blackbody spectrum with radiation temperature 30,000 K and luminosity $L_* = 2.7 \times 10^{37} \text{ ergs s}^{-1}$ and is diluted and

transferred in the same way as the X-ray spectrum. The computational procedure and the rest of the parameters of the model—gas density, X-ray source luminosity, and spectrum—are the same as in model 4. Thus, model 5 corresponds roughly to a compact X-ray source near an early-type star, with the surrounding gas coming from the stellar wind. However, our assumed stellar spectrum will not accurately reproduce the ionization observed in the winds of early-type stars, and we have not correctly accounted for the velocity gradients and density variations that would occur in a real stellar wind.

The main effect of the stellar radiation field is to prevent the formation of ions with thresholds below $\sim 50 \text{ eV}$. In the region of the cloud where the dominant

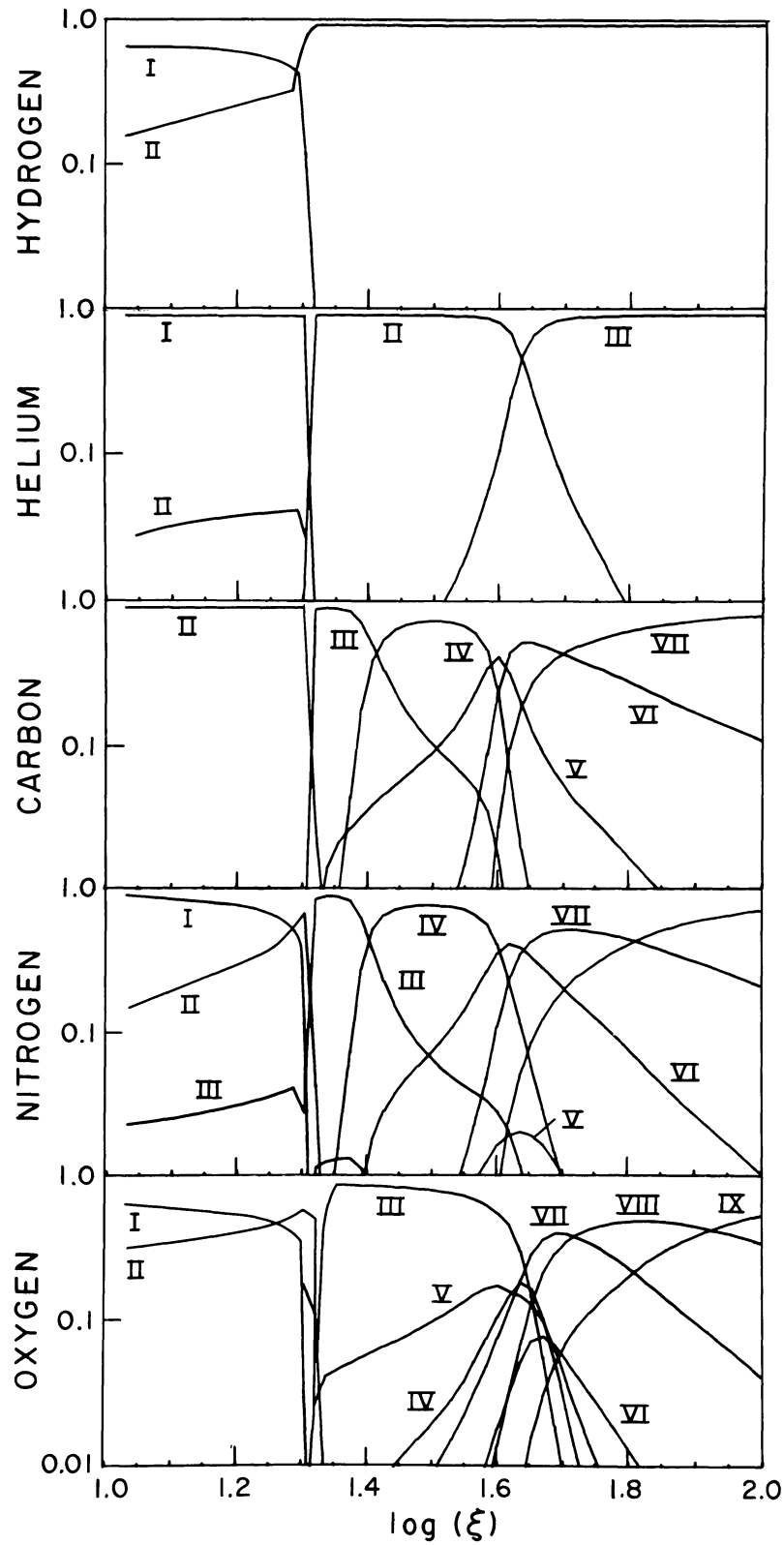


FIG. 12a

FIG. 12.—Ionization structure of model 4 for $1.0 < \log \xi < 2.0$ near the hydrogen and helium ionization fronts

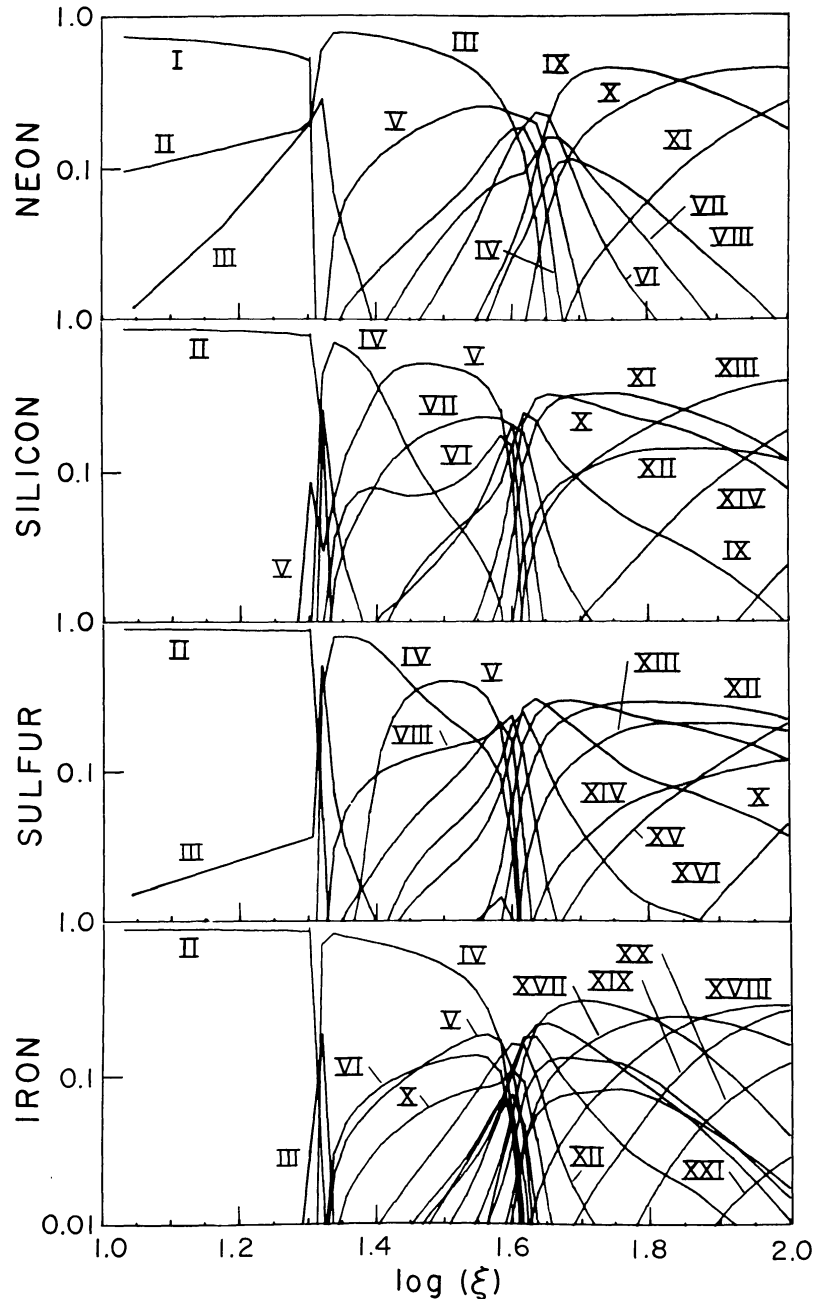


FIG. 12b

ions have thresholds greater than this value, the model results are similar to model 4. This is illustrated in Figure 15*a, b*, which shows the ionization structure of model 5 as a function of $\log \xi = 26 - 2 \log [R(\text{cm})]$. For $\log \xi > 1.8$, the ionization structure is essentially unaffected by the stellar radiation field. For $\log \xi < 1.8$, comparison with the results of model 4 shows that the addition of the stellar radiation field moves the He I ionization front from $\log \xi \approx 1.7$ to $\log \xi \approx 1.5$ and removes the H I ionization front. In the zone beyond the He II ionization front, $\log \xi < 1.5$, the ionization of trace

elements changes, due to the steep decrease in stellar flux for photon energies greater than ~ 20 eV. In this zone, carbon recombines from C IV to C III, and nitrogen recombines from N IV to N III.

Figure 16 shows the temperature structure of model 5 in the range $1.0 < \log \xi < 5.0$. These results differ from model 4 as a result of the differing spectral shapes of the two models. The addition of the large flux of stellar photons at low energies greatly increases the cooling of the gas by inverse Compton scattering, causing the temperature in model 5 near the source to be a factor of

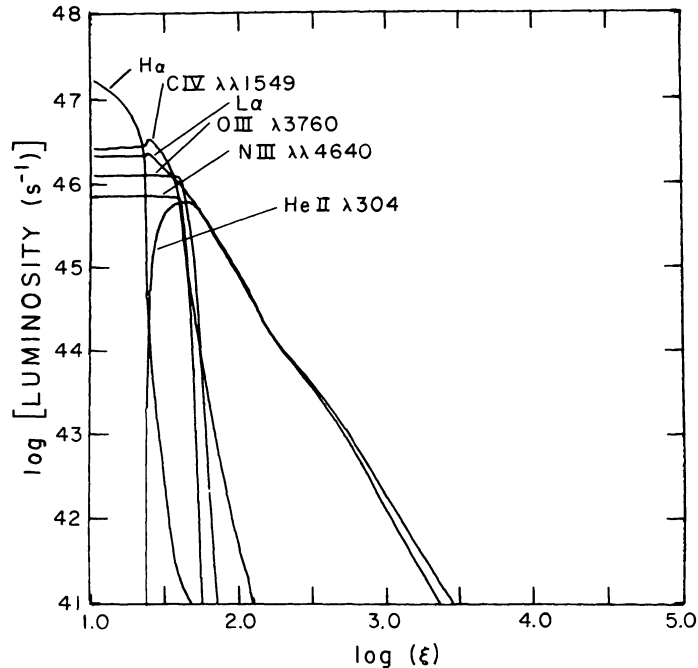


FIG. 13.—Luminosities of selected lines from model 4 as functions of $\log \xi$ for $1 < \log \xi < 5$

2.5 lower than in model 4. Further from the source, for $1.8 < \log \xi < 3.0$, the thermal structures of models 4 and 5 are nearly identical. In the He II zone, for $\log \xi < 1.5$, the gas is nearly isothermal, as a result of C IV $\lambda 1549$, hydrogen Ly α , and Si IV $\lambda 1398$ collisional excitation cooling.

The radiation spectrum escaping from model 5 is shown in Figure 17*a, b* for $\log \xi = 1.0$. Since the stellar radiation field keeps hydrogen and helium at least singly ionized throughout the cloud, the optical depths in the hydrogen and He I continua are small. Figure 17*a* shows absorption edges due to hydrogen, He I, and He II, in addition to prominent EUV emission lines such as He II Ly α , O III $\lambda 374$, Fe XIV $\lambda 384$, and Si XII $\lambda 506$. For wavelengths greater than 912 Å, comparison with the results of model 4 shows that the stellar radiation field suppresses the luminosities of lines of neutral and singly ionized ions such as hydrogen, Si II, and C II, while enhancing the luminosities of lines of doubly ionized species such as C III, N III, and Si III. These line luminosities will be roughly proportional to the stellar luminosity. A decrease in stellar temperature will cause the stellar radiation field to be reprocessed into lines from less ionized species, such as Si II and C II.

f) Model 6: Soft X-Ray Source

Model 6 illustrates the effect of lowering the X-ray source temperature in our models. It has a source with a 2 keV bremsstrahlung spectrum and is otherwise the same as model 4. Model 6 may be applicable to a compact source of soft X-rays, such as may occur in a burster or a galactic bulge source (Lewin and Joss 1981).

The ionization and temperature structure of model 6 are shown in Figures 18*a, b* and 19, respectively. Model 6 differs from model 4 in two ways. First, due to the shortage of high energy photons, model 6 is cooler and less ionized than model 4 in the region near the source. For $\log \xi \leq 5.0$, model 6 has a gas temperature $T \approx 4 \times 10^6$ K, and iron is predominantly hydrogenic and helium-like. This contrasts with model 4, which has $T \approx 2 \times 10^7$ K and iron fully stripped at the same values of $\log \xi$. The second difference between the two models is that, since the total luminosity is the same in both cases, the normalized spectral function, f_e , is a factor of 5 larger in model 6 than in model 4 for energies below 1 keV. As a result, the ionized region of model 6 is larger. The He II ionization front occurs at $\log \xi \approx 1.3$, and the hydrogen front at $\log \xi \approx 1.1$. Because of the similarity in spectral shape of models 4 and 6, the shapes of the ion abundance curves and temperature curves are very similar in the two models.

The radiation spectrum emergent from model 6 is shown in Figure 20*a, b*. This spectrum differs from the spectrum emergent from model 4 primarily in that (i) the lower column densities of neutral matter result in lower line luminosities from neutral and nearly neutral ions, i.e., H I, C II, N I, O I, Si II, S II, and Fe II; and (ii) the shortage of high energy photons causes the Fe $\lambda 1.76$ K α fluorescence lines to be very weak.

g) Model 7: Power-Law Spectrum

Model 7 illustrates the effects of a power-law spectrum of X-rays. The source spectrum in this model varies as ϵ^{-1} , and the source luminosity and gas density

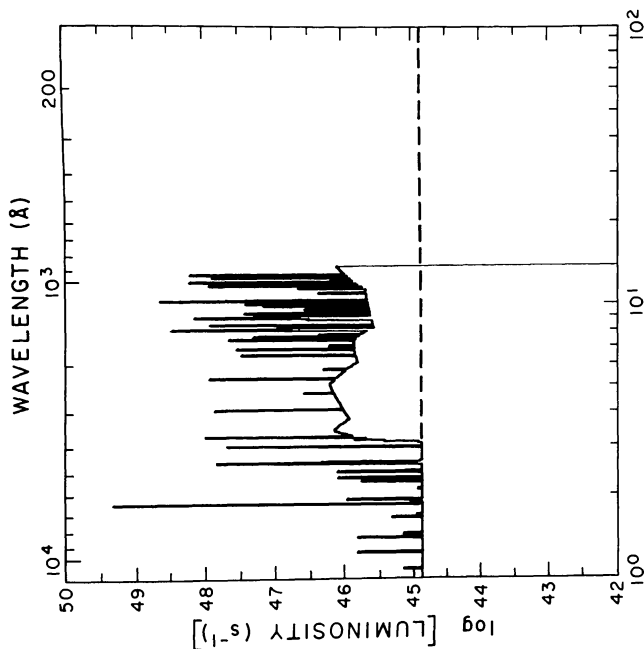


FIG. 14a

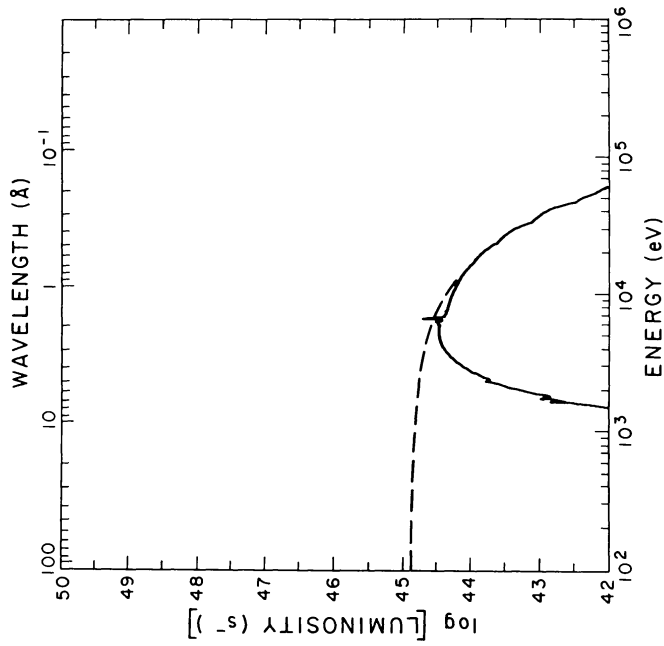


FIG. 14b

FIG. 14.—Radiation spectrum from model 4 at $\log \xi = 1.0$

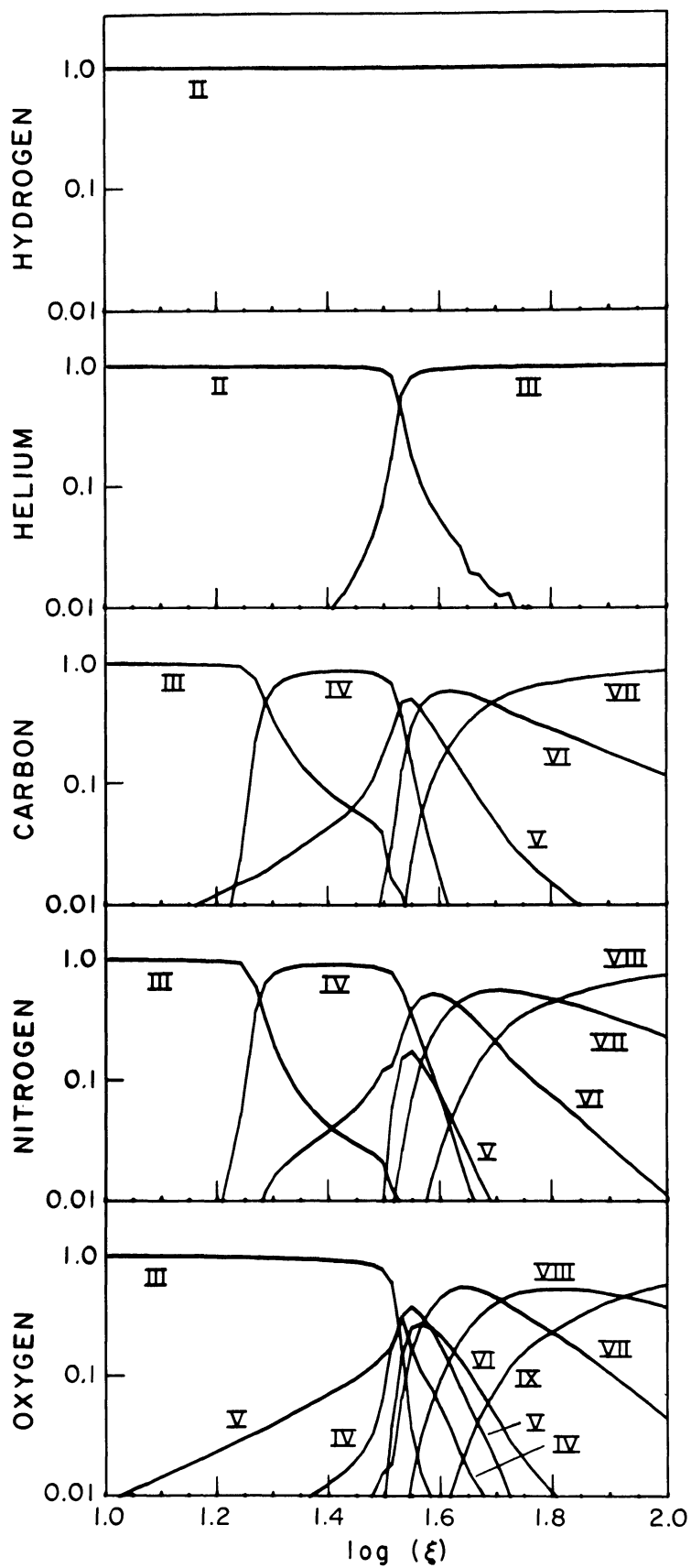


FIG. 15a

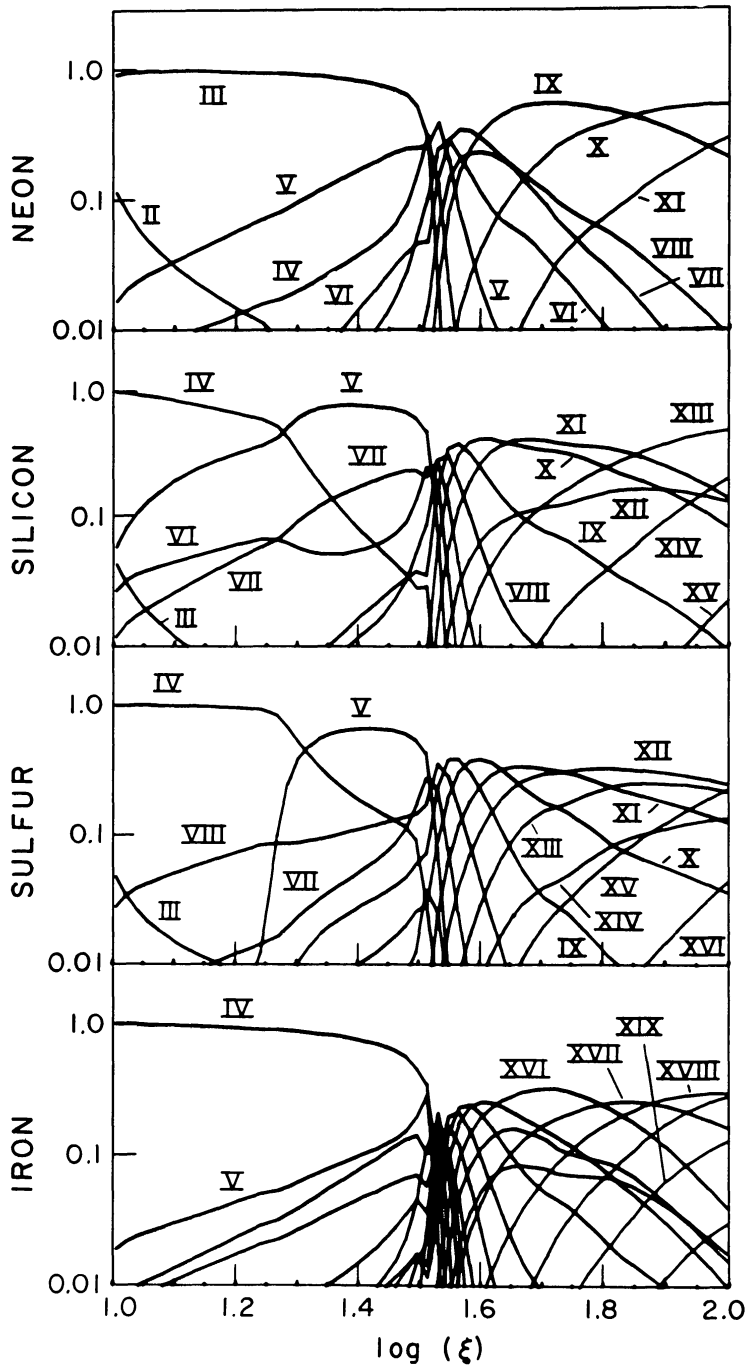


FIG. 15b

FIG. 15.—Ionization structure of model 5 for $1 < \log \xi < 2$

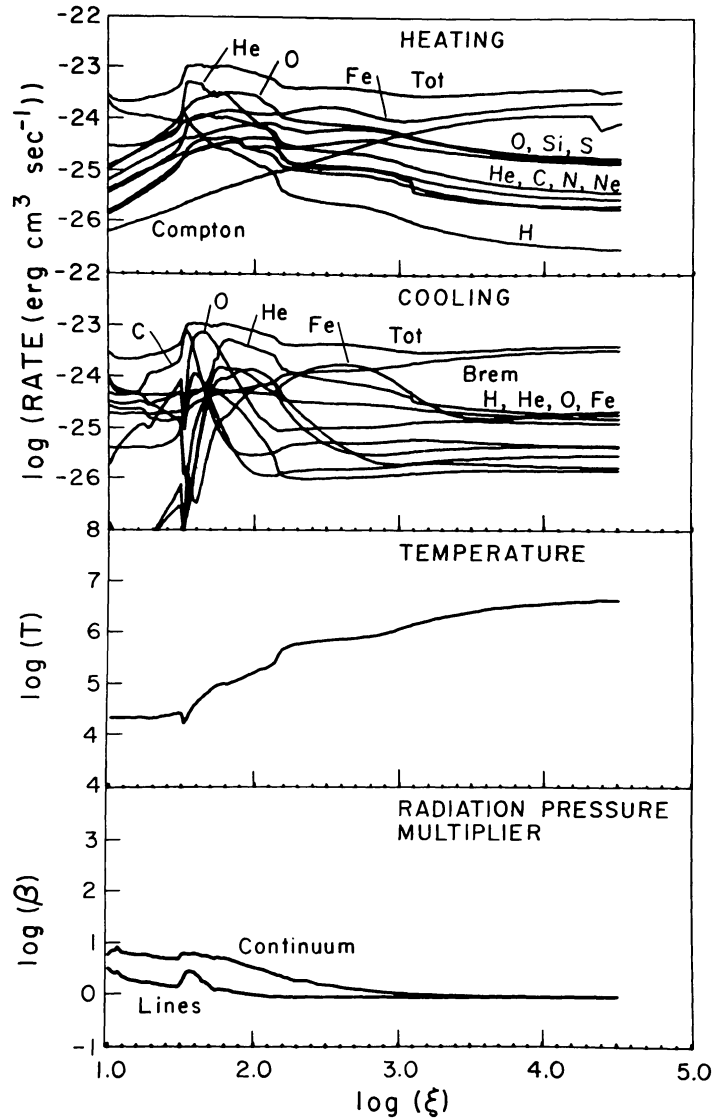


FIG. 16.—Thermal structure of model 5

are the same as model 4. Power-law spectra of this type are observed from some galactic X-ray sources such as Cyg X-1 (Sunyaev and Trümper 1979), and from extragalactic sources such as active galactic nuclei (Davidson and Netzer 1979).

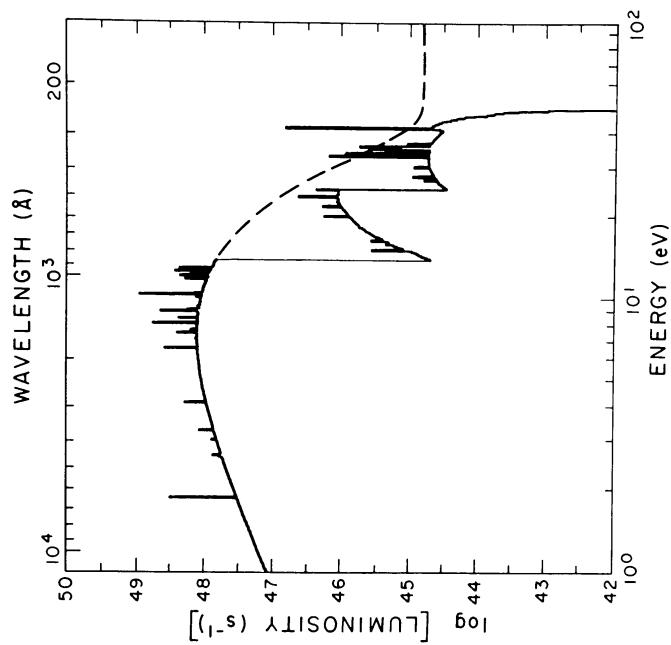
The power-law spectrum has approximately the same total flux at energies beyond the iron K edge as does the 10 keV bremsstrahlung spectrum of model 4. As a result, the ionization structure of model 7 is similar to that of model 4 in the region $3 \leq \log \xi \leq 5$. The ionization and temperature structures of model 7 are shown in Figures 21*a, b* and 22, respectively. At photon energies below a few keV, the power-law spectrum has a far greater flux than the bremsstrahlung spectrum, so the structure of model 7 in the region $\log \xi < 3.0$ resembles the soft

X-ray model 6 more than model 4. For example, the He II ionization front in model 7 occurs at $\log \xi \approx 1.4$, and the hydrogen ionization front is at $\log \xi \approx 1.2$.

The spectrum emergent from model 7 is shown in Figure 23*a, b*. Comparison with the results of model 4 shows that the UV and optical lines formed in the hot, ionized zone are more luminous in this case.

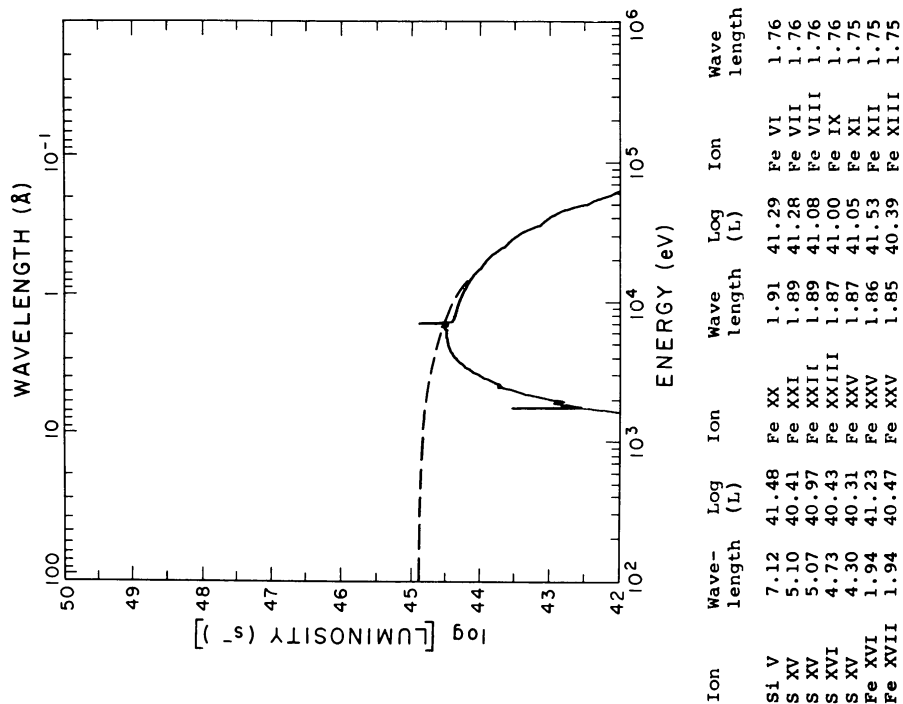
h) Model 8: Blackbody Model

Our models display qualitatively different behavior when the X-ray source spectrum is deficient in soft photons. In this case, strong collisionally excited line cooling can cause the gas to be thermally unstable (Buff and McCray 1974*a*). We illustrate this effect with model



| Ion | Wave-length (L) | Log (L) | Ion | Wave-length (L) | Log (L) | Ion | Wave-length (L) | Log (L) |
|--------|-----------------|---------|--------|-----------------|---------|--------|-----------------|---------|
| Si X | 14306. | 42.67 | Si II | 1814. | 43.69 | S VI | 937.1 | 43.71 |
| S XII | 7358. | 43.12 | N III | 1750. | 44.86 | O III | 834.5 | 43.43 |
| C II | 7234. | 43.32 | S IX | 1724. | 42.09 | O II | 833.8 | 42.22 |
| C II | 6580. | 43.22 | S III | 1667. | 43.38 | O IV | 789.4 | 42.63 |
| H I | 6563. | 46.50 | O III | 1663. | 46.13 | N IV | 765.1 | 43.19 |
| Fe X | 6376. | 42.43 | He II | 1640. | 45.54 | N III | 691.4 | 42.64 |
| C IV | 5805. | 41.98 | Fe II | 1608. | 43.17 | S III | 683.1 | 42.04 |
| Fe XII | 5438. | 43.58 | C IV | 1549. | 46.70 | O V | 629.7 | 44.07 |
| Fe XIV | 5304. | 44.04 | Si II | 1531. | 42.13 | He I | 584.3 | 44.00 |
| O III | 5007. | 42.92 | N IV | 1488. | 46.10 | Ne V | 571.0 | 41.95 |
| He II | 4886. | 44.75 | S XI | 1482. | 42.97 | Ne VI | 561.4 | 42.84 |
| O II | 4852. | 43.69 | O IV | 1407. | 44.70 | S XI | 540.5 | 42.37 |
| N III | 4641. | 45.34 | Si IV | 1397. | 46.56 | O II | 539.4 | 42.05 |
| N III | 4623. | 42.79 | S IV | 1385. | 45.78 | He I | 537.0 | 44.55 |
| N III | 4489. | 45.10 | C XI | 1343. | 42.28 | Fe XII | 533.7 | 42.58 |
| O II | 4099. | 42.33 | Fe XI | 1335. | 44.77 | Fe XII | 517.0 | 42.15 |
| O II | 3903. | 43.46 | Si II | 1263. | 42.95 | Si XII | 506.4 | 44.17 |
| Ne III | 3870. | 42.45 | N V | 1240. | 45.36 | Ne VII | 465.2 | 42.39 |
| O III | 3762. | 45.68 | O V | 1218. | 45.64 | N III | 452.1 | 42.73 |
| O IV | 3409. | 42.72 | H I | 1207. | 46.92 | Fe XV | 418.4 | 42.60 |
| Si IV | 3160. | 42.01 | Si III | 1207. | 45.50 | Fe XV | 384.4 | 42.22 |
| O IV | 3066. | 42.45 | S III | 1198. | 44.77 | N III | 374.4 | 42.96 |
| O III | 3003. | 46.03 | Ne V | 1127. | 43.11 | O III | 374.1 | 43.92 |
| C II | 2837. | 43.22 | Si IV | 1126. | 42.49 | S XIV | 372.1 | 42.88 |
| Fe II | 2600. | 42.56 | Si III | 1112. | 42.15 | Fe XVI | 360.8 | 42.51 |
| Fe XII | 2406. | 43.36 | N II | 1085. | 43.55 | Fe XII | 360.1 | 43.53 |
| Si II | 2325. | 42.50 | S IV | 1070. | 46.03 | Fe XII | 357.2 | 43.01 |
| C III | 2296. | 42.31 | O VI | 1034. | 46.20 | Fe XI | 354.5 | 42.23 |
| C III | 2141. | 42.30 | H I | 1026. | 45.90 | Si X | 353.1 | 43.73 |
| Si VII | 2128. | 42.25 | Ne VI | 1020. | 43.86 | Si IX | 347.4 | 42.83 |
| C III | 1909. | 46.42 | N III | 991. | 46.33 | He II | 303.9 | 44.78 |

FIG. 17a



| Ion | Wave-length (L) | Log (L) | Ion | Wave-length (L) | Log (L) | Ion | Wave-length (L) | Log (L) |
|---------|-----------------|---------|----------|-----------------|---------|--------|-----------------|---------|
| Si V | 7.12 | 41.48 | Fe XX | 1.91 | 41.29 | Fe VI | 1.76 | 41.58 |
| S XV | 5.10 | 40.41 | Fe XXI | 1.89 | 41.28 | Fe VII | 1.76 | 40.87 |
| S XV | 5.07 | 40.97 | Fe XXII | 1.89 | 41.08 | Fe VII | 1.76 | 40.48 |
| S XVI | 4.73 | 40.43 | Fe XXIII | 1.87 | 41.00 | Fe IX | 1.76 | 40.25 |
| S XV | 4.30 | 40.31 | Fe XXV | 1.87 | 41.05 | Fe XI | 1.75 | 40.34 |
| Fe XVI | 1.94 | 41.23 | Fe XXV | 1.86 | 41.53 | Fe XII | 1.75 | 40.62 |
| Fe XVII | 1.94 | 40.47 | Fe XXV | 1.85 | 40.39 | Fe XII | 1.75 | 41.01 |

FIG. 17b

FIG. 17.—Radiation spectrum from model 5 at $\log \xi = 1.0$

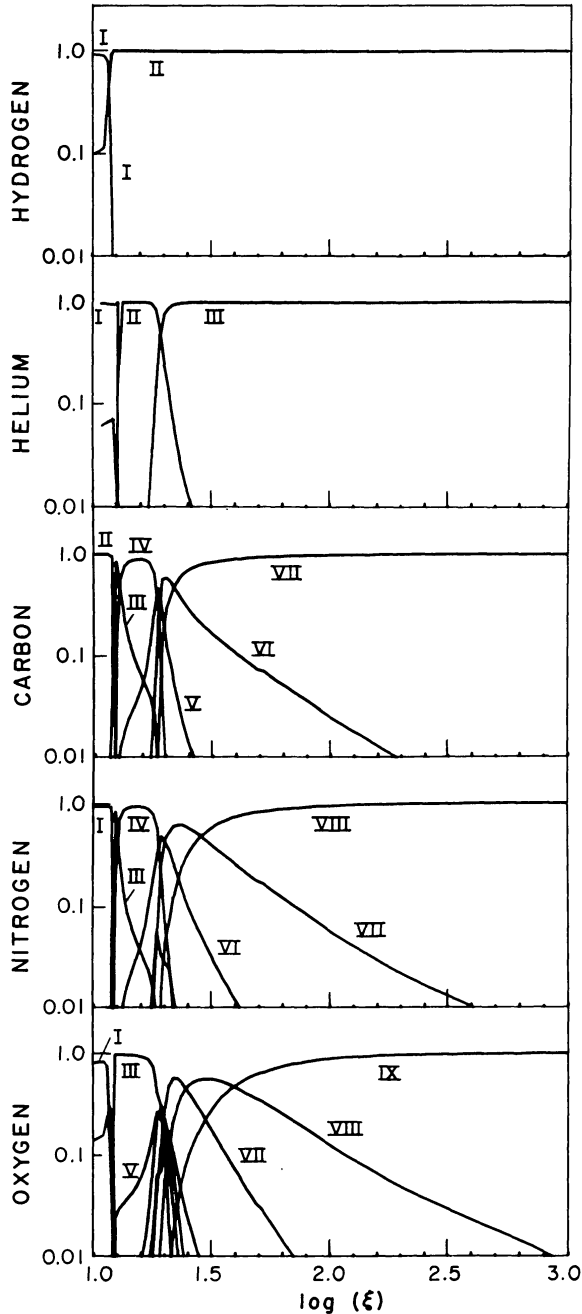


FIG. 18a

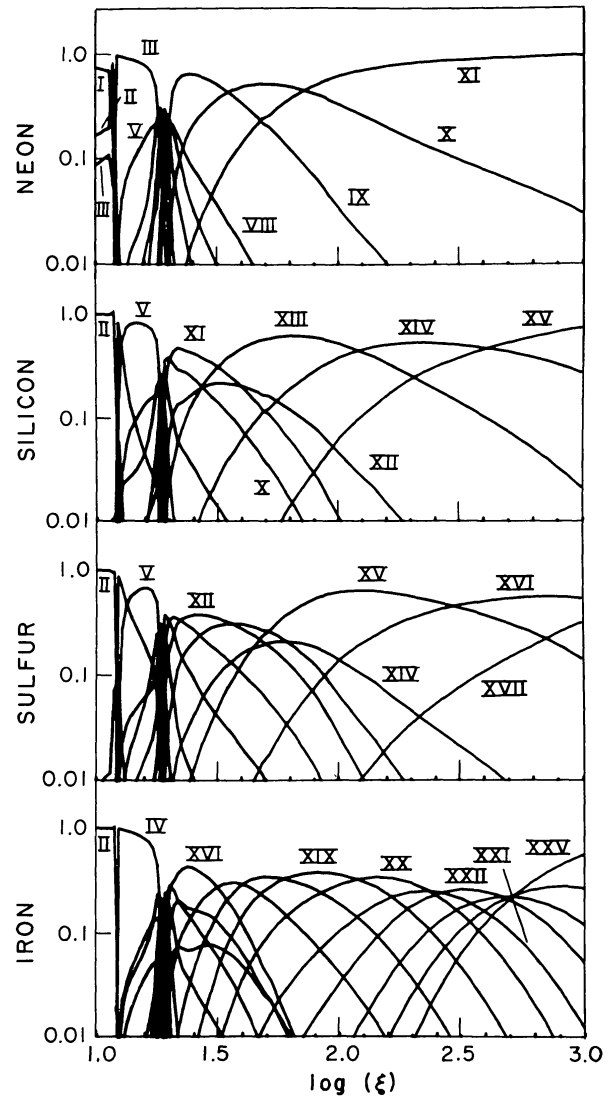


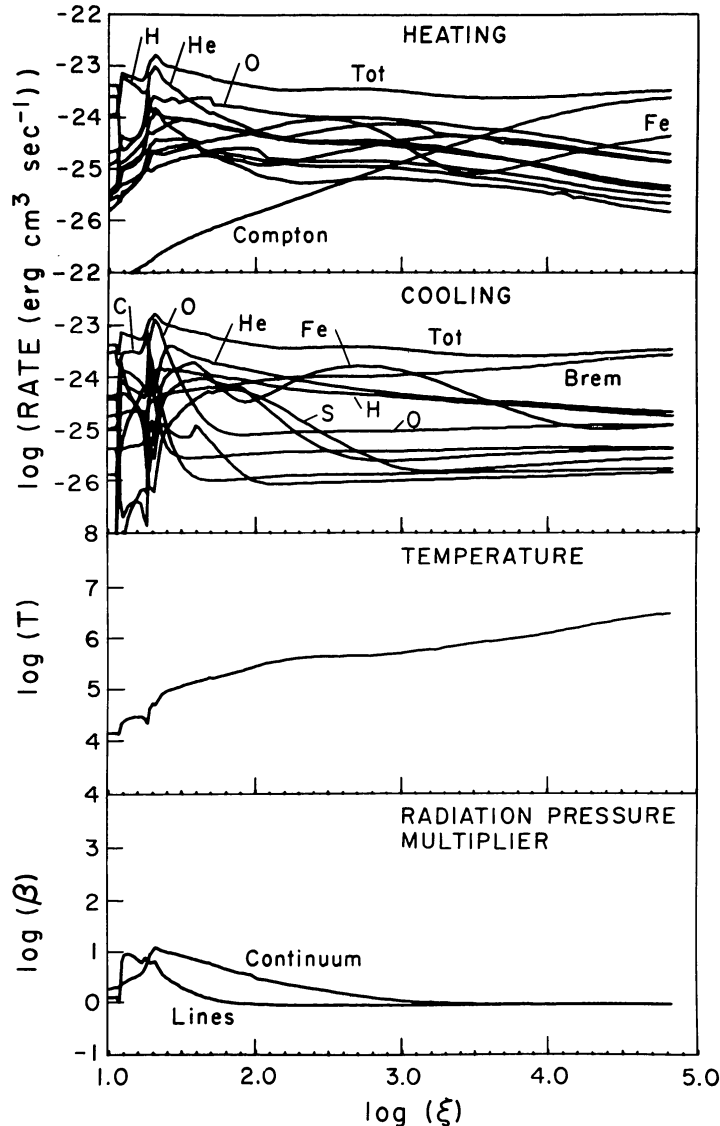
FIG. 18b

FIG. 18.—Ionization structure of model 6 for $1 < \log \xi < 3$

8, which has a blackbody input spectrum with $kT = 4$ keV, and the same source luminosity and gas density as model 4. Model 8 is representative of compact sources which have intrinsic low energy cutoffs, due either to absorption by gas close to the source or to optically thick thermal emission.

Figure 24 shows the temperature of model 8 as a function of $\log \xi$. The thermally unstable region is apparent near $\log \xi \approx 2.7$, where the gas temperature can

have three different values. This multiple-valued behavior may be understood in the following way. In the absence of a strong flux of soft photons, the cooling due to collisional excitation of He II Ly α and O VI $\lambda 1034$ can cause the net heating minus cooling, $\mathcal{L}(T)$, to have an unstable region where $d\mathcal{L}/dT > 0$. In the unstable region, the thermal equilibrium equation, $\mathcal{L}(T) = 0$, has three different solutions, and which one obtains depends on the past history of the gas. If the gas is flowing out

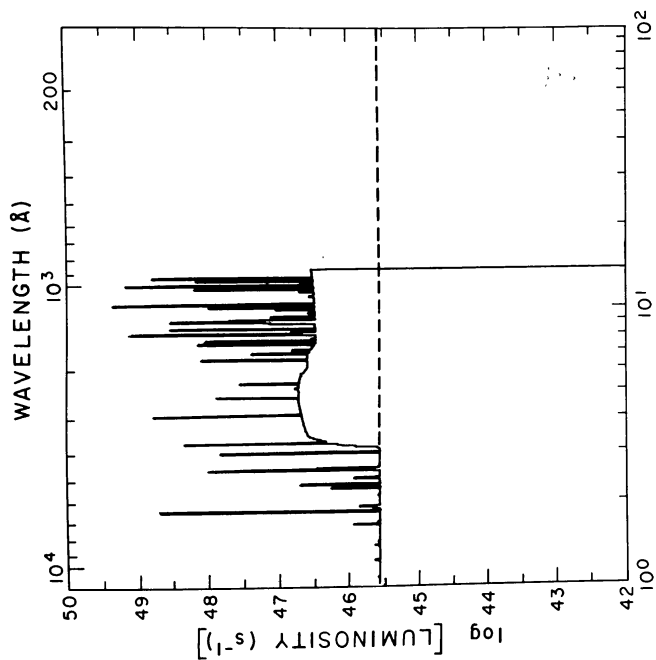
FIG. 19.—Thermal structure of model 6 for $1 < \log \xi < 5$

from the source, it will stay on the high temperature stable solution until that solution no longer exists, at which point the temperature must jump discontinuously to the low temperature stable solution. If the gas is flowing in toward the source, it will stay on the low temperature branch until it must jump discontinuously to the hot solution. The intervening unstable solution is not physically realizable.

The temperature solutions for inflowing and outflowing gas are shown as the solid curves in Figure 24, and the unstable solution is shown as the dashed curve. These solutions are found by using a secant method to solve the thermal equilibrium equation at each radius step. In the region where this equation has more than one solution, the secant method finds the stable solution closest to the initial temperature guess. Thus, the out-

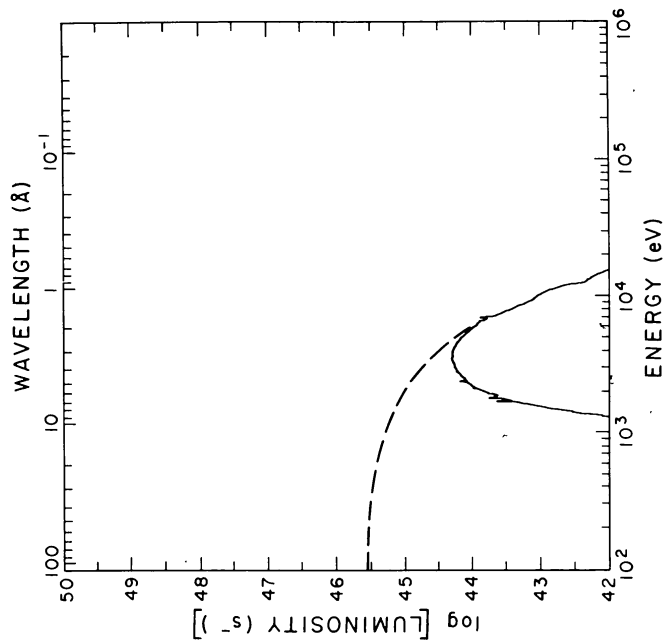
flow solution is found by adopting as a temperature guess at each successive radius step the temperature solution found at the previous radius. The inflow solution is found by taking a low temperature guess at each radius step, $T \approx 5 \times 10^4$ K. The unstable solution is found using the procedure outlined by HBM, that is, by assuming that the gas is optically thin, treating the temperature as an independent variable, and solving the thermal equilibrium equation to find the radius.

Line trapping plays an important role in suppressing the cooling function and reducing the extent of the unstable region (London, McCray, and Auer 1981). This effect is evident when Figure 24 is compared with the results of models 3 and 4 of HBM. Line trapping causes the unstable region in our model 8 to span a region $\Delta \log \xi \approx 0.1$, compared with $\Delta \log \xi \approx 1.0$ found by HBM.



| Ion | Wave-length (Å) | Log (L) | Ion | Wave-length (Å) | Log (L) | Ion | Wave-length (Å) | Log (L) |
|---------|-----------------|---------|---------|-----------------|---------|----------|-----------------|---------|
| Si X | 14306. | 43.27 | O IV | 3066. | 43.12 | N IV | 1488. | 46.48 |
| O I | 11287. | 40.87 | O III | 3003. | 46.54 | S XI | 1482. | 43.65 |
| S VII | 9872. | 42.35 | Ne VIII | 2860. | 41.41 | O IV | 1407. | 45.23 |
| S III | 8834. | 41.44 | C II | 2837. | 41.84 | Si IV | 1397. | 45.99 |
| O I | 8692. | 40.79 | Ne III | 2678. | 45.09 | O V | 1385. | 45.25 |
| N I | 8447. | 41.16 | Fe II | 2600. | 45.09 | Fe XI | 1371. | 42.41 |
| S XII | 7358. | 43.69 | Si III | 2559. | 40.78 | Fe XII | 1343. | 42.95 |
| S II | 7324. | 41.66 | Ne III | 2413. | 40.74 | C II | 1335. | 44.53 |
| C II | 6880. | 41.84 | Fe XII | 2406. | 43.91 | S X | 1305. | 42.41 |
| H I | 6563. | 46.42 | Ne IV | 2362. | 41.26 | O I | 1304. | 43.17 |
| Fe X | 6376. | 43.29 | C II | 2326. | 42.82 | Si II | 1263. | 44.43 |
| Si II | 6355. | 41.85 | Si II | 2325. | 44.72 | N V | 1240. | 45.99 |
| C IV | 5805. | 42.64 | C III | 2296. | 42.72 | O V | 1218. | 46.42 |
| Fe XIII | 5438. | 44.11 | Ne V | 2269. | 41.15 | H I | 1216. | 47.03 |
| Fe XIV | 5304. | 44.54 | Si II | 2141. | 42.36 | Si III | 1207. | 45.03 |
| Si II | 5051. | 42.00 | Si VII | 2128. | 43.27 | N I | 1200. | 42.69 |
| O III | 5007. | 42.43 | Ne VI | 2047. | 40.86 | S III | 1198. | 44.63 |
| He II | 4686. | 45.36 | S VI | 1987. | 40.86 | N I | 1135. | 42.30 |
| O II | 4652. | 43.01 | C III | 1909. | 45.40 | Ne V | 1127. | 44.14 |
| N III | 4641. | 45.79 | Si III | 1895. | 44.85 | Si IV | 1126. | 42.23 |
| N II | 4623. | 41.39 | Si IX | 1888. | 43.04 | Si III | 1112. | 41.05 |
| N III | 4099. | 45.55 | Si II | 1814. | 45.51 | N II | 1085. | 43.45 |
| Si IV | 4098. | 41.57 | N III | 1750. | 43.77 | S IV | 1070. | 45.75 |
| O II | 3903. | 42.68 | S IX | 1724. | 43.07 | O VI | 1034. | 46.94 |
| Ne II | 3870. | 41.96 | Si IV | 1724. | 41.38 | H I | 1026. | 44.87 |
| Si II | 3858. | 41.46 | Ne IV | 1719. | 41.99 | Ne VI | 1020. | 44.56 |
| S III | 3840. | 40.61 | S III | 1667. | 43.14 | Si II | 991.7 | 42.08 |
| O VI | 3819. | 42.33 | O III | 1663. | 45.99 | N III | 991.0 | 45.98 |
| O III | 3762. | 46.20 | He II | 1640. | 46.17 | C III | 977.0 | 46.32 |
| Ne V | 3726. | 41.55 | Fe II | 1608. | 42.82 | Fe XVIII | 974.7 | 44.33 |
| O IV | 3409. | 43.39 | C IV | 1549. | 46.78 | N I | 964.4 | 41.51 |

FIG. 20a



| Ion | Wave-length (Å) | Log (L) | Ion | Wave-length (Å) | Log (L) | Ion | Wave-length (Å) | Log (L) |
|---------|-----------------|---------|----------|-----------------|---------|---------|-----------------|---------|
| Si V | 7.12 | 41.26 | S XVI | 3.99 | 38.80 | Fe IV | 1.76 | 39.72 |
| Si XII | 6.74 | 41.21 | Fe XVI | 1.94 | 40.42 | Fe V | 1.76 | 41.22 |
| Si XIII | 6.68 | 41.15 | Fe XVII | 1.94 | 39.72 | Fe VI | 1.76 | 40.12 |
| Si XIII | 6.65 | 40.03 | Fe XVIII | 1.93 | 40.13 | Fe VII | 1.76 | 39.56 |
| Si XIV | 6.68 | 40.65 | Fe XIX | 1.92 | 40.37 | Fe VIII | 1.76 | 39.37 |
| Si XIV | 5.68 | 40.98 | Fe XX | 1.91 | 40.47 | Fe IX | 1.76 | 39.21 |
| S VII | 5.36 | 38.45 | Fe XXI | 1.89 | 40.38 | Fe X | 1.76 | 39.09 |
| Si XIV | 5.22 | 39.37 | Fe XXII | 1.89 | 40.13 | Fe XI | 1.75 | 39.33 |
| S XV | 5.10 | 41.04 | Fe XXIII | 1.87 | 39.98 | Fe XII | 1.75 | 39.62 |
| S XV | 5.07 | 41.55 | Fe XXV | 1.87 | 39.99 | Fe XIII | 1.75 | 40.04 |
| S XV | 5.04 | 39.99 | Fe XXV | 1.86 | 40.47 | Fe XV | 1.74 | 40.85 |

FIG. 20b

FIG. 20.—Radiation spectrum from model 6 at $\log \xi = 1.0$

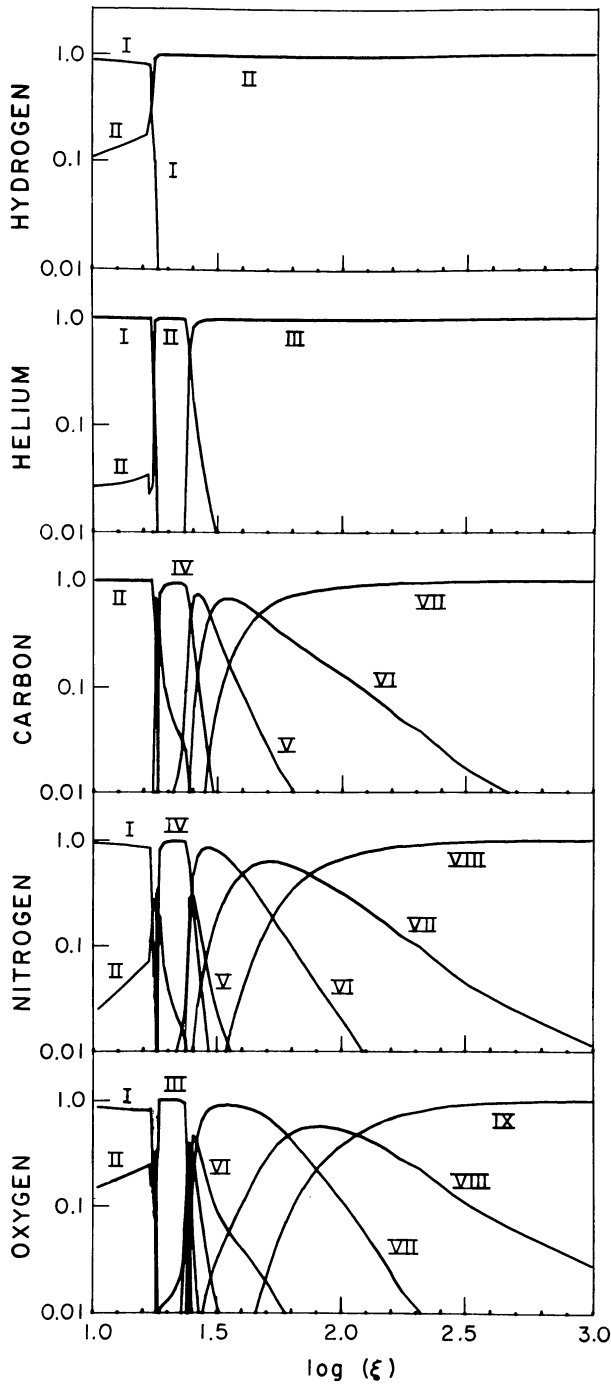


FIG. 21a

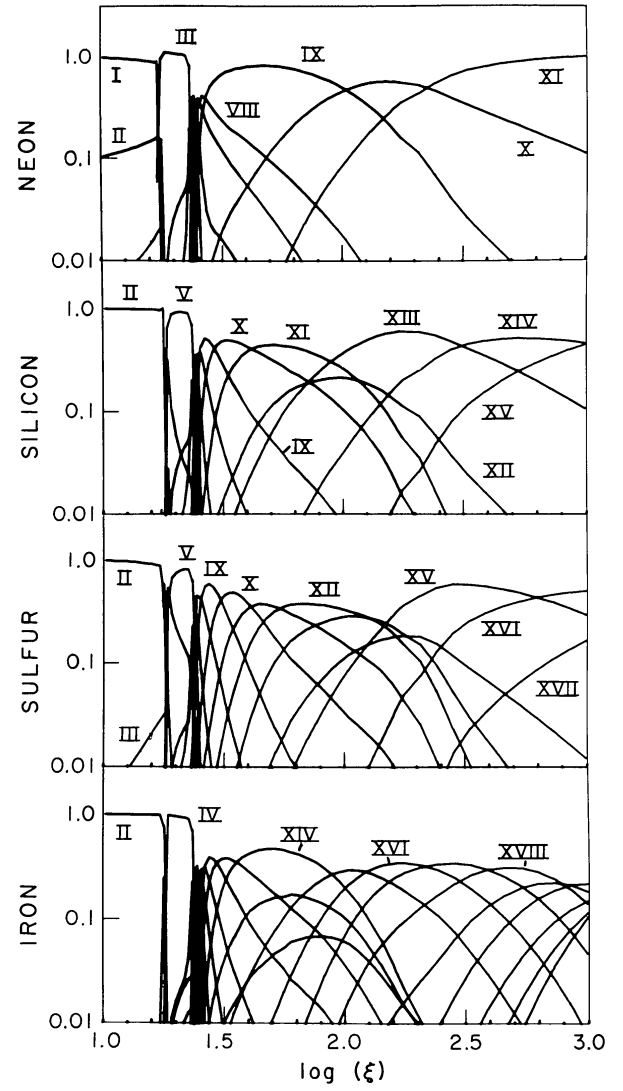


FIG. 21b

FIG. 21.—Ionization structure of model 7 for $1 < \log \xi < 3$

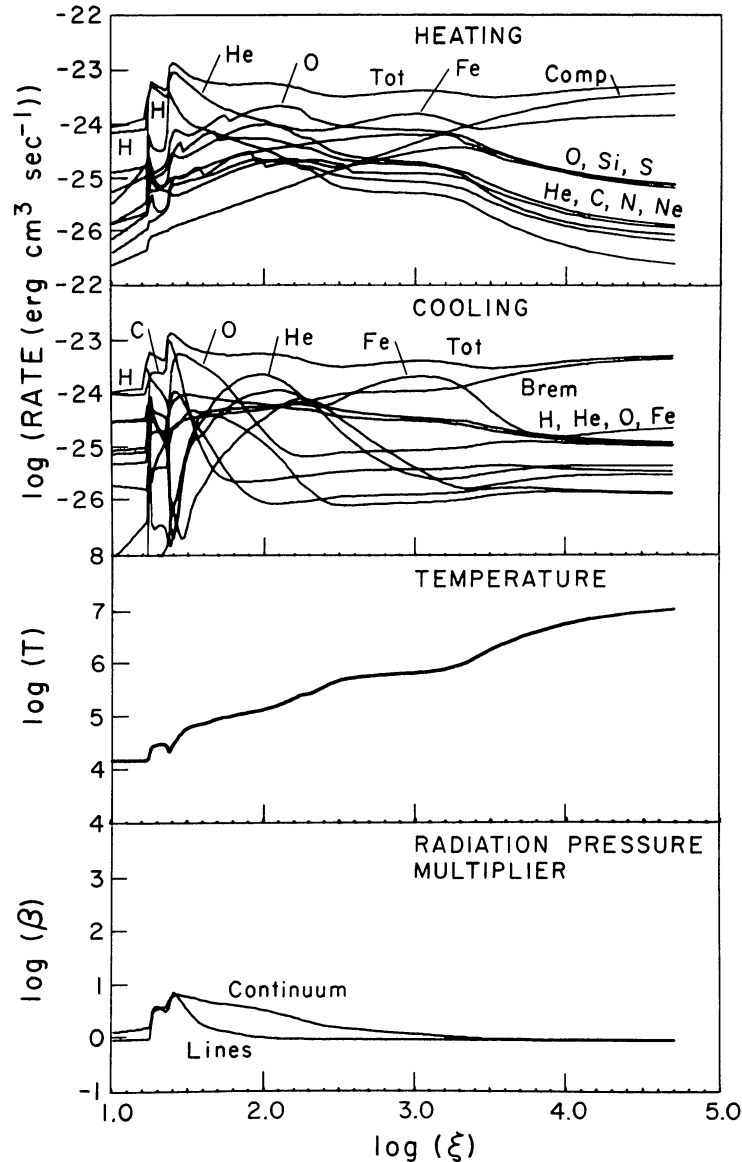


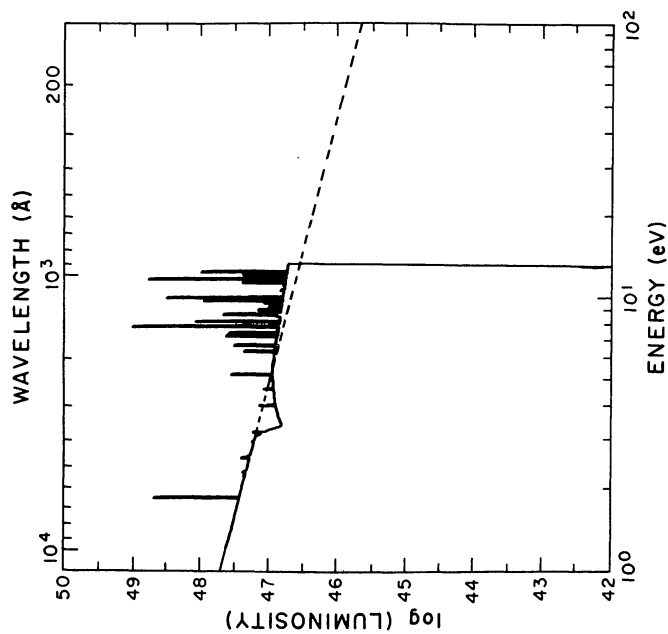
FIG. 22.—Thermal structure of model 7

The extent of the unstable region is also sensitive to our assumptions that the cloud density is constant. If, for example, the gas pressure is specified rather than the density, the gas density will increase sharply from the hot to the cool solution. This causes the ionization parameter ξ to decrease sharply and increases the range of ξ for which the gas is unstable. Constant pressure clouds are expected to occur in the broad-line emitting regions of quasars and active galaxies (Davidson and Netzer 1979; Kwan and Krolik 1981; Krolik, McKee, and Tarter 1981).

Figure 25*a, b* shows the ionization structure of model 8 as a function of $\log \xi$, for gas flowing out from the source. The structure shown here reflects the thermal structure shown in Figure 24—for $\log \xi \geq 2.7$, the gas is

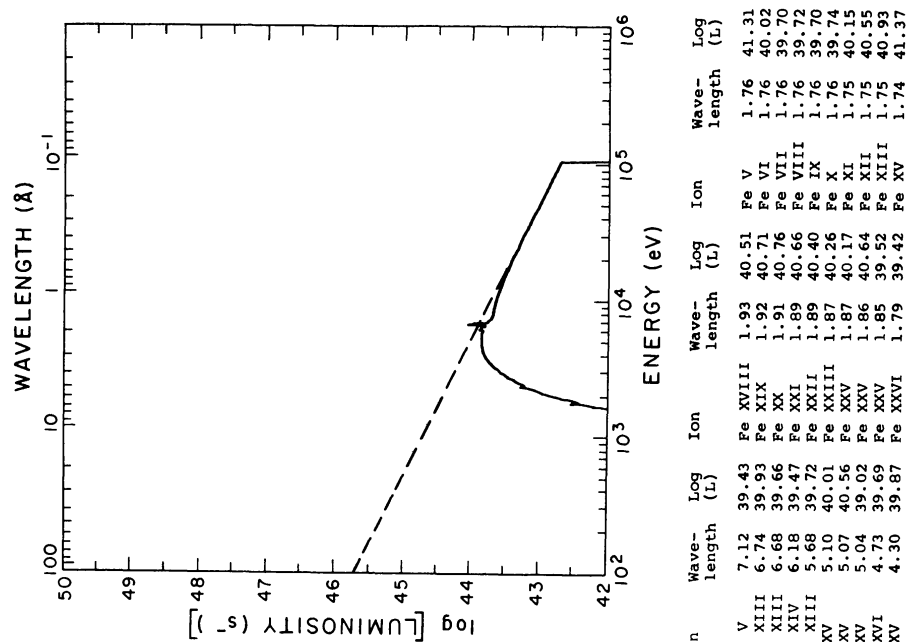
hot and ionized and resembles the results of previous models in the same region. At $\log \xi \approx 2.7$, helium recombines to He II, and the sharp drop in temperature results in the recombination of many of the other ions in the gas. The ionization structure in this region depends on which stable temperature solution is chosen—the cool, inflowing solution has a He II ionization front at $\log \xi \approx 2.8$. At $\log \xi < 2.7$, the ionization of trace elements is controlled by secondary emissions by the cloud. The ionization of hydrogen is controlled by collisional ionization by fast photoelectrons and Auger electrons.

The spectrum emergent from model 8 depends strongly on which of the two stable solutions the gas chooses. Figures 26*a, b* and 27*a, b* show the spectrum at $\log \xi = 2.78$ for gas on the two different solutions. Both



| Ion | Wave-length | Log | Ion | Wave-length | Log |
|--------|-------------|-------|---------|-------------|-------|
| | | (L) | | | (L) |
| Si X | 14306. | 43.29 | Ne V | 3726. | 40.91 |
| O I | 11257. | 42.32 | O IV | 3409. | 42.15 |
| O VII | 9872. | 42.51 | Si IV | 3160. | 41.28 |
| N V | 9829. | 43.05 | O IV | 3066. | 42.06 |
| S III | 8834. | 41.25 | O III | 3003. | 44.78 |
| N I | 8692. | 43.05 | Ne VIII | 2860. | 41.80 |
| O I | 8447. | 42.34 | C II | 2837. | 41.26 |
| S XII | 7358. | 43.34 | Fe II | 2600. | 44.56 |
| C II | 7234. | 41.32 | Fe XII | 2406. | 43.98 |
| C II | 6580. | 41.47 | C II | 2326. | 43.73 |
| H I | 6563. | 46.68 | Si II | 2325. | 45.45 |
| Fe X | 6376. | 43.28 | C III | 2296. | 42.10 |
| C IV | 5805. | 41.57 | N II | 2141. | 42.62 |
| Fe XII | 5438. | 44.18 | Si VII | 2128. | 42.57 |
| Fe XIV | 5304. | 44.41 | Ne VI | 2047. | 40.90 |
| Si II | 5051. | 43.28 | S VI | 1987. | 40.71 |
| O III | 5007. | 42.16 | C III | 1909. | 44.94 |
| He II | 4866. | 44.83 | Si III | 1895. | 44.84 |
| O II | 4852. | 42.74 | Si IX | 1895. | 43.19 |
| N III | 4823. | 41.03 | Si II | 1888. | 43.19 |
| N V | 4809. | 41.25 | S IX | 1750. | 45.41 |
| N III | 4099. | 44.02 | Si IV | 1724. | 43.32 |
| Si IV | 4098. | 41.16 | S III | 1674. | 43.10 |
| O II | 3903. | 42.37 | O III | 1663. | 45.56 |
| Ne III | 3870. | 41.74 | He II | 1640. | 45.52 |
| Si II | 3858. | 42.74 | Fe II | 1608. | 43.60 |

Fig. 23a



| Ion | Wave-length | Log | Ion | Wave-length | Log |
|---------|-------------|-------|----------|-------------|-------|
| | | (L) | | | (L) |
| Si V | 7.12 | 39.43 | Fe XVIII | 1.93 | 40.51 |
| Si XIII | 6.74 | 39.93 | Fe XIX | 1.92 | 40.71 |
| Si XIV | 6.68 | 39.66 | Fe XX | 1.91 | 40.76 |
| Si XIV | 5.18 | 39.47 | Fe XXI | 1.89 | 40.66 |
| Si XIII | 5.68 | 39.72 | Fe XXII | 1.89 | 40.40 |
| S XV | 5.10 | 40.01 | Fe XXIII | 1.87 | 40.26 |
| S XV | 5.07 | 40.56 | Fe XXV | 1.87 | 40.17 |
| S XV | 5.04 | 39.02 | Fe XXV | 1.86 | 40.64 |
| S XVI | 4.73 | 39.69 | Fe XXV | 1.85 | 39.52 |
| S XV | 4.30 | 39.87 | Fe XXVI | 1.79 | 39.42 |
| | | | Fe XV | 1.74 | 41.37 |
| | | | Fe V | 1.76 | 41.31 |
| | | | Fe VI | 1.76 | 40.02 |
| | | | Fe VII | 1.76 | 39.70 |
| | | | Fe VIII | 1.76 | 39.72 |
| | | | Fe IX | 1.76 | 39.70 |
| | | | Fe X | 1.76 | 39.74 |
| | | | Fe XI | 1.75 | 40.15 |
| | | | Fe XII | 1.75 | 40.55 |
| | | | Fe XIII | 1.75 | 40.93 |

Fig. 23b

Fig. 23.—Radiation spectrum from model 7 at $\log \xi = 1.0$

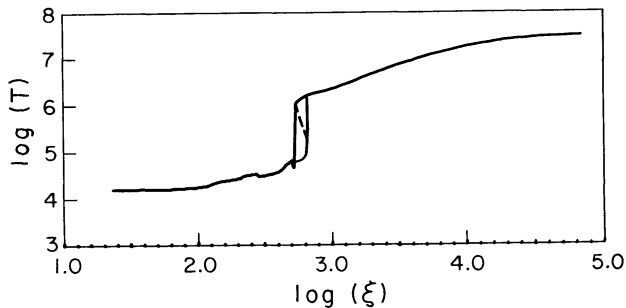


FIG. 24.—Temperature structure of model 8. Temperature is shown as a function of $\log \xi$ for $1 < \log \xi < 5$. Left (right) vertical discontinuities at $\log \xi \approx 2.7$ (2.8) represent the outflowing (inflowing) solutions. Dashed curve: thermally unstable solution.

figures show the effect of helium and hydrogen recombination emission at photon energies above 13.6 eV. In the spectrum corresponding to the outflow solution, shown in Figure 26*a, b*, the gas is hot and ionized, resulting in few emission or absorption features. In contrast, the spectrum of the inflow solution, displayed in Figure 27*a, b*, shows prominent emission lines of hydrogen, He II, N III, and O III Bowen lines, and C IV, N V, and O VI lines, in addition to He II continuum absorption. Strong EUV lines, such as O III $\lambda 374$, He II, Ly α , O V $\lambda 629$, and N III $\lambda 691$ are also emitted.

For $\log \xi < 2.7$ the emissivity of the gas is a single-valued function of ξ , and spectral features formed in this region may mask those formed in the unstable region.

i) Ion Column Densities

The ion column densities from our models illustrate many of the points discussed so far. The logarithmic column densities for the ions in each model are given in Table 3, which lists also the value of $\log \xi$ at the cloud edge and the value of $\log (Ln)^{1/2}$. Comparison of the results of models 1–3 illustrate the validity of the $(Ln)^{1/2}$ scaling laws derived in equation (32)—the scaling law holds for the ions with charge greater than 3 in models 1 and 2 and for the fully stripped ions in models 1, 2, and 3. For less highly ionized species, the column densities increase as a lower power of Ln , as expected from equation (31).

As demonstrated by the results of models 1 and 2, the $(Ln)^{1/2}$ scaling law can be used to predict column densities of ions with charge ≥ 3 for small values of Ln . As suggested by McCray, Wright, and Hatchett (1977), the column density of ion j of element i can be parametrized according to the formula

$$N_i^j = A_i K_i^j \left(\frac{Ln}{10^{38} \text{ ergs cm}^{-3} \text{ s}^{-1}} \right)^{1/2} \quad (36)$$

where A_i is the element abundance. In Table 4 we present the parameters K_i^j , in units of 10^{18} cm^2 , for a

variety of different X-ray source spectra. The parameters were calculated from the ion column densities of optically thin model clouds, with source spectra corresponding to models 4–9: 10 keV bremsstrahlung, 10 keV bremsstrahlung + 30,000 K blackbody, 2 keV bremsstrahlung, ϵ^{-1} power law, and 4 keV blackbody, for both inflowing and outflowing gas. These parameters, together with the $(Ln)^{1/2}$ scaling law, may be used to predict the ion column densities produced by cosmic X-ray sources in low density gas, such as the interstellar medium. The X-ray ionization may then be observable in the form of UV absorption lines, such as O VI $\lambda 1034$ (McCray, Wright, and Hatchett 1977).

VII. SUMMARY

In this paper, we have explored the details of the interaction of X-rays and gas in clouds by constructing a simple, general class of models, characterized by a source of X-rays at the center of a stationary, spherical, constant density cloud. The assumptions of our model—in particular, those of constant density gas and negligible velocity gradients—may need to be modified to describe the physical conditions in gas around particular X-ray sources. However, our models illustrate the processes that occur in all X-ray illuminated clouds and serve as an important first step toward making more accurate, specialized models for particular objects.

Our models for X-ray illuminated clouds span a wide range of physical parameters and embody a variety of physical processes. Use of these models is simplified, however, by the existence of simple scaling laws. For optically thin clouds the ionization and temperature in the clouds depend only on the X-ray source spectrum and on the ionization parameter, denoted ξ , which is the ratio of the X-ray flux to the gas density. Ionized column densities increase with Ln , the product of the X-ray source luminosity with gas density. Absorption of X-rays affects the ionization and temperature structure of the cloud for $Ln \geq 10^{40} \text{ ergs cm}^{-3} \text{ s}^{-1}$. As Ln is increased past this value, the gas shows sharp ionization fronts, and the spectrum emergent from the clouds shows photoelectric absorption edges and emission lines and continua. These spectral features are formed in a narrow region of the cloud, in the vicinity of the ionization fronts, where the gas temperature and ionization are changing rapidly with position.

At large Ln , the model results are affected by resonance line trapping, resulting in (a) suppression of line cooling, leading to higher gas temperature; (b) buildup of excited atomic level populations, leading to enhanced ionization rates, recombination continuum emission, and subordinate (e.g., H α) line luminosities; (c) splitting of resonance lines, such as Ly β , into subordinate lines such as H α ; and (d) conversion of He II Ly α photons into

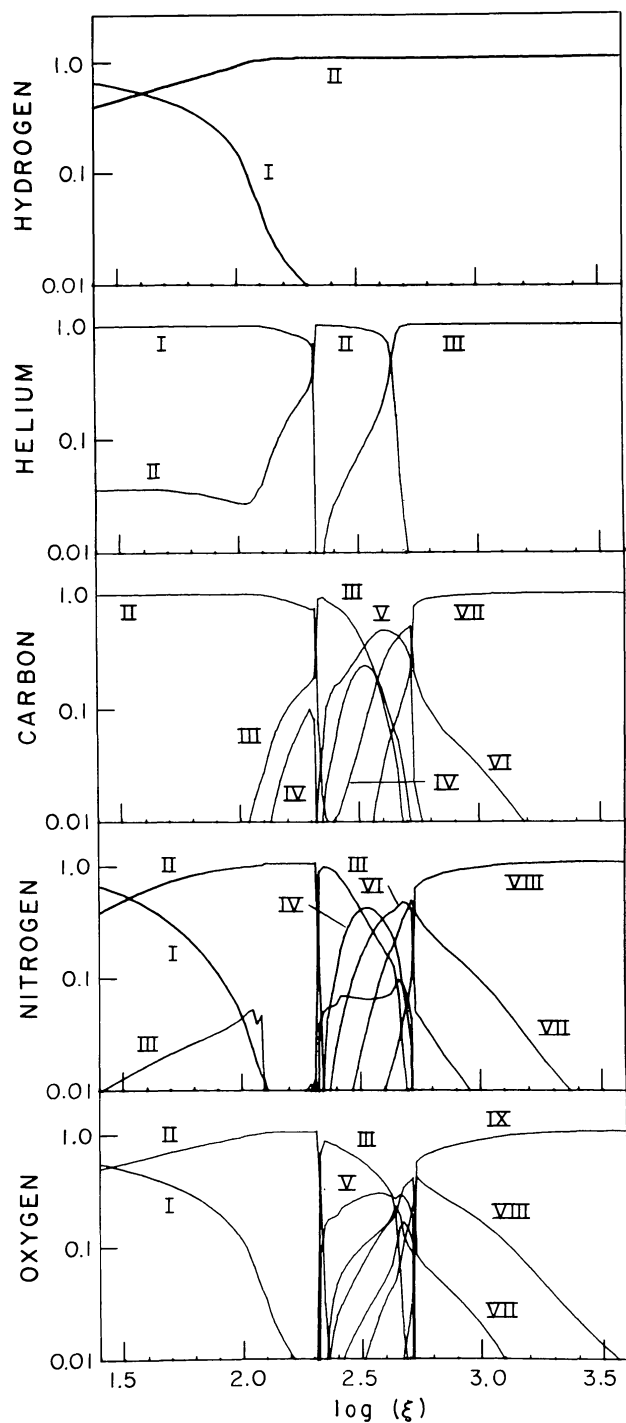


FIG. 25a

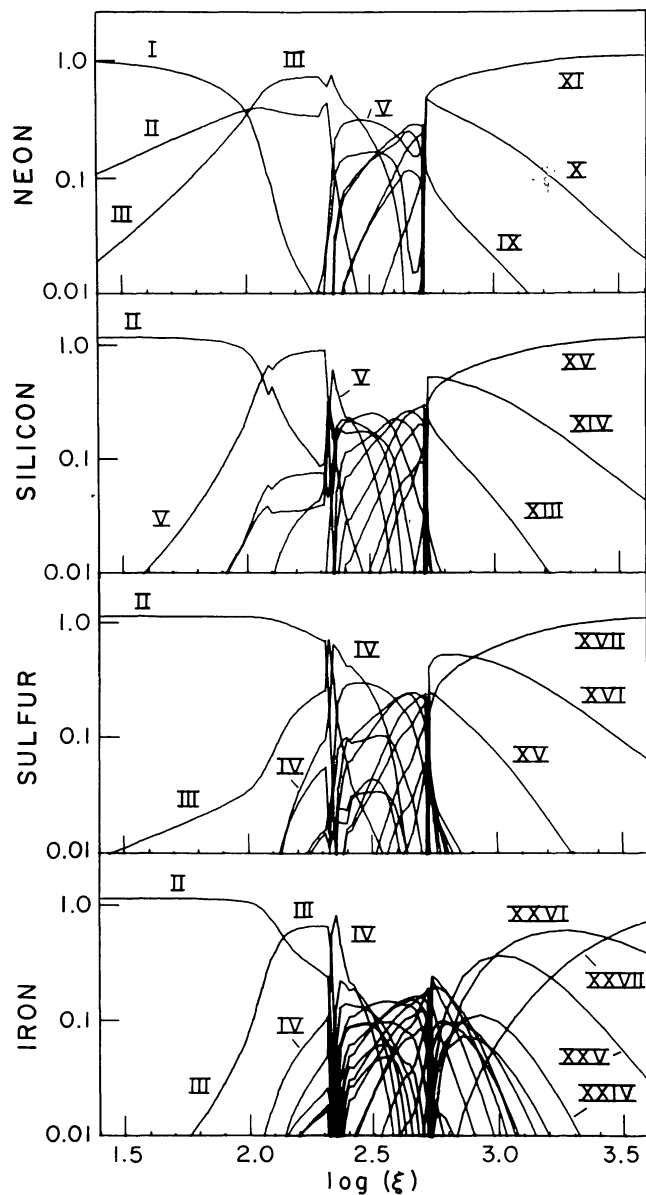
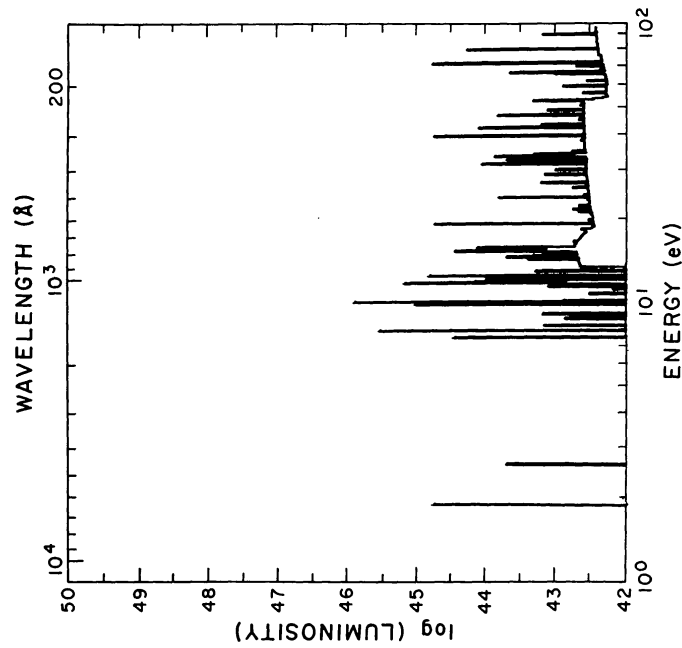


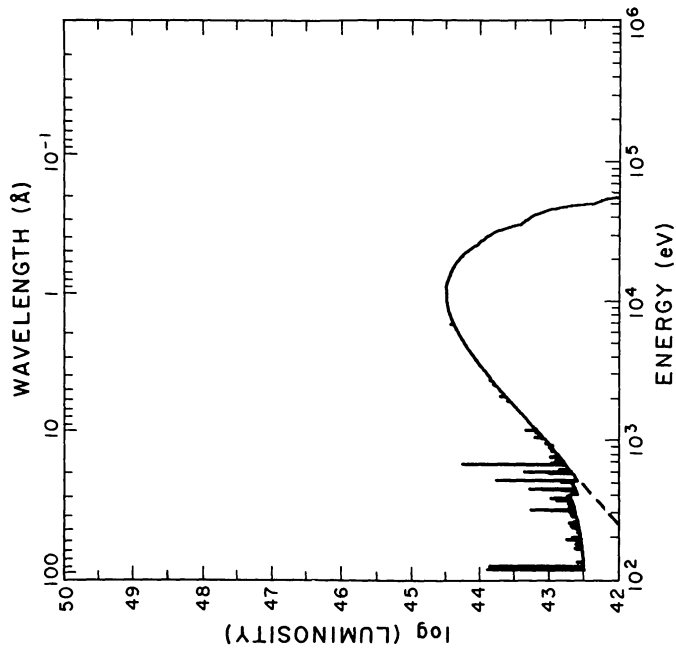
FIG. 25b

FIG. 25.—Ionization structure of model 8 for outflowing gas for $1.5 < \log \xi < 3.5$



| Ion | Wave-length (Å) | Log (L) | Ion | Wave-length (Å) | Log (L) |
|---------|-----------------|---------|---------|-----------------|---------|
| H I | 6563.00 | 42.79 | S V | 786.50 | 41.02 |
| He II | 4686.00 | 41.74 | Ne VIII | 773.70 | 40.96 |
| O VI | 3819.00 | 39.79 | N IV | 773.10 | 42.13 |
| Si II | 1892.00 | 40.09 | He II | 729.80 | 38.80 |
| Si II | 1814.00 | 39.61 | Si IX | 666.60 | 39.84 |
| He II | 1640.00 | 42.50 | S IV | 661.40 | 40.02 |
| C IV | 1549.00 | 43.59 | O V | 629.70 | 42.78 |
| N IV | 1488.00 | 41.17 | Si XI | 609.80 | 39.71 |
| Si IV | 1397.00 | 40.87 | He I | 584.30 | 39.11 |
| C II | 1382.00 | 41.21 | Ne V | 571.00 | 40.22 |
| Si II | 1323.00 | 39.14 | Ne VI | 561.40 | 40.41 |
| N V | 1261.00 | 43.05 | He IV | 542.80 | 39.81 |
| H I | 1218.00 | 43.11 | He X | 537.00 | 39.15 |
| Si III | 1215.00 | 43.66 | Si XII | 532.00 | 39.45 |
| Si III | 1198.00 | 40.51 | S XII | 507.40 | 38.52 |
| Ne V | 1129.00 | 40.51 | Ne VII | 465.20 | 39.78 |
| S IV | 1095.00 | 40.15 | Fe XII | 449.20 | 40.38 |
| H I | 1034.00 | 43.22 | C IV | 419.70 | 39.11 |
| S VI | 1030.00 | 43.22 | Fe XVI | 418.40 | 39.47 |
| H I | 1026.00 | 42.02 | Fe XII | 401.60 | 40.04 |
| Ne VI | 1020.00 | 40.89 | C IV | 394.40 | 42.87 |
| C III | 997.00 | 42.02 | Fe XIV | 384.10 | 39.82 |
| Fe XVII | 974.70 | 40.95 | Fe XVI | 372.10 | 41.69 |
| S VI | 937.10 | 41.30 | Fe XII | 360.80 | 41.82 |
| Fe XXII | 846.00 | 41.32 | Fe XII | 357.20 | 40.30 |
| O III | 834.50 | 41.68 | Fe X | 355.40 | 39.28 |
| O II | 833.80 | 39.69 | Fe XI | 354.50 | 39.69 |

FIG. 27a



| Ion | Wave-length (Å) | Log (L) | Ion | Wave-length (Å) | Log (L) |
|----------|-----------------|---------|----------|-----------------|---------|
| Fe XIX | 108.00 | 41.88 | C V | 34.97 | 40.50 |
| Fe XVIII | 104.00 | 41.41 | S XIV | 33.50 | 39.89 |
| Fe XVIII | 103.30 | 39.19 | Si XIV | 33.39 | 40.60 |
| Ne VIII | 103.00 | 39.56 | S XIV | 32.50 | 39.49 |
| O VIII | 102.50 | 41.85 | S XII | 32.41 | 39.39 |
| Fe XIV | 95.20 | 39.90 | Fe XXIII | 11.19 | 39.15 |
| Fe XIV | 93.20 | 39.86 | Fe XXIV | 10.80 | 40.88 |
| Fe XVI | 77.00 | 39.97 | Ne X | 10.26 | 39.29 |
| Fe XVI | 71.00 | 39.81 | Si XIII | 6.74 | 40.16 |
| Ne X | 68.30 | 39.69 | Si XIII | 6.68 | 40.54 |
| Fe XVI | 65.60 | 39.43 | S XVI | 6.53 | 39.52 |
| Fe XVI | 63.50 | 39.45 | O VIII | 22.10 | 40.74 |
| Fe XIV | 59.30 | 39.45 | O VIII | 21.80 | 40.76 |
| Si IX | 55.81 | 39.64 | S XVI | 20.94 | 40.35 |
| Fe XVI | 54.70 | 39.93 | O VIII | 19.00 | 42.26 |
| Fe XVI | 52.60 | 40.08 | S XVI | 18.63 | 40.53 |
| Si XI | 50.64 | 39.55 | Fe XIX | 17.86 | 40.25 |
| Fe XVI | 49.30 | 39.58 | Fe XVII | 16.77 | 40.43 |
| Si XI | 48.75 | 39.47 | Fe XVII | 15.28 | 39.96 |
| Si XII | 45.60 | 39.78 | Fe XVII | 13.00 | 39.74 |
| Si XII | 44.72 | 39.83 | Ne IX | 13.70 | 39.56 |
| Si XI | 43.76 | 39.77 | Fe XX | 13.50 | 39.72 |
| S X | 42.50 | 39.96 | Fe XX | 13.50 | 39.54 |
| Si XII | 40.32 | 39.91 | Ne IX | 13.50 | 39.55 |
| C V | 40.73 | 40.64 | Fe XX | 13.50 | 39.57 |
| C V | 40.27 | 41.17 | Fe XVIII | 12.42 | 40.19 |
| S XIII | 35.70 | 39.44 | Fe XXI | 12.30 | 39.74 |

FIG. 27b

FIG. 27.—Radiation spectrum from model 8 at $\log \xi = 2.78$ for inflowing gas

TABLE 3
LOGARITHMIC COLUMN DENSITIES

| Model | 1 | 2 | 3 | 4 | 5 | 6 | 7 | 8 (outflow) |
|--------------|-------|-------|-------|-------|-------|-------|-------|-------------|
| Log ξ | -3.0 | -1.38 | 1.16 | 0.99 | 1.0 | 1.00 | 0.99 | 0.97 |
| 1/2 Log (Ln) | 18.5 | 20.0 | 24.0 | 24.0 | 24.0 | 24.0 | 24.0 | 24.0 |
| H I | 19.71 | 20.47 | 22.75 | 22.84 | 18.09 | 22.41 | 22.75 | 23.06 |
| II | 19.52 | 20.12 | 23.24 | 23.32 | 23.44 | 23.40 | 23.34 | 23.21 |
| He I | 18.56 | 19.29 | 21.72 | 21.90 | 17.45 | 21.36 | 21.74 | 22.25 |
| II | 18.49 | 18.96 | 21.65 | 21.62 | 22.03 | 21.60 | 21.45 | 21.37 |
| III | 17.67 | 18.88 | 22.00 | 22.05 | 22.10 | 22.23 | 22.18 | 21.53 |
| C II | 16.43 | 17.07 | 19.41 | 19.56 | 16.28 | 19.05 | 19.40 | 19.91 |
| III | 15.59 | 16.39 | 18.17 | 18.67 | 19.48 | 18.40 | 18.16 | 18.67 |
| IV | 14.08 | 15.39 | 19.02 | 18.93 | 19.20 | 19.04 | 19.01 | 18.08 |
| V | 14.40 | 15.82 | 18.48 | 18.53 | 18.66 | 18.46 | 18.82 | 18.44 |
| VI | 14.00 | 15.52 | 18.83 | 18.88 | 18.97 | 19.00 | 19.15 | 18.24 |
| VII | 14.20 | 15.72 | 19.59 | 19.63 | 19.64 | 19.82 | 19.65 | 19.12 |
| N I | 15.66 | 16.39 | 18.76 | 18.82 | 10.45 | 18.39 | 18.74 | 18.99 |
| II | 15.40 | 15.82 | 17.25 | 18.28 | 15.34 | 17.34 | 17.60 | 18.96 |
| III | 14.08 | 15.19 | 17.43 | 17.98 | 18.82 | 17.64 | 17.40 | 18.06 |
| IV | 13.62 | 15.00 | 18.40 | 18.43 | 18.64 | 18.47 | 18.40 | 17.68 |
| V | 13.71 | 15.08 | 16.91 | 16.85 | 17.44 | 16.92 | 17.52 | 17.15 |
| VI | 13.40 | 14.88 | 17.98 | 18.03 | 18.15 | 18.08 | 18.49 | 17.62 |
| VII | 13.23 | 14.72 | 18.34 | 18.36 | 18.40 | 18.51 | 18.55 | 17.63 |
| VIII | 13.48 | 15.00 | 18.90 | 18.94 | 18.95 | 19.13 | 18.92 | 18.46 |
| O I | 16.38 | 17.08 | 19.36 | 19.42 | 11.46 | 19.02 | 19.36 | 19.63 |
| II | 16.04 | 16.55 | 18.88 | 19.23 | 16.62 | 18.48 | 18.82 | 19.73 |
| III | 14.86 | 15.89 | 19.10 | 19.21 | 19.72 | 19.23 | 19.08 | 18.69 |
| IV | 14.04 | 15.40 | 18.20 | 18.15 | 18.25 | 18.22 | 17.84 | 18.03 |
| V | 14.52 | 15.94 | 18.60 | 17.49 | 18.67 | 18.38 | 18.23 | 18.44 |
| VI | 13.91 | 15.36 | 18.08 | 17.83 | 18.38 | 18.07 | 18.53 | 17.62 |
| VII | 13.92 | 15.41 | 18.75 | 18.75 | 18.92 | 18.97 | 19.38 | 18.17 |
| VIII | 13.81 | 15.32 | 19.04 | 19.08 | 19.11 | 19.27 | 19.19 | 18.30 |
| IX | 14.11 | 15.62 | 19.54 | 19.59 | 19.59 | 19.76 | 19.53 | 19.14 |
| Ne I | 14.58 | 15.06 | 18.02 | 18.27 | 11.75 | 17.69 | 18.18 | 18.62 |
| II | 15.18 | 16.55 | 17.82 | 17.78 | 16.82 | 17.45 | 17.34 | 17.95 |
| III | 14.43 | 15.89 | 17.82 | 17.91 | 18.44 | 17.93 | 17.84 | 17.88 |
| IV | 13.20 | 14.48 | 16.95 | 17.05 | 17.05 | 16.88 | 16.55 | 16.96 |
| V | 12.97 | 14.40 | 17.34 | 17.48 | 17.55 | 17.22 | 16.81 | 17.20 |
| VI | 12.83 | 14.30 | 17.08 | 17.09 | 17.12 | 17.01 | 16.81 | 16.96 |
| VII | 12.73 | 14.23 | 17.20 | 17.11 | 17.34 | 17.11 | 17.30 | 16.90 |
| VIII | 12.49 | 13.96 | 17.11 | 16.95 | 17.25 | 17.17 | 17.55 | 16.47 |
| IX | 12.59 | 14.08 | 17.72 | 17.73 | 17.83 | 18.03 | 18.22 | 16.79 |
| X | 12.51 | 14.00 | 17.85 | 17.89 | 17.90 | 18.12 | 17.96 | 17.13 |
| XI | 12.75 | 14.28 | 18.23 | 18.28 | 18.27 | 18.40 | 18.15 | 17.89 |
| Si II | 15.41 | 16.05 | 18.35 | 18.50 | 13.88 | 17.99 | 18.34 | 18.80 |
| III | 12.38 | 13.45 | 15.86 | 16.40 | 16.49 | 16.16 | 16.27 | 16.63 |
| IV | 13.64 | 14.73 | 17.08 | 17.72 | 18.27 | 17.28 | 17.03 | 17.28 |
| V | 13.38 | 14.71 | 17.77 | 17.88 | 18.18 | 17.90 | 17.89 | 17.90 |
| VI | 13.00 | 14.43 | 17.04 | 17.23 | 17.41 | 16.92 | 16.77 | 17.25 |
| VII | 12.78 | 14.26 | 17.30 | 17.44 | 17.57 | 17.14 | 16.91 | 17.13 |
| VIII | 12.66 | 14.15 | 16.97 | 17.02 | 17.13 | 16.85 | 17.21 | 17.03 |

TABLE 3—Continued

| Model | 1 | 2 | 3 | 4 | 5 | 6 | 7 | 8 (outflow) |
|--------------|-------|-------|-------|-------|-------|-------|-------|-------------|
| Log ξ | -3.0 | -1.38 | 1.16 | 0.99 | 1.0 | 1.00 | 0.99 | 0.97 |
| 1/2 Log (Ln) | 18.5 | 20.0 | 24.0 | 24.0 | 24.0 | 24.0 | 24.0 | 24.0 |
| <hr/> | | | | | | | | |
| IX | 12.57 | 14.08 | 17.08 | 17.26 | 17.41 | 17.25 | 16.66 | 17.01 |
| X | 12.54 | 14.08 | 17.40 | 17.62 | 17.72 | 17.78 | 17.97 | 16.90 |
| XI | 12.53 | 14.04 | 17.68 | 17.69 | 17.76 | 17.93 | 17.99 | 16.70 |
| XII | 12.23 | 13.70 | 17.54 | 17.40 | 17.44 | 17.73 | 17.64 | 16.39 |
| XIII | 12.46 | 13.96 | 17.88 | 17.87 | 17.87 | 18.25 | 18.04 | 16.77 |
| XIV | 12.38 | 13.90 | 17.85 | 17.92 | 17.93 | 18.12 | 17.87 | 17.33 |
| XV | 12.61 | 14.15 | 18.11 | 18.16 | 18.16 | 18.13 | 17.92 | 17.92 |
| <hr/> | | | | | | | | |
| S II | 14.99 | 15.52 | 17.96 | 18.13 | 13.50 | 17.61 | 17.97 | 18.47 |
| III | 14.23 | 15.27 | 16.90 | 16.84 | 16.25 | 16.62 | 16.50 | 16.99 |
| IV | 12.88 | 14.15 | 16.83 | 17.56 | 18.05 | 17.20 | 16.97 | 17.10 |
| V | 12.74 | 14.08 | 17.40 | 17.24 | 17.57 | 17.45 | 17.42 | 16.06 |
| VI | 12.34 | 13.76 | 15.82 | 15.81 | 16.05 | 15.46 | 15.50 | 16.35 |
| VII | 12.38 | 13.84 | 16.72 | 16.76 | 16.86 | 16.61 | 16.55 | 16.47 |
| VIII | 12.41 | 13.89 | 16.82 | 17.02 | 17.25 | 16.69 | 16.97 | 16.88 |
| IX | 12.23 | 13.72 | 16.71 | 16.81 | 17.02 | 16.83 | 17.33 | 16.60 |
| X | 12.15 | 13.64 | 16.85 | 17.09 | 17.21 | 17.21 | 17.46 | 16.70 |
| XI | 12.08 | 13.60 | 17.08 | 17.28 | 17.33 | 17.44 | 17.50 | 16.45 |
| XII | 12.04 | 13.58 | 17.30 | 17.36 | 17.38 | 17.57 | 17.55 | 16.34 |
| XIII | 11.96 | 13.45 | 17.32 | 17.21 | 17.23 | 17.49 | 17.36 | 16.05 |
| XIV | 11.72 | 13.18 | 17.15 | 16.97 | 16.98 | 17.35 | 17.10 | 15.84 |
| XV | 11.98 | 13.48 | 17.43 | 17.44 | 17.44 | 17.86 | 17.56 | 16.44 |
| XVI | 11.95 | 13.48 | 17.45 | 17.54 | 17.55 | 17.65 | 17.41 | 17.04 |
| XVII | 12.15 | 13.65 | 17.63 | 17.67 | 17.66 | 17.48 | 17.38 | 17.55 |
| <hr/> | | | | | | | | |
| Fe II | 15.40 | 16.04 | 18.34 | 18.50 | 13.14 | 17.99 | 18.33 | 18.81 |
| III | 13.86 | 14.86 | 16.36 | 16.73 | 15.62 | 16.04 | 16.54 | 17.76 |
| IV | 13.43 | 14.57 | 17.80 | 18.05 | 18.53 | 17.98 | 17.91 | 17.28 |
| V | 13.20 | 14.49 | 17.11 | 17.20 | 17.43 | 16.95 | 16.75 | 16.94 |
| VI | 13.00 | 14.40 | 16.60 | 16.56 | 16.70 | 16.43 | 16.49 | 17.04 |
| VII | 12.81 | 14.26 | 16.28 | 16.06 | 16.52 | 16.22 | 16.50 | 16.37 |
| VIII | 12.68 | 14.15 | 17.08 | 17.27 | 17.29 | 17.00 | 16.64 | 16.94 |
| IX | 12.49 | 13.97 | 16.43 | 16.46 | 16.49 | 16.32 | 16.48 | 16.63 |
| X | 12.40 | 13.89 | 16.91 | 17.01 | 17.19 | 16.78 | 16.89 | 16.88 |
| XI | 12.40 | 13.90 | 16.92 | 17.03 | 17.11 | 16.85 | 17.20 | 16.93 |
| XII | 12.30 | 13.81 | 16.93 | 17.08 | 17.23 | 17.16 | 17.55 | 16.84 |
| XIII | 12.26 | 13.78 | 17.15 | 17.32 | 17.41 | 17.50 | 17.78 | 16.85 |
| XIV | 12.26 | 13.80 | 17.34 | 17.55 | 17.60 | 17.85 | 17.99 | 16.77 |
| XV | 12.08 | 13.57 | 17.30 | 17.17 | 17.25 | 17.44 | 17.53 | 16.64 |
| XVI | 11.89 | 13.38 | 17.15 | 17.00 | 17.06 | 17.16 | 17.13 | 16.47 |
| XVII | 12.20 | 13.72 | 17.56 | 17.56 | 17.59 | 17.80 | 17.71 | 16.70 |
| XVIII | 12.20 | 13.75 | 17.59 | 17.66 | 17.67 | 17.90 | 17.72 | 16.64 |
| XIX | 12.23 | 13.75 | 17.62 | 17.68 | 16.68 | 17.92 | 17.68 | 16.65 |
| XX | 12.15 | 13.65 | 17.57 | 17.56 | 17.58 | 17.81 | 17.53 | 16.61 |
| XXI | 11.89 | 13.38 | 17.35 | 17.33 | 17.34 | 17.57 | 17.26 | 16.39 |
| XXII | 11.76 | 13.26 | 17.26 | 17.25 | 17.26 | 17.49 | 17.14 | 16.46 |
| XXIII | 11.57 | 13.08 | 17.08 | 17.11 | 17.11 | 17.36 | 16.95 | 16.39 |
| XXIV | 11.61 | 13.15 | 17.11 | 17.21 | 17.22 | 17.42 | 17.01 | 16.60 |
| XXV | 12.04 | 13.57 | 17.53 | 17.63 | 17.65 | 17.88 | 17.41 | 17.18 |
| XXVI | 12.04 | 13.56 | 17.53 | 17.57 | 17.60 | 17.02 | 17.31 | 17.49 |
| XXVII | 11.99 | 13.5 | 17.49 | 17.46 | 17.36 | 15.48 | 17.10 | 17.64 |

TABLE 4
SCALING FACTORS K_i (10^{18} cm^2) FOR ION COLUMN DENSITIES OF OPTICALLY THIN MODELS

| Source * Spectrum Ion | 1 | 2 | 3 | 4 | 5 | 6 | 7 |
|-----------------------------|-------|-------|-------|-------|-------|-------|-------|
| C IV | 1.082 | 4.707 | 2.553 | 7.464 | 14.33 | 0.001 | 0.003 |
| V | 2.308 | 5.000 | 5.085 | 8.805 | 11.30 | 0.002 | 0.018 |
| VI | 0.954 | 2.028 | 2.123 | 2.617 | 3.026 | 0.016 | 0.053 |
| VII | 1.446 | 1.845 | 2.750 | 2.001 | 2.083 | 0.349 | 0.155 |
| N IV | 1.668 | 9.264 | 3.752 | 10.12 | 20.89 | 0.001 | 0.005 |
| V | 2.013 | 2.956 | 4.541 | 7.764 | 9.564 | --- | 0.003 |
| VI | 0.987 | 2.616 | 2.308 | 4.450 | 5.793 | 0.004 | 0.018 |
| VII | 0.654 | 1.236 | 1.435 | 1.496 | 1.624 | 0.028 | 0.051 |
| VIII | 1.192 | 1.412 | 2.140 | 1.382 | 1.431 | 0.335 | 0.148 |
| O IV | 0.883 | 7.408 | 2.025 | 6.343 | 15.68 | --- | 0.004 |
| V | 2.557 | 4.449 | 5.545 | 8.565 | 10.78 | 0.006 | 0.022 |
| VI | 0.631 | 1.714 | 1.572 | 3.215 | 4.729 | --- | 0.002 |
| VII | 0.649 | 1.642 | 1.540 | 2.622 | 3.258 | 0.005 | 0.021 |
| VIII | 0.507 | 0.882 | 1.088 | 0.997 | 1.060 | 0.037 | 0.049 |
| IX | 0.982 | 1.118 | 1.649 | 0.992 | 1.032 | 0.324 | 0.140 |
| Ne IV | 2.106 | 9.513 | 4.707 | 9.826 | 19.45 | 0.001 | 0.004 |
| V | 1.247 | 5.148 | 2.798 | 5.891 | 11.00 | --- | 0.005 |
| VI | 0.902 | 3.129 | 2.046 | 4.009 | 6.461 | --- | 0.005 |
| VII | 0.708 | 2.028 | 1.656 | 2.887 | 3.875 | --- | 0.005 |
| VIII | 0.405 | 0.980 | 1.040 | 1.651 | 2.026 | --- | 0.004 |
| IX | 0.514 | 0.970 | 1.259 | 1.500 | 1.619 | 0.006 | 0.024 |
| X | 0.421 | 0.559 | 0.841 | 0.564 | 0.577 | 0.048 | 0.049 |
| XI | 0.740 | 0.785 | 1.067 | 0.602 | 0.632 | 0.314 | 0.133 |
| Si IV | 4.700 | 4.449 | 10.18 | 12.59 | 12.92 | 0.020 | 0.045 |
| V | 2.580 | 10.44 | 5.632 | 9.451 | 17.45 | 0.006 | 0.015 |
| VI | 1.070 | 4.279 | 2.401 | 4.362 | 7.706 | 0.001 | 0.002 |
| VII | 0.644 | 2.325 | 1.448 | 2.543 | 3.968 | --- | 0.001 |
| VIII | 0.497 | 1.552 | 1.137 | 1.881 | 2.557 | --- | 0.002 |
| IX | 0.399 | 1.048 | 0.920 | 1.336 | 1.612 | --- | 0.004 |
| X | 0.377 | 0.829 | 0.853 | 1.058 | 1.170 | 0.001 | 0.007 |
| XI | 0.360 | 0.651 | 0.886 | 0.887 | 0.935 | --- | 0.010 |
| XII | 0.179 | 0.260 | 0.481 | 0.342 | 0.351 | 0.001 | 0.010 |
| XIII | 0.308 | 0.383 | 0.751 | 0.456 | 0.463 | 0.012 | 0.032 |
| XIV | 0.255 | 0.281 | 0.416 | 0.238 | 0.241 | 0.066 | 0.044 |
| XV | 0.441 | 0.447 | 0.408 | 0.272 | 0.298 | 0.287 | 0.116 |

TABLE 4—Continued

| Source Spectrum * Ion | 1 | 2 | 3 | 4 | 5 | 6 | 7 |
|-----------------------------|-------|-------|-------|-------|-------|-------|-------|
| S IV | 1.850 | 7.316 | 4.151 | 9.570 | 17.38 | 0.004 | 0.007 |
| V | 1.340 | 5.900 | 2.954 | 5.782 | 10.58 | 0.001 | 0.003 |
| VI | 0.563 | 1.983 | 1.267 | 2.500 | 4.352 | 0.001 | 0.001 |
| VII | 0.587 | 2.588 | 1.314 | 2.510 | 4.355 | --- | 0.001 |
| VIII | 0.627 | 2.179 | 1.430 | 2.490 | 3.697 | --- | 0.001 |
| IX | 0.423 | 1.226 | 0.980 | 1.472 | 1.865 | 0.001 | 0.002 |
| X | 0.338 | 0.830 | 0.777 | 1.015 | 1.157 | 0.001 | 0.004 |
| XI | 0.289 | 0.596 | 0.640 | 0.719 | 0.769 | 0.001 | 0.007 |
| XII | 0.279 | 0.477 | 0.618 | 0.574 | 0.597 | 0.001 | 0.010 |
| XIII | 0.223 | 0.313 | 0.540 | 0.368 | 0.378 | 0.001 | 0.012 |
| XIV | 0.127 | 0.153 | 0.338 | 0.168 | 0.170 | 0.001 | 0.013 |
| XV | 0.235 | 0.261 | 0.607 | 0.299 | 0.302 | 0.018 | 0.034 |
| XVI | 0.218 | 0.234 | 0.307 | 0.180 | 0.185 | 0.076 | 0.037 |
| XVII | 0.333 | 0.331 | 0.215 | 0.183 | 0.206 | 0.265 | 0.106 |
| Fe IV | 2.933 | 15.61 | 6.539 | 15.32 | 30.46 | --- | 0.003 |
| V | 1.681 | 6.605 | 3.789 | 8.786 | 16.08 | --- | 0.017 |
| VI | 1.092 | 3.815 | 2.499 | 5.802 | 10.00 | 0.003 | 0.005 |
| VII | 0.692 | 2.093 | 1.609 | 3.418 | 5.203 | 0.002 | 0.002 |
| VIII | 0.513 | 1.238 | 1.176 | 2.148 | 2.808 | 0.001 | 0.002 |
| IX | 0.329 | 0.622 | 0.764 | 1.152 | 1.327 | --- | 0.001 |
| X | 0.272 | 0.742 | 0.635 | 0.992 | 1.226 | --- | --- |
| XI | 0.272 | 0.705 | 0.610 | 0.861 | 1.034 | --- | --- |
| XII | 0.217 | 0.537 | 0.505 | 0.684 | 0.781 | --- | 0.001 |
| XIII | 0.196 | 0.476 | 0.461 | 0.598 | 0.662 | --- | 0.001 |
| XIV | 0.196 | 0.422 | 0.479 | 0.603 | 0.642 | --- | 0.002 |
| XV | 0.128 | 0.259 | 0.329 | 0.317 | 0.333 | --- | 0.002 |
| XVI | 0.084 | 0.151 | 0.196 | 0.144 | 0.149 | --- | 0.003 |
| XVII | 0.175 | 0.281 | 0.391 | 0.292 | 0.300 | 0.003 | 0.010 |
| XVIII | 0.176 | 0.236 | 0.346 | 0.230 | 0.234 | 0.008 | 0.013 |
| XIX | 0.180 | 0.215 | 0.326 | 0.195 | 0.197 | 0.012 | 0.016 |
| XX | 0.151 | 0.169 | 0.271 | 0.134 | 0.135 | 0.013 | 0.017 |
| XXI | 0.084 | 0.089 | 0.156 | 0.066 | 0.067 | 0.008 | 0.014 |
| XXII | 0.062 | 0.065 | 0.124 | 0.047 | 0.047 | 0.009 | 0.015 |
| XXIII | 0.040 | 0.041 | 0.089 | 0.029 | 0.030 | 0.008 | 0.014 |
| XXIV | 0.044 | 0.046 | 0.086 | 0.031 | 0.032 | 0.012 | 0.012 |
| XXV | 0.116 | 0.123 | 0.225 | 0.078 | 0.086 | 0.047 | 0.013 |
| XXVI | 0.115 | 0.121 | 0.038 | 0.067 | 0.071 | 0.096 | 0.011 |
| XXVII | 0.105 | 0.089 | 0.002 | 0.048 | 0.061 | 0.150 | 0.082 |

Values less than 5×10^{-4} are not shown

*Source spectrum key

Type

- 1 10 keV bremsstrahlung (same as model 1)
- 2 10 keV bremsstrahlung plus 30,000 K blackbody with luminosity 2.7 times greater (same as model 5).
- 3 2 keV bremsstrahlung (same as model 6)
- 4 ϵ^{-1} power law (same as model 7)
- 5 ϵ^{-1} power law + 30,000 K blackbody with luminosity 2.7 times greater
- 6 4 keV blackbody (same as model 8) outflow solution
- 7 4 keV blackbody inflow solution.

the O III and N III Bowen lines. Line trapping effects are sensitive to our assumption that the cloud is stationary, since velocity gradients in the cloud will facilitate photon escape.

Varying the X-ray source spectrum shows that the model results are most sensitive to the spectrum at low energies. An excess of soft photons causes the ionization and temperature in the cloud to vary slowly with position, smoothing out ionization fronts and reducing photoelectric absorption by the gas. A deficiency of soft photons leads to a thermal instability. In the unstable region more than one gas state can exist, and which obtains depends on the past history of the gas. Line trapping partially suppresses this instability.

Our models are applicable to a variety of different astrophysical objects. These include X-ray sources in low density clouds, such as the interstellar medium, where the time scale for pressure equilibration of the cloud with its surroundings is long, and X-ray sources in clouds where the gas density is prescribed by some external mechanism, such as in a stellar wind. When the gas flow has large velocity gradients, our treatment of

resonance line escape must be modified, e.g., by including a Sobolev escape probability for resonance lines.

Further work is needed to extend the range of applicability of our models to situations where the gas density is not specified *a priori*. An example is in the broad-line emitting region of quasars, which are thought to consist of clouds in pressure equilibrium with their surroundings. Models for constant pressure clouds will contain the same essential physics as the models presented here, except that the effect of the thermal instability described in § VIh will be greatly enhanced. We plan to present detailed models for these objects in a future paper.

We thank Steven Manson, Craig Sarazin, and John Raymond for providing their atomic rate data prior to publication, and Jules Halpern and Josh Grindlay for pointing out errors in an earlier version of this paper. Computing resources were provided by a grant from the National Center for Atmospheric Research. This work was supported by NASA grant NSG-7128 and by NSF grant AST 80-19960.

REFERENCES

- Abbott, D. 1978, *J. Phys. B*, **11**, 3479.
 Aldrovandi, S., and Pequignot, D. 1973, *Astr. Ap.*, **25**, 137; 1976, **47**, 321.
 Bambynek, W., et al. 1972, *Rev. Mod. Phys.*, **44**, 716.
 Barfield, W. C., Koontz, G. D., and Huebner, W. F. 1972, *J. Quant. Spectrosc. Rad. Transf.*, **12**, 1409.
 Basko, M. M., et al. 1977, *Ap. J.*, **215**, 276.
 Bekefi, G. 1966, *Radiation Processes in Plasma* (New York: Wiley).
 Bethe, H. A., and Salpeter, E. E. 1957, *Quantum Mechanics of One and Two Electron Atoms* (Berlin: Springer-Verlag).
 Bhalla, C. P., and Hein, M. 1973, *Phys. Rev. Letters*, **30**, 39.
 Biemont, E. 1976, *J. Quant. Spectrosc. Rad. Transf.*, **16**, 137.
 Blumenthal, G. R., Drake, G. W. F., and Tucker, W. H. 1972, *Ap. J.*, **172**, 205.
 Brocklehurst, M. 1971, *M.N.R.A.S.*, **153**, 471.
 Buff, J., and McCray, R. 1974a, *Ap. J.*, **189**, 147.
 ———. 1974b, *Ap. J. (Letters)*, **188**, L37.
 Burgess, A., Summers, H. P., Cochran, D. M., and McWhirter, R. W. P. 1977, *M.N.R.A.S.*, **179**, 275.
 Burke, P. G., Ormonde, S., and Whitaker, W. 1967, *Proc. Phys. Soc. London*, **92**, 319.
 Butler, S., and Dalgarno, A. 1980, *Ap. J.*, **241**, 838.
 Butler, S., Heil, T. G., and Dalgarno, A. 1980, *Ap. J.*, **241**, 442.
 Cassinelli, J. P., and Olson, G. L. 1979, *Ap. J.*, **229**, 304.
 Castor, J. I. 1970, *M.N.R.A.S.*, **149**, 111.
 Clementi, E. 1965, *IBM J. Res. Dev.*, **9**, 2.
 Cowie, L. L., Ostriker, J. P., and Stark, A. A. 1978, *Ap. J.*, **226**, 1041.
 Cox, D. P. 1970, Ph.D. thesis, University of California, San Diego.
 Crandall, D. H., Phaneuf, R. A., and Gregory, D. C. 1979, ORNL Rept.
 Crandall, D. H., Phaneuf, R. A., Hasselquist, B. E., and Gregory, D. C. 1979, *J. Phys. B*, **12**, L247.
 Czyzak, S. J., and Krueger, T. K. 1966, *Ap. J.*, **144**, 381.
 Dalgarno, A., and Butler, S. 1978, *Comments At. Molec. Phys.*, **7**, 129.
 Dalgarno, A., Heil, T. G., and Butler, S. 1981, *Ap. J.*, **245**, 793.
 Davidson, K., and Netzer, H. 1979, *Rev. Mod. Phys.*, **51**, 715.
 Dupree, A. K., et al. 1980, *Ap. J.*, **238**, 969.
 Ferland, G., and Netzer, H. 1979, *Ap. J.*, **229**, 274.
 Field, G. B., and Steigman, G. 1971, *Ap. J.*, **166**, 59.
 Gabriel, A. H., and Jordan, C. 1969, *M.N.R.A.S.*, **145**, 241.
 Garstang, R. H., Robb, W. D., and Rountree, S. P. 1978, *Ap. J.*, **222**, 384.
 Gau, J. N., and Henry, R. J. W. 1977, *Phys. Rev. A*, **16**, 986.
 Gould, R. J., and Thakur, R. K. 1970, *Ann. Phys.*, **61**, 351.
 Halpern, J. P., and Grindlay, J. E. 1980, *Ap. J.*, **242**, 1041.
 Hammerschlag-Hensberge, G. 1981, in *IAU Colloquium 59, Effects of Mass Loss on Stellar Evolution*, ed. C. Choisi and R. Stalio (Dordrecht: Reidel), p. 457.
 Hatchett, S., Buff, J., and McCray, R. 1976, *Ap. J.*, **206**, 847 (HBM).
 Hatchett, S., and McCray, R. 1977, *Ap. J.*, **211**, 552.
 Hollenbach, D., and McKee, C. F. 1978, *Ap. J. Suppl.*, **41**, 555.
 House, L. L. 1969, *Ap. J. Suppl.*, **18**, 21.
 Huebner, W. F., Argo, M. F., and Ohlsen, L. D. 1978, *J. Quant. Spectrosc. Rad. Transf.*, **19**, 93.
 Hummer, D. G. 1968, *M.N.R.A.S.*, **138**, 73.
 Hummer, D. G., and Rybicki, G. 1971, *Ann. Rev. Astr. Ap.*, **9**, 237.
 Illarionov, A. A., Kallman, T., McCray, R., and Ross, R. R. 1979, *Ap. J.*, **228**, 279.
 Kallman, T., and McCray, R. 1980, *Ap. J.*, **242**, 615.
 Kato, T. 1976, *Ap. J. Suppl.*, **30**, 397.
 Krolik, J. H., and McKee, C. F. 1978, *Ap. J. Suppl.*, **37**, 459.
 Krolik, J. H., McKee, C. F., and Tarter, C. B. 1981, *Ap. J.*, **249**, 422.
 Kwan, J., and Krolik, J. H. 1979, *Ap. J. (Letters)*, **233**, L91.
 Lewin, W. G., and Joss, P. C. 1981, *Space Sci. Rev.*, **28**, 3.
 London, R. 1979, *Ap. J.*, **228**, 8.
 London, R., McCray, R., and Auer, L. H. 1981, *Ap. J.*, **243**, 970.
 Lotz, W. 1967, *Ap. J. Suppl.*, **14**, 207.
 Mahan, A. H., Gallagher, A., and Smith, S. J. 1976, *Phys. Rev. A*, **13**, 156.
 Manson, S. T. 1979, private communication.
 McClintock, F. E., Canizares, C. R., and Tarter, C. B. 1975, *Ap. J.*, **198**, 641.
 McCray, R. 1979, in *Active Galactic Nuclei*, ed. C. Hazard and S. Mitton (Cambridge: Cambridge University Press), p. 227.
 McCray, R., Wright, C., and Hatchett, S. 1977, *Ap. J. (Letters)*, **186**, L63.
 McGuire, E. J. 1969, *Phys. Rev.*, **185**, 1.
 ———. 1970, *Phys. Rev. A*, **2**, 273.
 Mewe, R. 1972, *Astr. Ap.*, **20**, 215.
 ———. 1977, *Astr. Ap.*, **59**, 275.
 Mewe, R., and Schrijver, J. 1978, *Astr. Ap.*, **65**, 99.
 Missavage, D. W., Manson, S. T., and Daum, G. R. 1977, *Phys. Rev. A*, **15**, 1001.

- Morton, D. C., and Smith, W. H. 1973, *Ap. J. Suppl.*, **26**, 333.
- Osterbrock, D. E. 1974, *Astrophysics of Gaseous Nebulae* (San Francisco: Freeman).
- Ostriker, J. P., McCray, R., Weaver, R., and Yahil, A. 1976, *Ap. J. (Letters)*, **208**, L61.
- Pradhan, A. K., Norcross, D. W., and Hummer, D. G. 1981, *Ap. J.*, **246**, 1031.
- Raymond, J. 1976, Ph.D. thesis, University of Wisconsin.
- _____. 1978, private communication.
- Reilman, F. K., and Manson, S. T. 1978, *Phys. Rev. A*, **18**, 2724.
- Ross, R. R. 1979, *Ap. J.*, **233**, 334.
- Ross, R. R., Weaver, R., and McCray, R. 1978, *Ap. J.*, **219**, 292.
- Sarazin, C. 1978, private communication.
- Shapiro, P. R., and Bahcall, J. N. 1981, *Ap. J.*, **245**, 163.
- Shull, J. M. 1979, *Ap. J.*, **234**, 761.
- _____. 1981, *Ap. J. Suppl.*, **46**, 27.
- Stern, R., Wang, E., and Bowyer, S. 1978, *Ap. J. Suppl.*, **37**, 195.
- Summers, H. P. 1972, *M.N.R.A.S.*, **158**, 255.
- Sunyaev, R. A., and Trümper, J. 1979, *Nature*, **279**, 506.
- Tananbaum, H., *et al.* 1979, *Ap. J. (Letters)*, **234**, L9.
- Tarter, C. B., and McKee, C. F. 1973, *Ap. J. (Letters)*, **186**, L63.
- Tarter, C. B., and Salpeter, E. E. 1969, *Ap. J.*, **156**, 953.
- Tarter, C. B., Tucker, W., and Salpeter, E. E. 1969, *Ap. J.*, **156**, 943. (TTS).
- Treves, A., *et al.*, 1980, *Ap. J.*, **242**, 1114.
- Tucker, W. H., and Koren, M. 1971, *Ap. J.*, **168**, 283 (erratum 170, 621).
- Van Regemorter, H. 1962, *Ap. J.*, **136**, 906.
- Weisheit, J. C. 1974, *Ap. J.*, **190**, 735.
- Wiese, W. L., Smith, M. W., and Glennon, B. M. 1966, *Atomic Transition Probabilities*, Vol. **1**, NSRDS-NBS 4.
- Wiese, W. L., Smith, M. W., and Miles, B. M. 1969, *Atomic Transition Probabilities*, Vol. **2**, NSRDS-NBS 22.
- Withbroe, G. L. 1971, in *The Menzel Symposium on Solar Physics, Atomic Spectra, and Gaseous Nebulae*, ed. K. B. Gebbie (NBS Spec. Pub. 353), p. 127.

TIMOTHY R. KALLMAN: Massachusetts Institute of Technology, Cambridge, MA 02139

RICHARD MCCRAY: Joint Institute for Laboratory Astrophysics, University of Colorado, Boulder, CO 80309